Experimental studies on thermal transport in magnetized high energy density plasma for fast ignition inertial confinement fusion

by

Kazuki MATSUO

Supervised by Shinsuke Fujioka

Graduate School of Science
Department of Physics
Osaka University

March 2019

Abstract

The main scope of this dissertation is showing the effect of thermal transport in the magnetic field on Magnetized Fast Ignition(MFI) scheme, which combines a conventional Fast Ignition(FI) scheme with a strong magnetic field. In MFI scheme, a high-intensity laser is irradiated on the surface of a substance that becomes fuel in an external magnetic field, and the fuel is compressed with ablation pressure. Fluid instability grows as the fuel is compressed toward the center. Finally, energy is injected into the compressed fuel core from the outside using a short pulse laser of several picoseconds and heated instantaneously. We experimentally verified that the effect of thermal transport in a strong magnetic field on high energy density plasma in three stages: laser to ablation pressure conversion, fluid instability growth, and the core heating.

The external magnetic field reduces electron thermal transport across the external magnetic field lines because the Larmor radius of the thermal electrons in the external magnetic field is much shorter than the mean free path of the ther-

mal electrons. The suppression of electron thermal transport in a magnetic field increases the temperature and pressure of the ablation plasma. The velocity of a thin polystyrene foil driven by intense laser beams in the strong external magnetic field is faster than that in the absence of the external magnetic field. Growth of sinusoidal corrugation imposed initially on the laser-driven polystyrene surface is enhanced by the external magnetic field because the plasma pressure distribution becomes nonuniform due to the external magnetic-field structure modulated by the perturbed plasma flow ablated from the corrugated surface. We experimentally revealed that an external magnetic field of 200–300 T notably affects hydrodynamics due to anisotropic thermal transport, even when the magnetic field pressure is much lower than the plasma pressure.

A study of the contribution of thermal transport on the core heating with multi-picoseconds intense laser pulse in a strong magnetic field is also discussed in this thesis. We have achieved experimentally 2.2 petapascal pressure of ultra-high-energy-density (UHED) state with 4.6 kJ of the total laser energy that is one order of magnitude lower than the energy used in the conventional implosion scheme. Particle-in-cell simulations with the experimental conditions confirm that the diffusive heating mechanism in which thermal electrons transport their energy diffusively from the laser heated hot region to the cold dense region plays an essential role to heat the core plasma over keV range.

Achievements

Publications

1. **K.Matsuo**, N.Higashi, N.Iwata, S.Sakata, S.Lee, T.Johzaki, H.Sawada, Y.Iwasa, K.F.F.Law, H.Morita, Y.Ochiai, S.Kojima, Y.Abe, M.Hata, T.Sano, H.Nagatomo, A.Sunahara, A.Morace, A.Yogo, M.Nakai, H.Sakagami, T.Ozaki, K.Yamanoi, T.Norimatsu, Y.Nakata, S.Tokita, J.Kawanaka, H.Shiraga, K.Mima, H.Azechi, R.Kodama, Y.Arikawa, Y.Sentoku and S.Fujioka, "Peta-Pascal Pressure Driven by Fast Isochoric Heating with Multi-Picosecond Intense Laser Pulse", Phys.Rev.Lett 124, 035001 (2020).
2. **K.Matsuo**, H.Nagatomo, Z.Zhang, T.Sano, S.Sakata, S.Kojima, S.Lee, K.F.F.Law, Y.Arikawa, Y.Sakawa, T.Morita, Y.Kuramitsu, S.Fujioka and H.Azechi, "Magnetohydrodynamics of laser-produced high-energy-density-plasma in a strong external magnetic field", Phys.Rev.E 95, 053204 (2017).

3. C.Liu, **K.Matsuo**, S.Ferri, H.Chung, S.Lee, S.Sakata, K.F.F.Law, H.Morita, B.Pollock, J.Moody, S.Fujioka, "Design of Zeeman spectroscopy experiment with magnetized silicon plasma generated in the laboratory", High Energy Density Physics, 33, 100710 (2019).
4. S.Kojima, M.Hata, N.Iwata, Y.Arikawa, A.Morace, S.Sakata, S.Lee, **K.Matsuo**, K.F.F.Law, H.Morita, Y.Ochiai, A.Yogo, H.Nagatomo, T.Ozaki, T.Johzaki, A.Sunahara, H.Sakagami, Z.Zhang, S.Tosaki, Y.Abe, J.Kawanaka, S.Tokita, M.Nakai, H.Nishimura, H.Shiraga, H.Azechi, Y.Sentoku, S.Fujioka, "Electromagnetic field growth triggering super-ponderomotive electron acceleration during multi-picosecond laser-plasma interaction", Commun. Phys. 2, 99 (2019).
5. S.Sakata, S.Lee, T.Morita, T.Johzaki, H.Sawada Y.Iwasa, **K.Matsuo**, K.F.F.Law, A.Yao, M.Hata, A.Sunahara, S.Kojima, Y.Abe, H.Kishimoto, A.Syuhada, T.Shiroto, A.Morace, A.Yogo, N.Iwata, M.Nakai, H. Sakagami, T.Ozaki, K.Yamanoi, T.Norimatsu, Y.Nakata, S.Tokita, N.Miyanaga, J.Kawanaka, H.Shiraga, K.Mima, H.Nishimura, M.Bailly-Grandvaux, J.J.Santos, H.Nagatomo, H.Azechi, R.Kodama, Y. Arikawa, Y.Sentoku, S.Fujioka, "Magnetized fast isochoric laser heating for efficient creation of ultra high energy density states", Nat. Commun. 9, 3937 (2018).
6. H Nagatomo, T Johzaki, T Asahina, M Hata, **K.Matsuo**, S.Lee, A.Sunahara, H.Sakagami, K.Mima, K.Iwano, S.Fujioka, H.Shiraga, H.Azechi, "Compression and electron beam heating of solid target under the external magnetic field for fast ignition", Nuclear Fusion 57 (8), 086009 (2017).

7. K.F.F.Law, M.Bailly-Grandvaux, A.Morace, S.Sakata, **K.Matsuo**, S.Kojima, S.Lee, X. Vaisseau, Y.Arikawa, A.Yogo, K.Kondo, Z.Zhang, C.Bellei, J.J.Santos, S.Fujioka and H.Azechi, "Direct measurement of kilo-tesla level magnetic field generated with laser-driven capacitor-coil target by proton deflectometry", Applied Physics Letters, 108, 091104 (2016).
8. T.Ozaki, M.Hata, **K.Matsuo**, S.Kojima, Y.Arikawa, S.Fujioka, H.Sakagami, A.Sunahara, H.Nagatomo, T.Johzaki, A.Yogo, A.Morace, Z.Zhang, H.Shiraga, S. Sakata, T.Nagai, Y.Abe, S.Lee, M.Nakai, H.Nishimura, H.Azechi, FIREX group and GXII-LFEX group, "Electron transport estimated from electron spectra using electron spectrometer in LFEX laser target experiments", J. Phys.: Conf. Ser. 717 012043 (2016).
9. H.Nagatomo, T.Johzaki, T.Asahina, **K.Matsuo**, A.Sunahara, H.Sakagami, T.Sano, K.Mima, A.Morace, Z.Zhang, S.Fujioka, K.Shigemori, H.Shiraga and FIREX project group, "An optimum design of implosion with external magnetic field for electron beam guiding in fast ignition", J. Phys.: Conf. Ser. 717 012043 (2016).

Presentation in Conferences

1. **K.Matsuo**, T.Sano, H.Nagatomo, K.Ishigure, H.Kato, H.Nagatomo, N.Philippe, N.Nagamatsu, Y.Sakawa, Y.Arikawa, S.Sakata, S.Lee, K.K.F.Law, H.Morita, C.Liu, H.Li, J.Nishibata, R.Takizawa, H.Azechi and S.Fujioka, "Experimental study for characterizing the effect of a strong magnetic field to interfacial instability", 11th International Conference on Inertial Fusion Sciences and Applications, Osaka, Japan, Sep. 22 - Sep. 27, (2019).
2. **K.Matsuo**, H.Nagatomo, T.Sano, N.Philippe, T.Somekawa, Y.Sakawa, Y. Arikawa, S.Sakata, S.Lee, K.K.F.Law, H.Morita, H.Azechi and S.Fujioka, "Growth of ablative Rayleigh-Taylor instability in a strong external magnetic field", 2nd Asia-Pacific Conference on Plasma Physics, Nov. 12, (2018).
3. **K.Matsuo**, H.Sawada, H.Nagatomo, T.Shiroto, S.Lee, S.Sakata, S.Kojima, K.K.F.Law, H.Morita, Y.Iwasa, Y.Arikawa, H.Azechi and S.Fujioka, "Measurements of Temporal evolution of implosion core in strong magnetic field", 10th International Conference on Inertial Fusion Sciences and Applications, Saint Malo, France, Sep. 11 - Sep. 15, (2017).
4. **K.Matsuo**, H.Sawada, H.Nagatomo, T.Shiroto, S.Lee, S.Sakata, S.Kojima, K.K.F.Law, H.Morita, Y.Iwasa, Y.Arikawa, H.Azechi and S.Fujioka, "Measurements of Temporal evolution of implosion core in strong magnetic field", Direct Drive Fast Ignition Workshop 2017, Salamanca, Spain, Mar. 22 - Mar. 24, (2017).

5. **K.Matsuo**, H.Nagatomo, T.Sano, Z.Zhang, P.Nicolai, J.Breil, Y.Sakawa, Y.Hara, H.Shimogawara, Y. Arikawa, S.Sakata, K.K.F.Law, S-H.Lee, S.Kojima, H.Kato, K.Shigemori, S.Fujioka, H.Azechi, "Hydrodynamic instability of high-energy-density-plasma in strong magnetic field" Conference on Laser Energy Science, Yokohama, Japan, May. 17 - May. 20, (2016).
6. **K.Matsuo**, H.Nagatomo, T.Sano, Z.Zhang, Y.Sakawa, Y.Hara, H.Shimogawara, Y. Arikawa, S.Sakata, K.K.F.Law, S.Lee, S.Kojima, H.Kato, K.Shigemori, H.Azechi and S.Fujioka, "Magnetohydrodynamics of high-energy-density-plasma in strong magnetic field", 58th Annual Meeting of the APS Division of Plasma Physics, San Jose, California, Oct. 31 - Nov. 4, (2016).
7. **K.Matsuo**, Y.Arikawa, Y.Iwasa, S.Sakata, K.K.F.Law, S.Lee, H.Morita, L.Chang, L.Huan, H.Azechi and S.Fujioka, "Creation of high energy density state by direct interaction between multi-pico second intense laser pulse and dense matte", 35th annual meeting of the Japanese Society of Plasma science and nuclear Fusion research, Dec. 3 – Cec.6, (2018).

Academic Awards

1. Institute of Laser Engineering Progress Award (December 2019)
2. Chiyoe Yamanaka Award, IFSA (September 2019)
3. Student Presentation Award of the Japan Physical Society (September 2019)
4. Excellent Young Presentation Prize in the 35th annual meeting of the Japanese Society of Plasma science and nuclear Fusion research (December 2018)
5. AAPPS-DPP Poster Prize, Association of Asia-Pacific Physical Societies (November 2018)
6. Student Presentation Award of the Japan Physical Society (March 2016)

Contents

List of Tables

List of Figures

1. Inertial confinement fusion

The sun keeps shining using the tremendous energy produced by the nuclear fusion reactions. When two nuclei combine, a huge amount of energy is released. And this energy is called fusion energy. This energy comes from the mass difference between the fusion products and the original interacting nuclei. The energy released is calculated from one of the most famous formula $E = mc^2$. It is beneficial to implement a sustainable this enormous fusion energy source in our society.

Using a deuterium-tritium(DT) reaction is easiest way to achieve a thermonuclear ignition thanks to its large cross section.

$$\mathrm{D} + \mathrm{T} \longrightarrow {}^4\mathrm{He}(3.5\mathrm{MeV}) + \mathrm{n}(14.1\mathrm{MeV}) \tag{1.1}$$

As a result of the DT reaction, nucleus of helium-4(^{4}He) and neutron(n) are generated, as shown in Fig.1.1. For interacting nuclei, it is necessary to overcome the Coulomb barrier of each other. The thermonuclear ignition require high temperature of the order of several tens of million degrees or keV. The neutron does not interact with the surrounding thermonuclear fuel, because they have no charge.

The alpha particle can give its energy to the surrounding thermonuclear fuel. It is helpful to maintain high temperature which is required for the reaction.

It is necessary to generate high-temperature and high-density plasma on the earth and maintain or repeat frequently the fusion reaction for a long time. At present, mainly two methods are being studied: confining fuel plasma in a high magnetic field using a superconducting coil and implosing fuel plasma using a high-power laser. Inertial confinement fusion (ICF) is one of a concept to achieve such a condition using a high-power laser. There are two strategies to ignite the thermonuclear fuel in ICF. One is central ignition and the other is fast ignition, as shown in Fig.1.2.

It has become clear that it is not easy to obtain high-temperature and high-density plasma efficiently with the conventional central ignition scheme. Currently, the research for the demonstration of fast ignition coupled with a strong magnetic field is continuing to achieve such a plasma efficiently in the institute of laser engineering osaka university (ILE) by using a high power laser system named GEKKO-XII and LFEX laser.

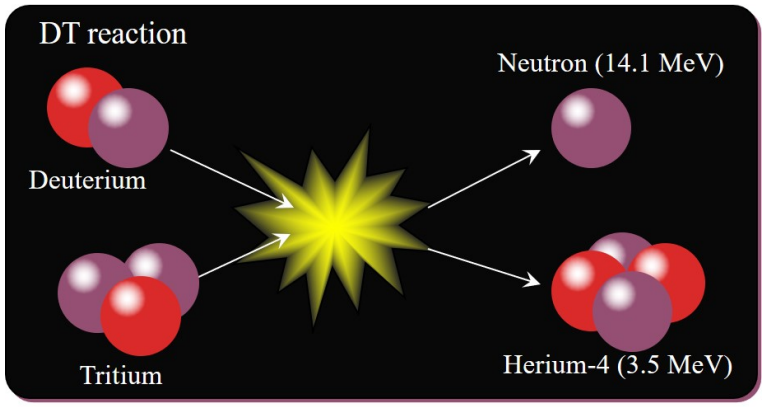

Figure 1.1: Deuterium-Tritium(DT) reaction

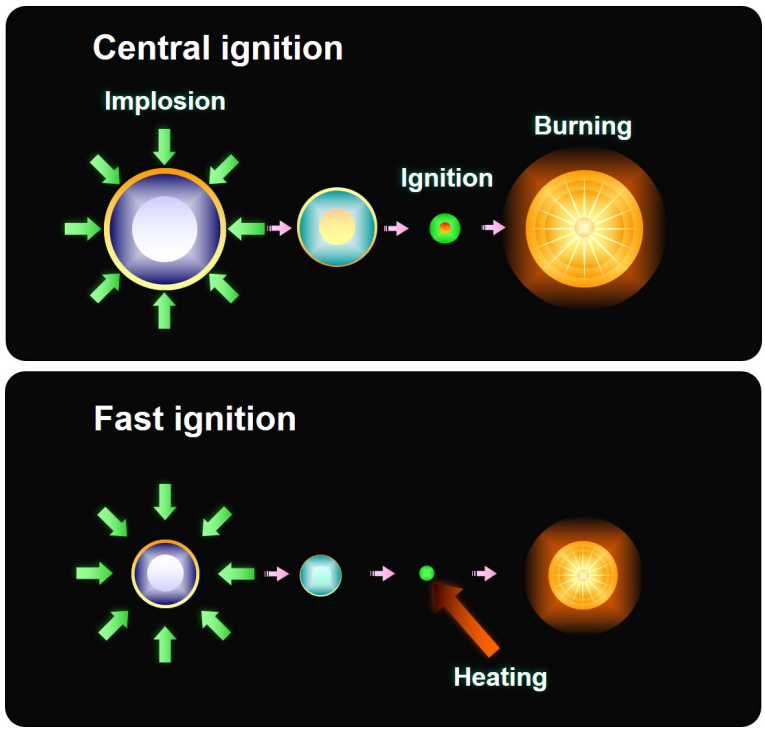

Figure 1.2: Central ignition and Fast ignition

1.1 Central ignition

Central ignition is a type of fusion energy research that attempts to initiate nuclear fusion reactions by heating and compressing a fuel target, typically in the form of a shell that most often contains a mixture of deuterium and tritium, as shown in Fig.1.2. To compress and heat the fuel, energy is delivered to the outer layer of the target using high-energy beams of laser light. The heated outer layer explodes outward, producing a reaction force against the remainder of the target, accelerating it inwards, compressing the target. This process is designed to create shock waves that travel inward through the target. A sufficiently powerful set of shock waves can compress and heat the fuel at the center so much that fusion reactions occur.

In conventional implosion, kinetic energy of the imploded shell is converted to the internal energy of the compressed matter at the maximum compression. A ultra-high-energy-density(UHED) state with 36 Peta-Pascal (PPa) was achieved on the National Ignition Facility with 1.8 MJ of laser energy by the indirect X-ray driven implosion[1]. The OMEGA laser facility with 30 kJ of laser energy produced 5.6 PPa of UHED by the direct laser-driven implosion[2]. The current central ignition scheme requires enormous laser energy to create UHED state. The significant growth of hydrodynamic instabilities during the compression causes the hot spark mixing with the cold dense fuel and prevents efficient creation of UHED state.

[1] Le Pape et al. 2018.
[2] Regan et al. 2016.

1.2 Fast ignition

In the context of ICF, the fast isochoric heating also known as the Fast ignition(FI) had been proposed as an alternative approach[3]. This approach separates compression and heating processes to avoid the mixing, using a more stable compression followed by an external energy injection whose time scale is much shorter than the implosion time scale, as shown in Fig.1.2. The implosion does not need to create a compressed hot spot. Hence, it potentially leads to higher gain by increasing the mass of the compressed fuel.

A cone-in-shell target is commonly used in the integrated fast-isochoric-heating experiments, since a dense plasma core, which is produced by the laser-driven implosion, is surrounded by a long-scale-length coronal plasma, as shown in Fig.1.3. The cone preserves a vacuum channel in the coronal plasma for the heating laser pulse to access the compressed core. Significant progresses have been made on the fast isochoric heating to increase the laser-to-core energy coupling[4]. Those improvements mainly focus on increasing laser-to-core energy coupling by drag heating which is the energy exchange through binary collisions between relativistic electrons (REs) and bulk electrons of the plasma.

There are three major mechanisms of the fast isochoric heating[5]. The first mechanism is the heating by REs, which is often called drag heating. The REs' large divergence is a critical issue in the drag heating. Enhancement of the laser-

[3] Tabak et al. 1994.
[4] R.Kodama 2001; Theobald et al. 2014; Jarrott et al. 2016.
[5] Kemp et al. 2006.

to-matter energy coupling with the magnetized fast isochoric heating scheme was reported by Ref.[6]. The maximum coupling efficiency via the drag heating reached $7.7 \pm 1.2\%$ because of reduction of RE's divergence by the application of the external magnetic field. The second mechanism is the resistive heating. The RE current drives return current to maintain current neutrality in a plasma. Since the return current is more collisional than the RE current, the return current heats the plasma ohmically. The resistive heating is the dominant heating mechanism in the laser-plasma interaction region. The third mechanism is the diffusive heating, in which thermal electrons transport their energy diffusively from the laser heated hot region to the cold dense region. The diffusive heating has been identified as one of the dominant mechanisms for laser isochoric heating for the first time in Ref. [7]. A high ionization state in a solid was produced by thermal diffusion in a few picoseconds even after the pulse terminates. By extending the pulse duration, the laser supplies its energy continuously to the hot plasma while the thermal diffusion takes place. The diffusive heating becomes more important to heat the dense core (> 10 g/cm^3) beyond keV by multi-picosecond heating laser pulse duration.

1.3 Ignition condition

For igniting the thermonuclear fuel, the energy from the nuclear fusion(w_{dep}) should exceed energy losses due to emission of radiation(w_{r}), thermal conduction(w_{c}),

[6] Sakata et al. 2018.
[7] Sawada, Sentoku, et al. 2019.

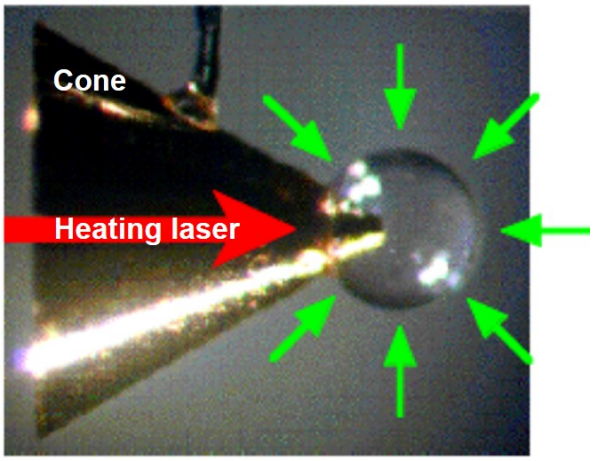

Figure 1.3: A cone-in-shell target

and convection(w_{m}). We can define the ignition condition as:

$$w_{\mathrm{dep}} > w_{\mathrm{r}} + w_{\mathrm{c}} + w_{\mathrm{m}} \tag{1.2}$$

w_{dep} is a term of self-heating by alpha particles and neutrons generated by fusion reactions. Using a deuterium-tritium(DT) reaction, w_{dep} can express as:

$$w_{\mathrm{dep}} = \frac{1}{4} {n_{\mathrm{i}}}^2 < \sigma v >_{\mathrm{DT}} (E_\alpha f_\alpha + E_n f_n) \tag{1.3}$$

where $< \sigma v >_{\mathrm{DT}}$ is average DT reactivity obtained by the collision cross section and the velocity distribution(Boltzman distribution) of the relative velocity between particles[8]. $E_\alpha = 3.5\mathrm{MeV}$ and $E_n = 5E_\alpha$ are deposition energy of alpha particles and neutrons respectively. Neutron stopping range in DT plasma ($\lambda_n \approx 4.7/\rho_{\mathrm{h}}\,\mathrm{cm}$)

[8] Peres 1979.

is larger than radius of the ignition core ($R_\mathrm{h} \approx 0.5/\rho_\mathrm{h}\,\mathrm{cm}$), therefore the energy deposition rate of neutron heating is negligible ($f_n = 0$). The energy deposition rate of alpha heating is:

$$\frac{3}{2}\tau_\alpha - \frac{4}{5}\tau_\alpha^2 \tag{1.4}$$

for ratio of alpha particle stopping range in DT plasma to radius of the ignition core $\tau_\alpha = R_\mathrm{h}/\lambda_\alpha < \frac{1}{2}$ and,

$$1 - \frac{1}{4\tau_\alpha} + \frac{1}{160\tau_\alpha^3} \tag{1.5}$$

for $\tau_\alpha > \frac{1}{2}$[9]. We can rewrite equation (1.3) to:

$$w_\mathrm{dep} = A_\alpha f_\alpha \rho_\mathrm{h}^2 < \sigma v >_\mathrm{DT} \tag{1.6}$$

where A_α is constant value($= 8.06 \times 10^{40}\mathrm{erg\,g^{-2}}$).

The ignition core is optically thin for bremsstrahlung xrays and reabsorption is negligible. The energy loss due to emission of radiation(w_r) can simply write:

$$w_\mathrm{r} = A_b \rho_\mathrm{h}^2 T_\mathrm{h}^{\frac{1}{2}} \tag{1.7}$$

where T_h is temperature of the ignition core, and A_b is constant value($= 3.05 \times 10^{23}\mathrm{erg\,cm^3\,g^{-2}\,s^{-1}\,keV^{-\frac{1}{2}}}$).

To describe the heat transport, Spitzer[10] models is usually employed. In the derivation of the models, they assume a collisional plasma in which the mean free

[9] Krokhin and Rozanov 1973.
[10] Spitzer and Härm 1953.

path of thermal particles is much shorter than the temperature gradient scale length and therefore the distribution function is close to Maxwellian. From the model, the energy loss due to thermal conduction($w_{\rm c}$) is described as:

$$\begin{aligned} w_{\rm c} &= \frac{1}{V_{\rm hs}} \int -\nabla \cdot \kappa_{\rm e} \nabla T_{\rm e} d\vec{r} \\ &\approx 3 \frac{A_e}{\ln\Lambda} \frac{T_{\rm h}^{\frac{7}{2}}}{R_{\rm h}^2} \end{aligned} \tag{1.8}$$

where A_e is constant value($= 9.50 \times 10^{19} \mathrm{erg\,s^{-1}\,cm^{-1}\,keV^{-\frac{7}{2}}}$).

The energy loss due to convection($w_{\rm m}$) is defined as:

$$w_{\rm m} = -\frac{1}{V_{\rm h}} p_{\rm h} \frac{dV_{\rm h}}{dt} \tag{1.9}$$

where $V_{\rm h}$ is volume of the ignition core($=\frac{4}{3}\pi R_{\rm h}^3$) and $p_{\rm h}$ is pressure of the ignition core. Here we assume that $p_{\rm h}$ can be expressed by the equation of state of ideal gas:

$$p_{\rm h} = 2 \frac{\rho_{\rm h}}{m_{\rm i}} k_{\rm B} T_{\rm h} \tag{1.10}$$

and the expansion speed of the ignition core can apply the equation of fluid velocity behind strong shock:

$$\frac{dR_{\rm h}}{dt} = \sqrt{\frac{2p_{\rm h}}{\gamma+1}\rho_{\rm h}} \tag{1.11}$$

where $k_{\rm B}$ is Boltzman constant and $\gamma = 5/3$ for strong shock. Using equation (1.10)

and (1.11), we can rewrite the equation(1.9) to:

$$w_{\mathrm{m}} = A_m \frac{\rho_{\mathrm{h}}}{R_{\mathrm{h}}} T_{\mathrm{h}}^{\frac{3}{2}} \tag{1.12}$$

where A_m is constant value($= 5.51 \times 10^{22} \mathrm{cm}^3\,\mathrm{s}^{-3}\,\mathrm{keV}^{-\frac{3}{2}}$). Figure1.4 is typical profile of the core density, temperature, and pressure. In fast ignition scheme, the core pressure is large because of external heating with a constant density, as shown in Fig.1.4(a). Therefore it is necessary to consider the energy loss due to convection. On the other hand, in central ignition scheme, the core is made by adiabatic compression, so there is no pressure difference between the core and its surroundings, as shown in Fig.1.4(b). Therefore $w_{\mathrm{m}} = 0$ in central ignition scheme.

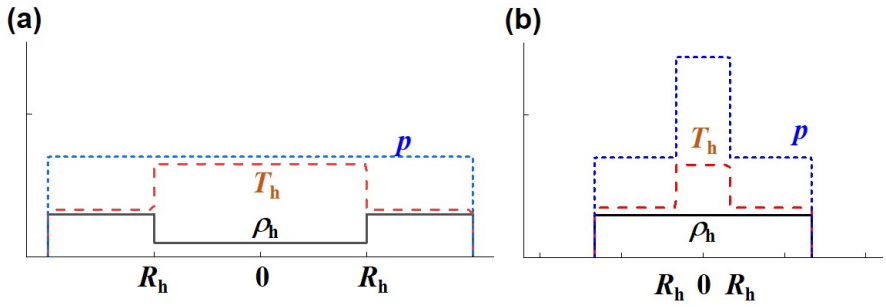

Figure 1.4: Typical profile of the core (a) in central ignition scheme and (b) in fast ignition scheme.

Substituting that equation (1.6), (1.7), (1.8), (1.12) into equation (1.2), we can represent the ignition conditions with ρR_{h} and T_{h}:

$$(A_\alpha f_\alpha < \sigma v >_{\mathrm{DT}} - A_b T_{\mathrm{h}}^{\frac{1}{2}})(\rho R_{\mathrm{h}})^2 - A_m (\rho R_{\mathrm{h}}) T_{\mathrm{h}}^{\frac{3}{2}} - \frac{3A_e}{\ln\Lambda} T_{\mathrm{h}}^{\frac{7}{2}} > 0 \tag{1.13}$$

Figure1.5 show the ignition condition calculated from equation(1.13). The point that satisfies the ignition conditions with minimum internal energy is $\rho R_{\mathrm{h}} = 0.32\mathrm{g/cm}^2, T_{\mathrm{h}} = 6.7\mathrm{keV}$ in central ignition scheme and $\rho R_{\mathrm{h}} = 0.54\mathrm{g/cm}^2, T_{\mathrm{h}} = 8.9\mathrm{keV}$ in fast ignition scheme. We have not yet reached the ignition condition. For igniting the thermonuclear fuel, it is required that increasing w_{dep} and/or reducing w_{r}, w_{c}, and w_{m}.

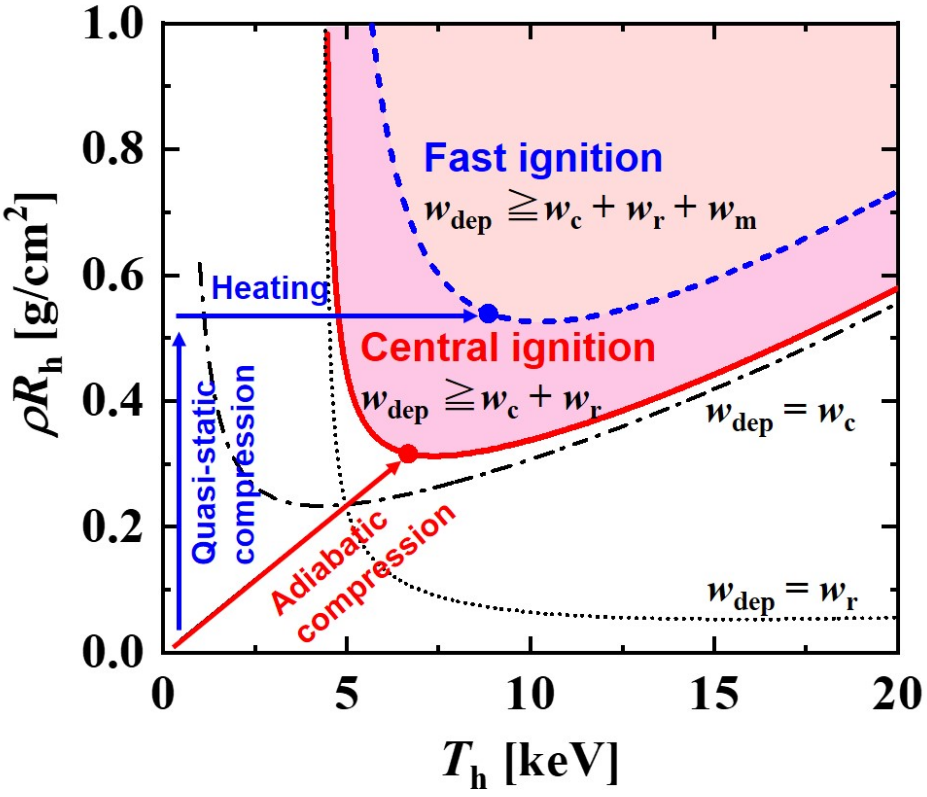

Figure 1.5: Ignition condition

1.4 Benefits of applying a strong magnetic field to fast ignition scheme

Applying a strong external magnetic fields benefit ICF in general, as well as FI. By applying an external magnetic field of about 100 T before the compression of the fusion fuel, it is expected that heat conduction from the hot ignition part to the low-temperature fuel part is reduced(reducing w_c). Therefore the temperature of the ignition part and fusion rate are increased[11]. And alpha particles generated by the fusion reaction are trapped in the fuel section by the compressed strong magnetic field.

Laboratory for Laser Energetics of Rochester University has done an implosion experiment in an external magnetic field, as shown in Fig.1.6[12]. A spherical ICF target is placed inside a coil generating an 0.8 T magnetic field. The target is imploded by the OMEGA laser. As a result of the hot-spot magnetization, the electron radial heat losses were suppressed and the observed ion temperature and neutron yield were enhanced by 15% and 30%, respectively. Further enhancement can be expected by suppressing heat conduction by stronger magnetic field.

In FI scheme, several benefits also have reported applying a strong magnetic field[13]. That scheme is called Magnetized Fast Ignition(MFI). Previous works mainly focus on reduction of the relativistic electron beam divergence by the application of the external magnetic field that means enhancement of drag heating.

[11] Perkins et al. 2013.
[12] Chang et al. 2011.
[13] Strozzi et al. 2012; Sakata et al. 2018; Bailly-Grandvaux et al. 2018.

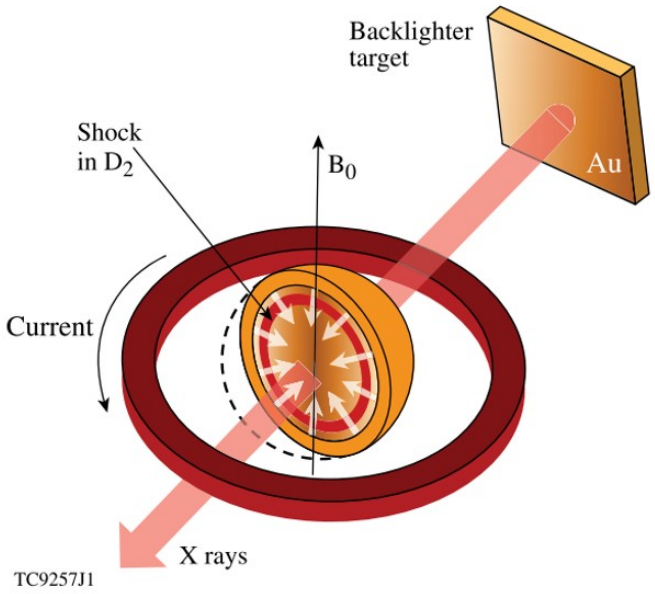

Figure 1.6: A spherical ICF target is placed inside a coil generating an 80-kG magnetic field. The target is imploded by the OMEGA laser, trapping and compressing the field inside. The figure is taken from Chang et al. 2011.

When an external magnetic field is applied along the propagation direction of the relativistic electron beam, electrons are wound around the lines of magnetic force, and the heating efficiency is increased by the electrons being guided. In our work, we report that another heating mechanism which is called diffusive heating also plays an essential role in heat the core plasma over keV range on top of the drag heating.

In MFI, a high-intensity laser is irradiated on the surface of the fuel in an external magnetic field, and the fuel is compressed with ablation pressure. Fluid instability grows during the fuel is compressed toward the center. It is important to understand hydrodynamic instabilities in a magnetic field because fluid instabilities

that occur during the compression process can result in asymmetric compression. Finally, energy is injected into the compressed fuel core from the outside using a short pulse laser of several picoseconds and heated instantaneously. The magnetic field affects the high energy density plasma in three stages: laser to ablation pressure conversion, fluid instability growth, and core heating. For these three stages, the effect of changes in heat transport in a strong magnetic field on high energy density plasma was verified in experiments. The study of the heat transport of high energy density plasma in a strong magnetic field is the key to MFI principle proof.

2. Strong magnetic field generation scheme in laser laboratories

2.1 Laser-driven capacitor coil target

A laser-driven capacitor coil target is one of the schemes for kilo-tesla level magnetic field generation in laser-plasma experiment platform such as GEKKO-XII, LULI2000, Shengguang-II, and OMEGA-EP laser facilities[1]. A fabricated laser-driven capacitor coil target used in experiment is shown Fig.2.1. The capacitor coil target is made by two disks. The intense laser pulse irradiates the first disk through the second disk with a hole. The two plates are connected by wires with the small coil. The laser pulse is absorbed at critical density. The critical density is the

[1] Law et al. 2016; Fujioka, Z. Zhang, et al. 2013; Zhu et al. 2015; Santos et al. 2015; Gao et al. 2016.

electron density at which the plasma frequency is the same as the laser frequency:

$$n_c = \frac{m_e \omega^2}{4\pi e^2} = \frac{1.1 \times 10^{21}}{\lambda^2} \mathrm{cm}^{-3} \tag{2.1}$$

For the laser with the wavelength (λ=1.053 μm) used in this study, the critical density is $1 \times 10^{21} \mathrm{cm}^{-3}$. Near the critical density, electrons are forcibly vibrated by the electric field of the laser beam. The energy of the electrons is transferred to the ions by the collision of the electrons with the ions. The repetition of this process causes the heating of the electrons and the ions. This process is called classical absorption (collisional absorption, inverse bremsstrahlung).

The laser beam incident on the plasma at an angle is refracted before reaching the critical density and is reflected. When the laser beam is incident to the short density scale length plasma (about 10 times the wavelength) as P-polarized light, the laser electric field reaches the critical density and induces an electron wave resonantly and generates hot electrons. This mechanism is called resonant absorption, and the induced electron temperature T_h can be expressed as[2]:

$$T_h = 14(I\lambda^2)^{\frac{1}{3}} T_e \tag{2.2}$$

where I is laser intensity, T_e is the electron temperature near the critical density. This temperature is generally higher than that of electrons generated by classical absorption. The electrons induced by resonant absorption make a electric potential between the capacitor disks. The potential drive the current, therefore the magnetic

[2] Tikhonchuk et al. 2017.

field is generated in the coil.

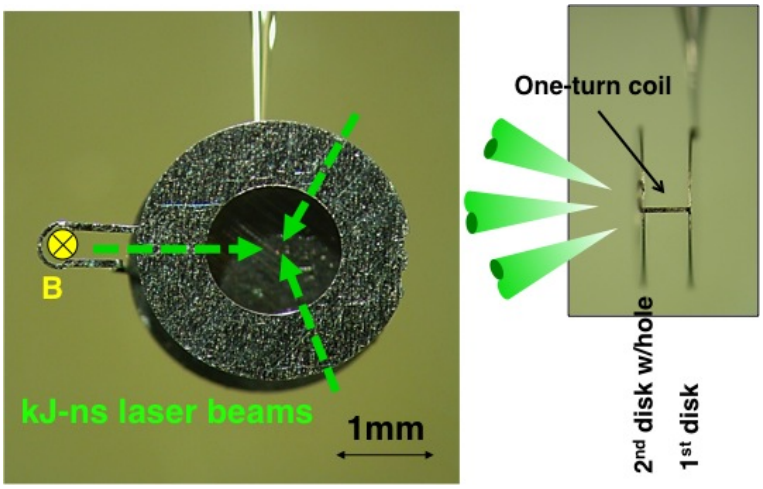

Figure 2.1: A schematic of a capacitor coil target used in experiment performed in ILE. The capacitor coil target is made by two disks. The intense laser pulse is irradiated the first disk through the second disk with a hole. The two plates are connected by wires to the small coil. In the coil, the magnetic field is generated. The figure is taken from Fujioka, Z. Zhang, et al. 2013.

The capacitor coil target have demonstrated by Daido *et al.,* in 1986[3]. Wavelength, pulse shape, pulse duration, and energy of the CO_2 laser used for driving the capacitor-coil target were 10.6 μm, Gaussian, 1.0 ns (FWHM), and 100 J in toal. The average intensity at the focal point is $1.3 \pm 0.2 \times 10^{14} \mathrm{W/cm^2}$ and the hot electron temperature generated by resonance absorption is estimated to be 15 keV. A strong magnetic field of 60 T was generated at the center of a 2 mm diameter one turn coil.

In this work, the distance between the two plates was also mentioned. A toroidal magnetic field is generated between the two plates during the laser-plasma

[3] Daido et al. 1986.

interaction by the isothermal expansion of the hot electrons, as shown in Fig.2.2(a). The toroidal magnetic field produces an outward $E \times B$ drift of the expanding electrons, which determines the optimal distance between the two plates. Critical separation distance Z_c is determined by the equation:

$$Z_c = C_{sh}\tau_L \tag{2.3}$$

where C_{sh} is the hot electron sound velocity and τ_L is the driving laser pulse duration. The relation of magnetic field amplitude and the plate separation is shown in Fig.2.2(b). In that study, the predicted value of Z_c is 600 μm, which have a good agreement with the experimental result. By fitting the experimental result, a linear relationship could be observed. When the separation is larger than Z_c, a large proportion of the expanding hot electrons could not reach the second disk and the magnetic field amplitude greatly decrease.

In the experiment in this work, the capacitor-coil target design is based on the original design. There are several changes came from experimental needs.

1. The diameter of the coil is changed from 2mm to 500 μm. We can achieve a larger magnetic field by trade-off of reducing the field area.
2. Kilo Joule class GXII laser is used for driving the capacitor coil to achieve kilo tesla level magnetic field[4].
3. The material dependency of magnetic field generated by capacitor-coil is being studied experimentally[5]. Maximum magnetic field amplitude gener-

[4] Law et al. 2016; Fujioka, Z. Zhang, et al. 2013.
[5] Santos et al. 2015.

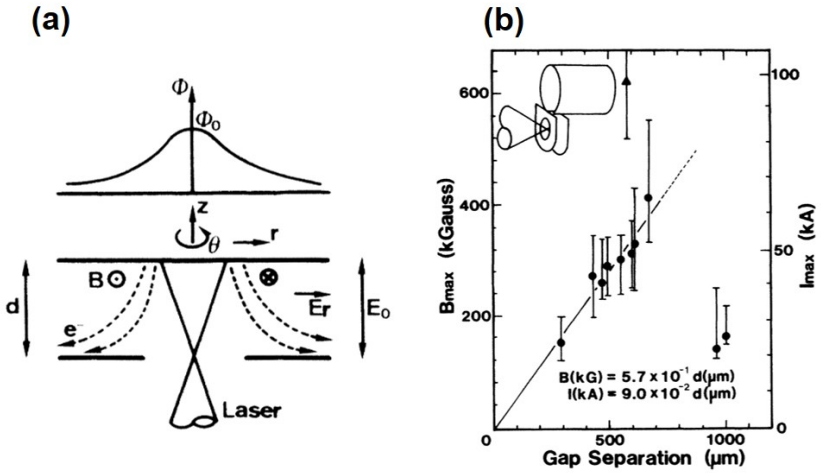

Figure 2.2: (a)The toroidal self generated magnetic field which produces an outward drift of the expanding electrons. (b)The relation of magnetic field amplitude and the plate separation. The figure is taken from Daido et al. 1986.

ated by nickel capacitor-coil is about 70% of that of copper capacitor-coil, which still have the capability to achieve kilo-tesla magnetic field. In recent years the emission lines of copper, especially the K-emission lines, are powerful tools for diagnosis during laser-plasma experiment. In order to avoid generation of copper X-ray emission during such kind of experiments, material other than copper is preferable. Therefore, instead of copper, nickel capacitor-coil is chosen in this work.

2.2 Method to measure a strong magnetic field

In this section, three methods for magnetic field measurement is briefly introduced. The first one is a differential magnetic probe (also called a B-Dot probe). It could record a long scale time evolution of the magnetic field at its position, though it should put several centimeters away from the magnetic field region because the voltage induced by the measured magnetic field exceeds its detection limits. The second one is Faraday rotation, which uses a phenomenon originating from the small difference of refractive index inside a medium, between the left-handed and right-handed circularly polarized wave. In faraday rotation measurements, the crystal should be located few millimeters from the coil, because of signal blackout due to very rapid crystal ionization induced by laser produced xray. The third one is proton deflectometry, which allows direct measurement of the magnetic field, though it can not measure the time evolution of the magnetic field in a single shot. By using different techniques, measurements with a wide range of time resolution and accuracy could be performed.

2.2.1 Differential magnetic probe

Differential magnetic probe is a type of probe coil, which utilizes Faraday's law to detect magnetic field fluctuations. Faraday's law gives the relation between electromotive force and the magnetic flux through a coil:

$$\varepsilon = -N\frac{d\phi}{dt} \tag{2.4}$$

where ε is the electromotive force, N is the number of turn of the coil, ϕ is the magnetic flux through one loop of the coil. Practically, a differential magnetic probe have three key elements: the probe tip, the probe shaft and enclosure, and the differential amplifier[6], as shown in Fig.2.3. It induces the electromotive force with the relation of equation 2.4 By measuring the voltage across the probe coil, rate of change of magnetic field could be determined. Because of the complicated structure of the differential magnetic probe, the equation2.4 is rewritten:

$$V_{out} = A\frac{dB}{dt} \tag{2.5}$$

and

$$\phi = BA \tag{2.6}$$

where V_{out} is the output voltage of the differential magnetic probe, B is the magnetic field perpendicular to the coil cross-section and A is a parameter called "equivalent sensor area" (in unit of m^2) which is sensor dependent. Practically, A is calibrated using uniform magnetic field source, performed by the manufacturer.

V_{out} is measured by using high frequency oscilloscopes. It is possible to achieve sub-ns time resolution by using oscilloscopes and the differential magnetic probe with several GHz frequencies. In a high power laser experiment, the differential magnetic probe is usually placed a few centimeters away from the maximum position because V_{out} induced by the measured magnetic field exceeds its detection limits. The differential magnetic probe cannot directly measure the laser-generated

[6] Constantin et al. 2009.

kilo-tesla magnetic field. To obtain the maximum magnetic field amplitude, one has to compute the magnetic field spatial profile analytically or numerically. In order to obtain the magnetic field strength by such an extrapolation method, it is necessary to assume the spatial profile of the magnetic field. Therefore the method is limited to magnetic field characterization using simple-shaped coils such as single-turn coils.

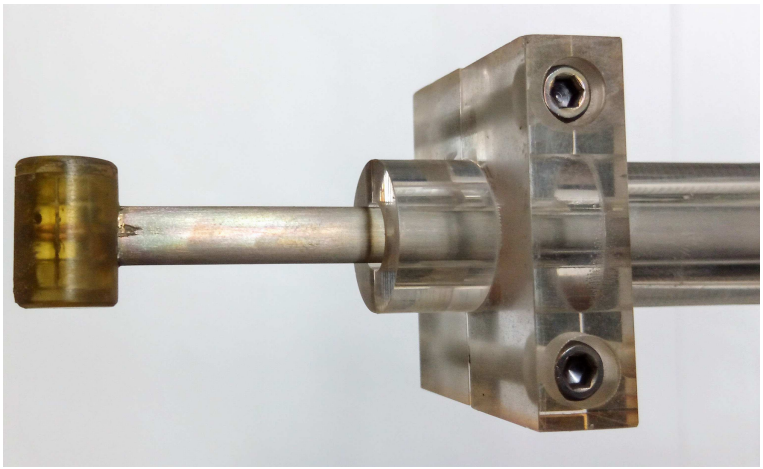

Figure 2.3: Photo of differential magnetic probe.

2.2.2 Faraday rotation

Faraday rotation comes from the fact that linearly polarized transverse waves can be decomposed into a pair of a left-handed and right-handed circularly polarized waves. A small difference of refractive index brings a small difference in phase speed between two modes under an external magnetic field along the propagation direction. It produces a rotation of the plane of polarization when a linearly-polarized electromagnetic wave passes through a medium along the direction of

the external magnetic field. The rotation of the plane of polarization in plasma medium is given by:

$$\alpha(L) = \frac{\omega_{pe}^2 \omega_{ce} L}{2c\omega^2} \tag{2.7}$$

where L is the length of medium, ω_{pe} and ω_{ce} are the plasma frequency and cyclotron frequency of electrons in plasma respectively. The ω_{pe} and ω_{ce} can be found by the relations:

$$\omega_{pe} = (\frac{n_e e^2}{\varepsilon_0 m_e})^{1/2} \tag{2.8}$$

and

$$\omega_{ce} = \frac{e|B|}{m_e} \tag{2.9}$$

where n_e is the electron density, e is the charge of electron, ε_0 is the vacuum permittivity, m_e is the electron mass and $|B|$ is absolute value of the magnetic field amplitude. Substituting equations 2.8 and 2.9 into 2.7 gives:

$$\alpha = \frac{e^3}{8\pi {\varepsilon_0}^2 c^3 {m_e}^2} n_e B_{\parallel} L \lambda^2 \tag{2.10}$$

where λ is the wavelength of the electromagnetic wave and $B_{\parallel}$ is the magnetic field component parallel to the electromagnetic wave propagation direction.

The plasma is usually inhomogeneous, which the n_e and $B_{\parallel}$ are not uniform, therefore the local $n_e B_{\parallel}$ have to be integrated along the whole path. It is difficult to measure such plasma parameters along the whole path. Therefore a crystal is usually used instead of plasma in the experiment. The rotation of polarization is

represented as:

$$\alpha = \nu B_{\parallel} L \tag{2.11}$$

where ν is an wavelength dependent constant of the crystal, called Verdet constant. Nd:YAG laser (at a wavelength of 0.532 μm) is commonly used as the probe light and fused silica(SiO_2) was used as the faraday medium with a Verdet constant of 0.298 deg / T mm at 0.532 μm. In our experiment, 500 μm thick birefringent terbium gallium garnet (TGG) crystals with its Verdet constant 11.35 deg /T mm is used. The sensitivity is 38 times higher than that of SiO_2 used in the earlier work[7], allowing to be sensitive to weaker magnetic field strengths.

Fig.2.4 shows one example of schematic of the magnetic flux density measurement with Faraday rotation. A cylinder made of fused silica, whose diameter and length are respectively 600 μm and 500 μm, is located 600 μm away from the coil. Horizontally polarized second harmonic light from an Nd:YAG laser pass throudh the fused silica. The transmitted probe light is imaged by lens 1 onto the iris. The central part of the image is selected by the iris. The image is transferred to the visible streak camera by lens 2. Heat absorption and bandpass filters are used for removing the laser harmonics and the thermal emission from the plasma. The Wollaston prism divides the rotated light into horizontal and vertical components. The rotation angle is determined from the intensity ratio between the horizontal and vertical components. From 2.11, $B_{\parallel}$ at the place of the fused silica is estimated. In the experiment the crystal are placed at position that is in distance of 1 mm order from the coil center. The distance is 1-2 order closer compared to the

[7] Fujioka, Z. Zhang, et al. 2013.

differential magnetic probe, although extrapolation is still necessary to determine the maximum magnetic field amplitude. The signal blackout due to the crystal ionization by the hard x-rays and fast particles limit the distance.

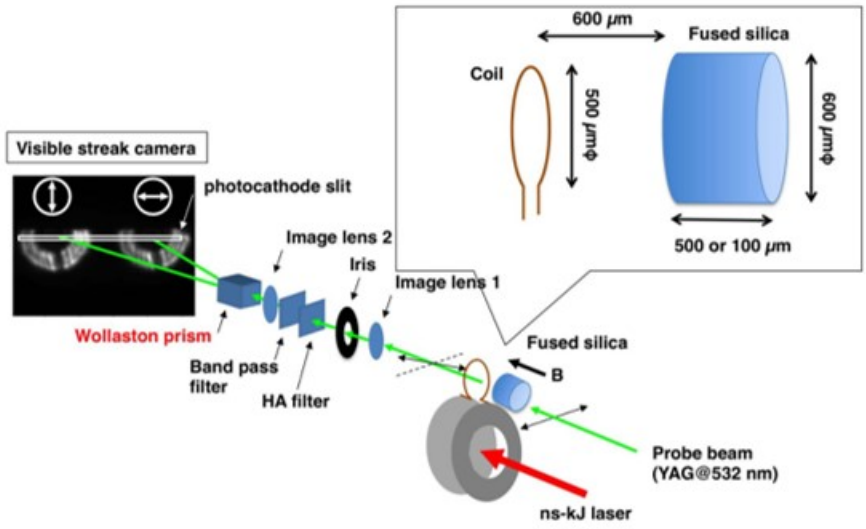

Figure 2.4: Setup of faraday rotation experiment. The figure is taken from Fujioka, Z. Zhang, et al. 2013.

2.2.3 Proton deflectometry

The differential magnetic probe and Faraday rotation method can measure only at the detection limit of the magnetic field amplitude much lower than the order of kilotesla. Therefore, extrapolation is necessary to obtain the maximum magnetic field amplitude at the center of the capacitor coil target. This means that these methods are only valid if the magnetic field profile can be modeled with very high accuracy. These methods are still promising when applied to magnetic fields generated by laser-driven capacitor coils because the magnetic field generated by a single-turn coil approximates the shape of a simple dipole field. However, it is hard to obtain information about the compressed magnetic field that can be achieved by compressing high-density plasma in ICF research due to complex spatial profile. Therefore, direct exploration of magnetic fields on the order of kilo tesla must be developed to properly evaluate such magnetic field generation schemes. From this background, approaches have been developed that use charged particle beams as magnetic field probes.

Proton is usually used as the probing particle. The potential for obtaining high-resolution images using MeV protons have been demonstrated[8]. Target Normal Sheath Acceleration(TNSA)[9] scheme with an ultra-intense ($> 10^{18}\mathrm{W/cm^2}$) laser pulse is commonly used for a particle acceleration. In TNSA process, relativistically hot electron produced by an intense laser interaction is recirculated through the thin solid target and form a cloud of relativistic electrons at the rear surface with

[8] Cobblea 2004.
[9] Passoni 2010.

a length of several Debye lengths. The strong charge separation which responsible for the intense electric field occurs in the Debye length. The electric field can effectively accelerate ions.

Proton deflectometry was performed using GEKKO-XII and LFEX laser by Law *et al.,*[10]. Fig.2.5 show the experimental setup. Each capacitor coil target was driven by a single GEKKO-XII laser beam with wavelength, pulse duration, and intensity of 1053 nm, 1.3 ns, and $2.2 \times 10^{16}\mathrm{W/cm^2}$, respectively. An LFEX laser beam with a wavelength, pulse duration, and intensity on the target of 1053 nm, 1.5 ps, and $1.1 \times 10^{19}\mathrm{W/cm^2}$, respectively, was focused on an aluminum backlight foil to generate a proton beam. TNSA produced protons with maximum energy of 35MeV are generated within time interval that is comparable with the laser pulse duration.

Proton generation point was 2 mm away from TCC, and a 35-layer radiochromic film (RCF) stack was placed at 20 mm from TCC to record proton beam pattern after travelling through the magnetic field. Fig.2.6 show deflected proton patterns detected on RCF and calculated with the Monte-Carlo simulation. Lorentz force due to the fringing field around the coil wire produces an umbrella-like proton pattern. By comparing the separation distance of the two high intensity points of umbrella-like proton pattern with the experimental data, the magnetic field is estimated to be 610T at center of each capacitor coil.

[10]Law et al. 2016.

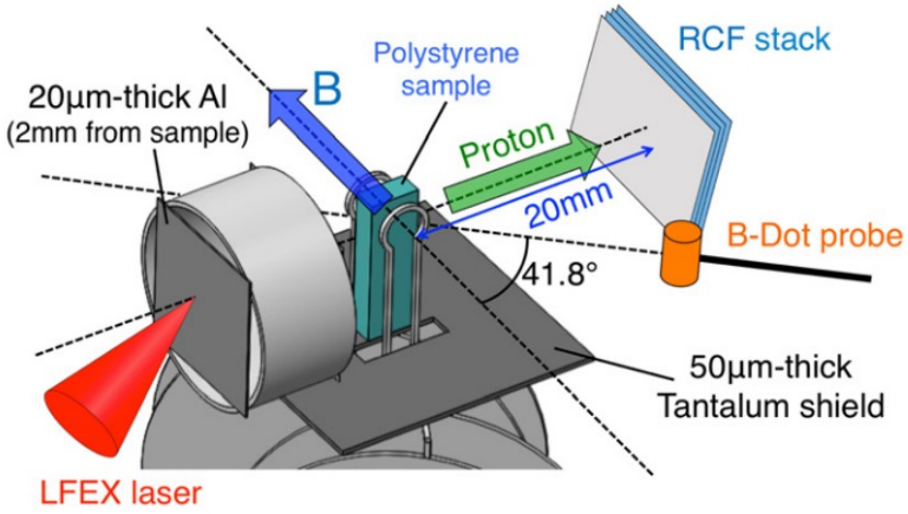

Figure 2.5: Experimental layout of proton deflectometry. Two laser-driven capacitor-coil targets are used for generating a magnetic field. The proton beam propagates perpendicular to the magnetic field direction and the is detected on an RCF stack. The figure is taken from Law et al. 2016.

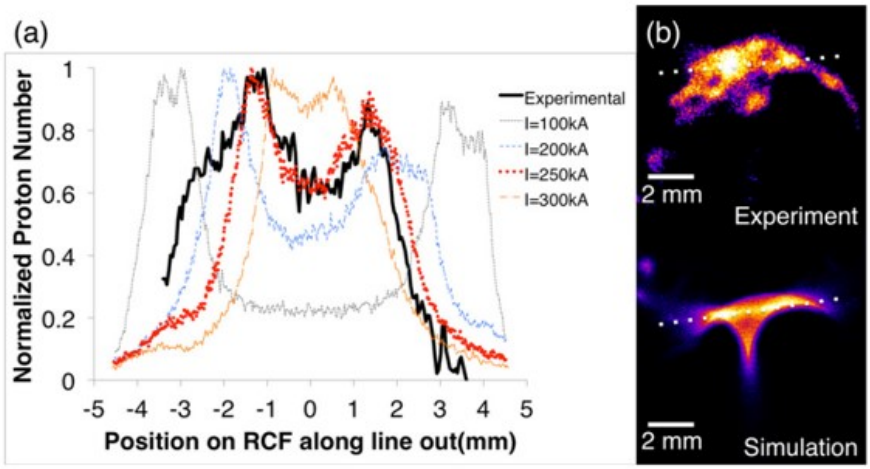

Figure 2.6: Deflected proton patterns detected on RCF and calculated with the Monte-Carlo simulation. Lorentz force due to the fringing field around the coil wire produces an umbrella-like proton pattern. The line profile for 250kA (610 T field amplitude, red dotted line) shows the best agreement with the experimental result (black solid line). The figure is taken from Law et al. 2016.

3. Effect of anisotropic thermal transport in a strong magnetic field on hydrodyanmics

3.1 Introduction

Magnetohydrodynamics (MHD) of a high-energy-density plasma (HEDP) in an external magnetic field involve fundamental physics relevant to the fields of astronomy and solar physics and inertial confinement fusion. On the aspect of magnetized laser fusion research, several authors reported interesting and important HEDP phenomena in a strong magnetic field. Chang *et al.*, reported that electron radial heat losses from the hot-spot to the surrounding cold fuel were suppressed by embedding axial magnetic field in a plastic capsule[1]. Perkins *et al.*, found that application of strong magnetic field to fusion targets relaxes ignition requirements

[1] Chang et al. 2011.

in two-dimensional (2D) hydrodynamic simulations[2]. Strozzi *et al.*, showed guiding of relativistic electrons generated by intense laser-plasma interactions with kilo-tesla magnetic field by 2D hybrid simulations[3]. The growth or suppression of hydrodynamic instabilities in an external magnetic field have been studied theoretically and numerically. However, a few fundamental experiments have been performed in this research area, mainly due to the lack of a strong magnetic field source. Recent significant progress of generation in laboratory of a strong magnetic field enables us to investigate experimentally unexplored MHD phenomena of a HEDP.

Assuming a single fluid and two-temperature plasma, MHD dynamics of a laser-produced plasma can be described as:

$$\frac{\mathrm{d}\rho}{\mathrm{d}t} = -\rho\nabla\cdot\mathbf{u}, \tag{3.1}$$

$$\rho\frac{\mathrm{d}\mathbf{u}}{\mathrm{d}t} = -\nabla(P_{\mathrm{th}}+\frac{\mathbf{B}^2}{8\pi})+\frac{1}{4\pi}(\mathbf{B}\cdot\nabla)\mathbf{B}, \tag{3.2}$$

$$\rho\frac{\mathrm{d}\varepsilon_i}{\mathrm{d}t} = -P_i\nabla\cdot\mathbf{u}-\nabla\cdot q_i+Q_{ei}, \tag{3.3}$$

$$\rho\frac{\mathrm{d}\varepsilon_e}{\mathrm{d}t} = -P_e\nabla\cdot\mathbf{u}-\nabla\cdot(\kappa\cdot\nabla T_e)-Q_{ei}+S_L+S_r, \tag{3.4}$$

where ρ and $\mathbf{u}$ are mass density and fluid velocity of a plasma; ε_i, ε_e, P_i and P_e are the energy and pressure of ion and electron. q_i is the ion heat flux, and Q_{ei} is the term for ion-electron relaxation. The term S_L and S_r describe the energy transfer from laser and radiation. (3.1) - (3.4) describe the mass, momentum, ion energy

[2] Perkins et al. 2013.
[3] Strozzi et al. 2012.

and electron energy conservations in a plasma transport with an external magnetic field.

The influence of magnetic field can be revealed by two ways. Firstly, the velocity of plasma is directly affected by the magnetic field presssure $\nabla(\mathbf{B}^2/8\pi)$ and magnetic tension force $\frac{1}{4\pi}(\mathbf{B}\cdot\nabla)\mathbf{B}$, in (3.2). Both term come from Lorentz force ($\mathbf{j}\times\mathbf{B}$). The direct effect of the magnetic field on the plasma hydrodynamics is evaluated with the dimensionless parameter $\beta = P_{\rm th}/P_{\rm mag}$, i.e., the ratio between the plasma pressure ($P_{\rm th} = n_e k_B T_e$) and magnetic field pressure ($P_{\rm mag} = B^2/8\pi$):

$$\beta = 4.0\left(\frac{B}{100\mathrm{T}}\right)^{-2}\left(\frac{T_e}{100\mathrm{eV}}\right)\left(\frac{n_e}{10^{21}\mathrm{cm}^{-3}}\right) \tag{3.5}$$

When β is less than 1 which means the magnetic pressure is higher than the plasma pressure, it is possible to control the plasma with the magnetic field. On the other hand, when β is greater than 1, the plasma pressure is more dominant than the magnetic field pressure. β is evaluated to be more than 10 with typical plasma parameters in HEDP experiment. The contribution of the magnetic field pressure is negligibly small.

Secondly, plasma pressure($P_{\rm th}$) is changed due to the suppression of heat transport in a magnetic field. In (3.4), κ is the tensor for thermal conductivity. Assuming a two dimensional transport, κ is described as:

$$\kappa\cdot\nabla T_e = \kappa_\parallel\nabla_\parallel T_e + \kappa_\perp\nabla_\perp T_e + \kappa_\wedge\mathbf{h}\nabla T_e, \tag{3.6}$$

$$\kappa_\parallel = \gamma_0\left(\frac{n_e T_e \tau_e}{m_e}\right) = \gamma_0\kappa_0, \tag{3.7}$$

$$\kappa_{\perp} = \kappa_0 \frac{\gamma_1' \chi^2 + \gamma_0'}{\triangle}, \tag{3.8}$$

$$\kappa_{\wedge} = \kappa_0 \frac{\chi\left(\gamma_1'' \chi^2 + \gamma_0''\right)}{\triangle} \tag{3.9}$$

where χ is Hall parameter, and $\triangle = \chi^4 + \delta_1 \chi^2 + \delta_0$. γ_1', γ_0', δ_1 and δ_0 are the Braginskii coefficients[4], which values are refined with the magnetic field. From (3.6) - (3.9), thermal conductivity perpendicular to magnetic field can be simplified:

$$\kappa_{\perp} \approx \frac{\kappa_0}{\sqrt{1+\chi^2}} \tag{3.10}$$

and

$$\chi = \omega_{ce}\tau_{ei} = 1.3 \left(\frac{B}{100\mathrm{T}}\right) \left(\frac{T_e}{100\mathrm{eV}}\right)^{\frac{3}{2}} \left(\frac{n_e}{10^{21}\mathrm{cm}^{-3}}\right)^{-1} \tag{3.11}$$

Here, Coulomb logarithm($\ln\Lambda$ = 4.8) is used for 100eV, $10^{21}\mathrm{cm}^{-3}$ plasma[5]. By applying a magnetic field of about 100T, the Hall parameter easily becomes more than unity at the ablation region. When Hall parameter has nonzero value, the thermal conductivity reduce in the external magnetic field owing to (3.10) and the anisotropic thermal diffusion is formed. Because anisotropic thermal diffusion reduces thermal energy loss from the ablated plasma to its peripheral cold region, temperature and thermal pressure of the ablated plasma increases significantly.

In this study, a well-characterized basic experiment in a simple geometry can be performed with a spatially uniform strong magnetic field generated by using a pair of laser-driven capacitor coil targets. The magnetic field changes its shape due

[4] Braginskii 1965.
[5] Stefano 2003.

to the magnetic field transport equation described by:

$$\begin{aligned}\frac{\partial \mathbf{B}}{\partial t} &= \nabla \times (\mathbf{V_i} \times \mathbf{B}) + \frac{c}{e}[\nabla \times (\frac{\nabla p_e}{n_e}) - \nabla \\ &\quad \times \{\frac{(\nabla \times \mathbf{B}) \times \mathbf{B}}{4\pi n_e}\} - \nabla \times (\frac{\mathbf{R_u} + \mathbf{R_T}}{n_e})], \end{aligned} \tag{3.12}$$

where $\mathbf{B}$, $\mathbf{V_i}$, c, p_e and n_e are the magnetic field, ion velocity, speed of light, electron pressure and electron number density, respectively. The first term in (3.12) denotes the convection of the magnetic field flux by the ion motion. The second term is the self-generated magnetic field term caused by the nonparallel ∇T_e and ∇n_e, which is called Biermann battery effect. The third term $\nabla \times \{((\nabla \times B) \times B)/(4\pi n_e)$ is the Hall term which is caused by $\mathbf{j} \times \mathbf{B}$. $\mathbf{R_u}$ is the so-called diffusion term of the magnetic field. $\mathbf{R_T}$ is thermal force term which is called Nernst effect. The Nernst effect causes convective amplification of magnetic field in a region with large temperature gradients such as near laser ablation region[6].

Magnetic-Reynolds-number $Re_{\mathrm{m}} = \tau_{\mathrm{diffusion}}/\tau_{\mathrm{hydrodyanmics}}$, the ratio of the magnetic field's diffusion time $\tau_{\mathrm{diffusion}}$ to the hydrodynamic time scale $\tau_{\mathrm{hydrodynamics}}$, is an important parameter for dynamics of magnetic field associated with $\nabla \times (\mathbf{V_i} \times \mathbf{B})$ and $\mathbf{R_u}$ in (3.12). $\tau_{\mathrm{diffusion}} = 4\pi\sigma L^2/c^2$, where σ is the conductivity and L is the typical plasma scale. For example, in a 300-eV polystyrene plasma, $\tau_{\mathrm{diffusion}} > 10$ ns, and the hydrodynamics time scale is L/C_{S} $\sim 100\ \mu$m/10^7 cm/s = 1 ns, here C_{S} is a sound velocity of a plasma. $\mathrm{Re_m}$ is about 10 for this plasma. Therefore magnetic field fluxes freeze in a plasma, and the

[6] Nishiguchi et al. 1984.

field structure is changed by plasma motion. The external magnetic field flows associated with the plasma motion owing to its large magnetic Reynold's number.

In this section, we described the experimental investigation of unexplored magnetohydrodynamics phenomena of a high-energy-density plasma, which an external magnetic field of 200-300 T notably affects due to anisotropic thermal conduction, even when the magnetic field pressure is much lower than the plasma pressure. The experiments were performed with planar targets in the following magnetic field geometries: $B_{\parallel}$ is an external magnetic field with direction parallel to the growth direction of the instability and $B_{\perp}$ is an external magnetic field with direction perpendicular to the growth direction of the instability. The external magnetic field reduces electron thermal conduction across the external magnetic field lines because the Larmor radius of the thermal electrons in the external magnetic field is much shorter than the mean free path of the thermal electrons. The velocity of a thin polystyrene foil driven by intense laser beams in the strong external magnetic field is faster than that in the absence of the external magnetic field. Growth of sinusoidal corrugation imposed initially on the laser-driven polystyrene surface is enhanced by the external magnetic field because the plasma pressure distribution becomes nonuniform due to the external magnetic-field structure modulated by the perturbed plasma flow ablated from the corrugated surface. These observations were reproduced by two-dimensional radiation-hydrodynamic simulations (PINOCO-MHD). Details are given in the following sections.

3.2 Characterization of a strong magnetic field in helmholtz geometries

A basic experiment in a simple geometry can be performed with a spatially uniform strong magnetic field generated by using a pair of laser-driven capacitor coil targets as a helmholtz-type arrangement. For simplicity, the experiments were performed with a planar target in two magnetic field geometries: $B_{\parallel}$ or $B_{\perp}$ are the external magnetic fields with directions parallel or perpendicular to the plasma motion, respectively, as shown in Fig. 3.1 (a) and (b). In this study, two capacitor coil targets with a diameter of 1500 μm are separated by 900 μm around a polystyrene target. The first nickel-disk is irradiated through the hole in the second nickel disk by the GEKKO-XII laser having 1.5 $\pm$ 0.1 kJ, a Gaussian shape with 1.2 ns of full width at half maximum (FWHM), and an intensity of around 1.5 $\times$ 10^{15} W/cm^2. A plasma is generated at the first disk, and suprathermal hot electrons with temperatures exceeding 10 keV are generated in the plasma corona. The hot electrons move ahead of the expanding plasma plume and are accumulated on the second disk. The second disk acquires negative charges, and a large electrical potential develops between the disks. That potential difference drives a current in the coil. A strong magnetic field pulse is generated in the coil, the coils are destroyed after every laser shot.

The magnetic flux density was characterized using a three-axis differential magnetic probe[7] and Faraday rotation with a terbium gallium garnet (TGG) crystal

[7] Everson et al. 2009.

as the magneto-optical material. The differential magnetic probe and TGG crystal were placed 70 mm and 4 mm away from the coil center, respectively. The Faraday rotator (a piece of TGG) makes significant noise in the differential magnetic probe signal, we did not use simultaneously both Faraday rotation and differential magnetic probe in the shots. Generation mechanism of the noise is not understood. The magnetic flux densities were reconstructed using the RADIA code[8] to evaluate the current inside the coil and the magnetic field structure around the target position, as shown in Fig. 3.1 (c) and (d). The results are summarized in Table 3.1. Since the position of the differential magnetic probe is farther away, the value of the observed magnetic field strength is smaller. Comparing the strength of the magnetic field at the center of the coil calculated from the strength of the magnetic field at the observation point, the strength of the magnetic field was observed within a 15% error range even when using two measurement methods with different measurement principles.

The average flux density of $B_{\parallel}$ and $B_{\perp}$ at the midpoint between the coils were 215 ± 21 T and 350 ± 19 T, respectively. The errors on the B-field measurement mainly came from build-variations of the coils. The build-variations affect laser spot size and beam pointing on the first disk. The difference between the $B_{\parallel}$ and $B_{\perp}$ strengths may have been due to the difference in the coil inductance and resistance. It is necessary to change coil shapes to produce $B_{\parallel}$ and $B_{\perp}$ geometries because all laser beams come from one direction in our laser facility. Assuming that the potential difference occurs instantaneously in the capacitor, the equation of the RL

[8] RADIA n.d.

circuit holds:

$$V = RI(t) + L\frac{\mathrm{d}I}{\mathrm{d}t} \tag{3.13}$$

and

$$I(t) = \frac{V}{R}(1 - \exp(-\frac{L}{R}t)) \tag{3.14}$$

Assuming a current in a quasi-static magnetic field, $I = V/R$. The strength of the magnetic field $B^2 = LI^2$, therefore $B^2 = LV^2/R^2$. The potential difference V of the capacitor part of the capacitor coil does not depend on the arrangement because it has the same shape even if the arrangement is changed. The discrepancy between the magnetic field strengths of $B_{\parallel}$ and $B_{\perp}$ may be due to the difference of L/R^2. As the result of the difference of the coil shape, inductance and resistance of the $B_{\perp}$ geometry coil are 1.33 and 0.87 times those of $B_{\parallel}$ one. The differences of inductance and resistance correspond to $B_{\parallel}/B_{\perp}$ = 1.33 calculated with a simple circuit model, this is not inconsistent with the experimental value ($B_{\parallel}/B_{\perp}$ = 1.63 $\pm$ 0.18), however, there may be other unrecognized differences. Fig. 3.2 shows time evolution of the magnetic field measured by Faraday rotation. The magnetic field generated by the laser-driven capacitor coil peaks 1.5 ns after laser irradiation and has a duration of about 1 ns.

3.3 Anisotropic thermal flow in ablation region

Figure 3.3 (a) and (b) show top and face views of the target used in the trajectory measurement. A 25-μm-thick polystyrene (C_8H_8) foil was irradiated by the laser

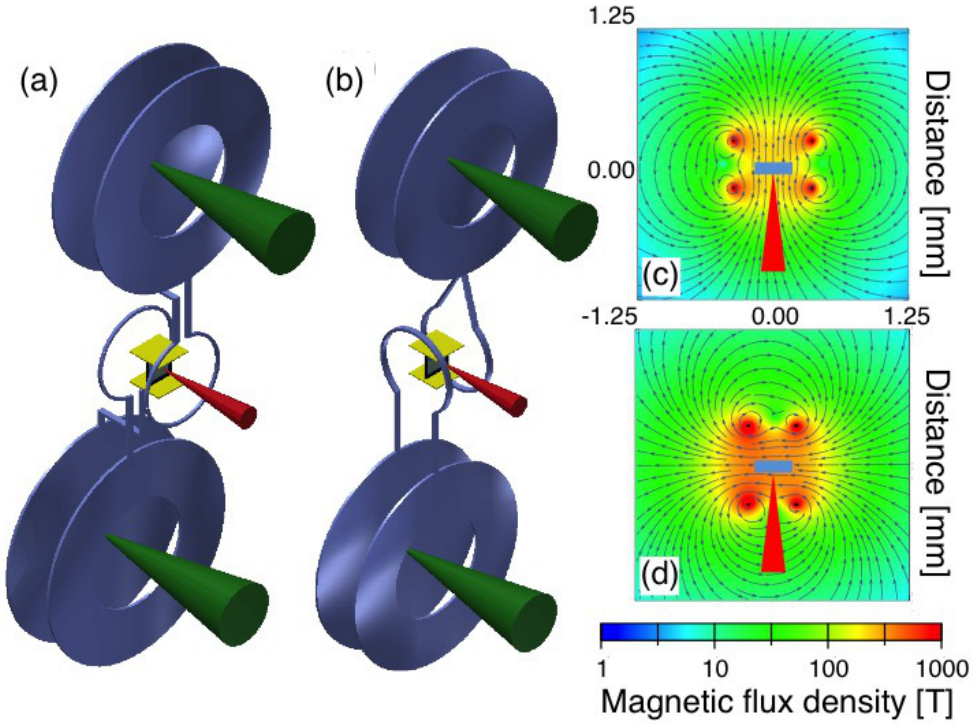

Figure 3.1: Experimental configurations for studying the hydrodynamics of HEDPs in an external magnetic field. (a) Experimental setup for the $B_{\parallel}$ geometry, in which the magnetic field lines are parallel to the ablated plasma motion. (b) Experimental setup for the $B_{\perp}$ geometry, in which the magnetic field lines are perpendicular to the ablated plasma motion. 50-μm-thick tantrum plates are put at the bottom and top of the polystyrene foils to prevent the polystyrene foils from preheating by X rays generated at the capacitor plates. Magnetic field structures computed using the RADIA code for the (c) $B_{\parallel}$ and (d) $B_{\perp}$ geometries.

Shot ID	Geometry	E_L	I_L	B@measure	B@center	I_c	Methods
		J	W/cm^2	T	T	kA	
38043	$B_{\parallel}$	1263	1.49×10^{15}	1.4	206	210	Faraday
38047	$B_{\perp}$	1267	1.49×10^{15}	0.00407	349	295	B-dot
38051	$B_{\parallel}$	1266	1.49×10^{15}	0.00417	239	244	B-dot
38054	$B_{\parallel}$	1306	1.54×10^{15}	0.00350	201	205	B-dot
38055	$B_{\perp}$	1316	1.55×10^{15}	0.0388	332	281	B-dot
38056	$B_{\perp}$	1308	1.54×10^{15}	0.00430	369	312	B-dot

Table 3.1: Summary of magnetic flux density and current in the coil.

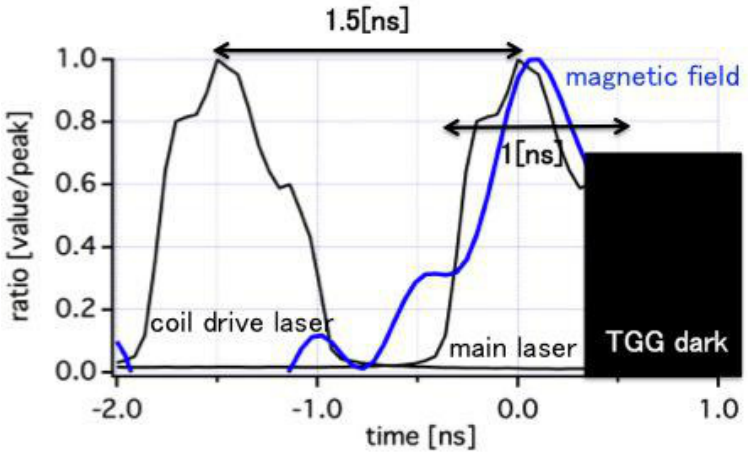

Figure 3.2: Time evolution of the magnetic field measured by Faraday rotation. The magnetic field generated by the laser-driven capacitor coil peaks 1.5 ns after laser irradiation and has a duration of about 1 ns.

beams midway between the two coils. 50-μm tantrum plates are put at the bottom and top of the polystyrene foil as shown in Fig. 3.1 (a) and (b) to prevent the polystyrene foil from preheating by X rays generated at the capacitor parts. Three 351-nm beams of the GEKKO-XII laser were used to drive the foil with an intensity of $4.0 \pm 0.1 \times 10^{13}$ W/cm^2. The magnetic field strength reaches its peak at 1.5 ns after the peak of the magnetic field generation laser pulse, this is same as the result in Ref.[9]. The external magnetic field must diffuse into the polystyrene foil before the foil acceleration, therefore the drive laser beams were delayed by 1.5 ns with respect to the magnetic field generation beams.

Figure 3.3 (c), (d), and (e) show shadows of the laser-driven polystyrene foils that were observed using an X-ray streak camera and the side-on backlighting. The backlight was 1.2 keV X rays emitted due to M-shell to L-shell transitions of

[9] Law et al. 2016.

bounded electrons of Cu ions in a laser produced Cu plasma. The pulse duration of the backlight X rays was 1.2 ns. The spatial and temporal resolutions of the X-ray imaging system were measured to be 13 μm and 40 ps, respectively. The width of the polystyrene foil along the line of sight of the diagnostics was $l = 150$ μm. When the 1.2 keV X rays pass through the target with the initial intensity I_0, the intensity after passing through the target I is calculated by $I = I_0 e^{-\mu\rho l}$ where $\mu = 630\,\mathrm{cm}^2/\mathrm{g}$ and $\rho = 1.1\,\mathrm{g}/\mathrm{cm}^3$ are mass absorption rate of a polystyrene for the 1.2 keV X rays and mass density. The target reduces the initial X-ray intensity by a factor of 10^{-4}. Therefore, when this X-ray is imaged by an X-ray streak camera, an image with low brightness is obtained at the part that has passed through the polystyrene plate. The X-ray streak camera records the position of the polystyrene plate for 1.89 ns. The flying velocity can be estimated from the slope of the shadow.

The flying velocity of the rear surface accelerated in the $B_{\parallel}$ and $B_{\perp}$ fields are 1.5 times faster than in the absence of an external magnetic field as shown in Fig. 3.3 (f), (g), and (h). This acceleration mechanism is discussed below. The magnetic field generated by the Biermann battery effect[10] is estimated to be 10 T in this experiment. The self-generated field contribution is relatively small compared to the external magnetic field. Only external magnetic field is considered in the following discussions.

The direct effect of the magnetic field on the plasma hydrodynamics is evaluated with the dimensionless parameter $\beta = P_{\mathrm{plasma}}/P_{\mathrm{mag}}$, i.e., the ratio between the

[10] Manuel et al. 2012; Srinivasan and Tang 2012.

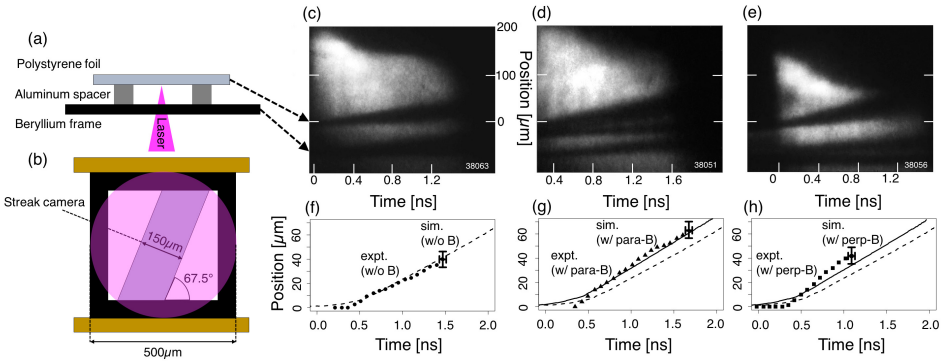

Figure 3.3: (a) Top view of the target used in a trajectory measurement. A 25 μm-thick polystyrene foil was mounted on a 25 μm-thick beryllium frame. A 50-μm-thick aluminum spacer was inserted between the foil and frame. (b) Face-view of a target used in the trajectory measurement. The width of the polystyrene foil was 150 μm along the line of sight of the diagnostics. The polystyrene foil and the beryllium frame are irradiated by the 500 μm diameter laser beam. Shadow of laser-driven polystyrene foils measured using side-on X-ray backlighting in (c) no external magnetic field, (d) $B_{\parallel}$ and (e) $B_{\perp}$ geometries. The rear surface of laser-driven polystyrene foils (black points) are compared with the results of simulations carried out using the PINOCO-MHD code for (f) no external magnetic field and the (g) $B_{\parallel}$ and (h) $B_{\perp}$ geometries. The solid black and dashed lines are PINOCO-MHD calculations with and without consideration of the external magnetic field, respectively. The origins of the axes are defined as the laser peak timing and initial position of the target rear surface.

plasma pressure (P_{plasma}) and magnetic field pressure ($P_{\mathrm{mag}} = B^2/8\pi$). β value is evaluated to be about 50 with typical plasma parameters in this experiment. The contribution of the magnetic field pressure is negligibly small to the plasma acceleration.

The other important parameter is the Hall parameter $\chi = \omega_{\mathrm{ce}}\tau_{\mathrm{e}}$, where ω_{ce} and τ_{e} are the electron gyrofrequency and electron collision time, respectively. For a 300-eV polystyrene plasma and a 200-T external magnetic field, the Hall parameter

is close to unity. When the Hall parameter is non-zero, the external magnetic field reduces the electron thermal conduction across the external magnetic field lines because the Larmor radius of the thermal electrons in the external magnetic field is much shorter than mean-free-path of the thermal electrons. The electron temperature increment is modified by the magnetic field through the anisotropic thermal conductivity.

The magnetic Reynolds number $Re_{\rm m} = \tau_{\rm diffusion}/\tau_{\rm hydrodynamics}$ is the ratio of the magnetic field diffusion time ($\tau_{\rm diffusion}$) to the hydrodynamic time scale ($\tau_{\rm hydrodynamics}$). This dimensionless parameter is important for understanding the dynamics of the magnetic field associated with plasma motion. $\tau_{\rm diffusion} = 4\pi\sigma L^2/c^2$, where σ is the conductivity of the plasma and L is the typical plasma scale. For example, in a 300-eV polystyrene plasma, $\tau_{\rm diffusion} > 10$ ns, and the hydrodynamic time scale is $L/C_{\rm S} \sim 100\ \mu$m/$10^7$ cm/s = 1 ns, where $C_{\rm S}$ is the sound velocity of a plasma. $Re_{\rm m}$ is about 10 for this plasma. Therefore, magnetic field fluxes are frozen in the plasma, and the field structure changes with the plasma motion. The external magnetic field moves with the plasma flow owing to its large Re_m.

We performed two-dimensional radiation-hydrodynamic simulations (PINOCO-MHD) with and without an external magnetic field. The models used in the PINOCO-MHD code are described in the references[11]. The thermal conductivity becomes anisotropic in both the $B_{\parallel}$ and $B_{\perp}$ cases in the simulation. Because anisotropic thermal diffusion reduces the thermal energy loss from the ablated

[11] Nagatomo, T. Johzaki, Sunahara, et al. 2013; Nagatomo, T. Johzaki, T. Asahina, et al. 2015.

plasma to its cold peripheral region that is transverse to the $B_{\parallel}$ field lines, the temperature and pressure of the ablated plasma increase significantly, resulting in acceleration of the polystyrene foil by the larger pressure gradient (Figs. 3.4 (a), (c) and (e)).

The situation is more complex for the $B_{\perp}$ geometry than that for the $B_{\parallel}$ geometry. There is shear flow in the ablated plasma that is perpendicular to the $B_{\perp}$ field lines, because ablated plasma flow directed along the target normal within the laser spot region is faster than that in its cold periphery. The $B_{\perp}$ lines are bent and $B_{\parallel}$ component appears at the edge of the target. Thermal energy loss from the ablated plasma to its cold peripheral region is reduced in this magnetic field structure, the temperature and pressure of the ablated plasma increase significantly, resulting in acceleration of the polystyrene foil by the larger pressure gradient (Figs. 3.4 (b), (d) and (f)).

In the $B_{\perp}$ geometry, the measured trajectory is faster than calculated one. This different may be caused by the Nernst effect. The Nernst effect causes convective amplification of magnetic field in a laser-produced plasmas near the ablation surface[12]. In the $B_{\perp}$ case, the direction of the external magnetic field are perpendicular to the direction of thermal electrons that flow from the high temperature region to the low temperature one. These electrons receive force from the external magnetic field and create an electric field. This electric field drive the current. The magnetic field made by the current causes the convective amplification of a magnetic field near the ablation surface, this increases anisotropic thermal conduction in a plasma.

[12] Nishiguchi et al. 1984.

The Nernst effect can not been taken into account in the PINOCO-MHD, because this effect is three-dimensional effect. The present PINOCO-MHD simulation does not explain completely the experimental results obtained in the $B_{\perp}$ cases because of the Nernst effect. In the $B_{\parallel}$ geometry, the direction of the electrons that move from the high temperature to the low temperature side and the direction of the external magnetic field are parallel. Therefore the Nernst effect is not effective in the $B_{\parallel}$ geometry.

3.4 Enhancement of perturbation growth in a strong magnetic field

The hydrodynamic perturbation growth is also affected by the external magnetic field as a result of the anisotropic thermal conductivity in the ablated plasma. The Rayleigh Taylor instability which is a famous mechanism of the hydrodynamic perturbation growth is caused by gravity on the surface of polystyrene foil[13]. Numerous studies of the RTI have been done. The essence is described below. The target density ρ_1 is larger than the plasma density ρ_2 around the target. During the acceleration, a dense substance is on a medium of low density, and interfaces of different densities are in a state of gravitational instability. This gravitational instability is called Rayleigh-Taylor instability. When considering the force acting

[13] Zhou 2017.

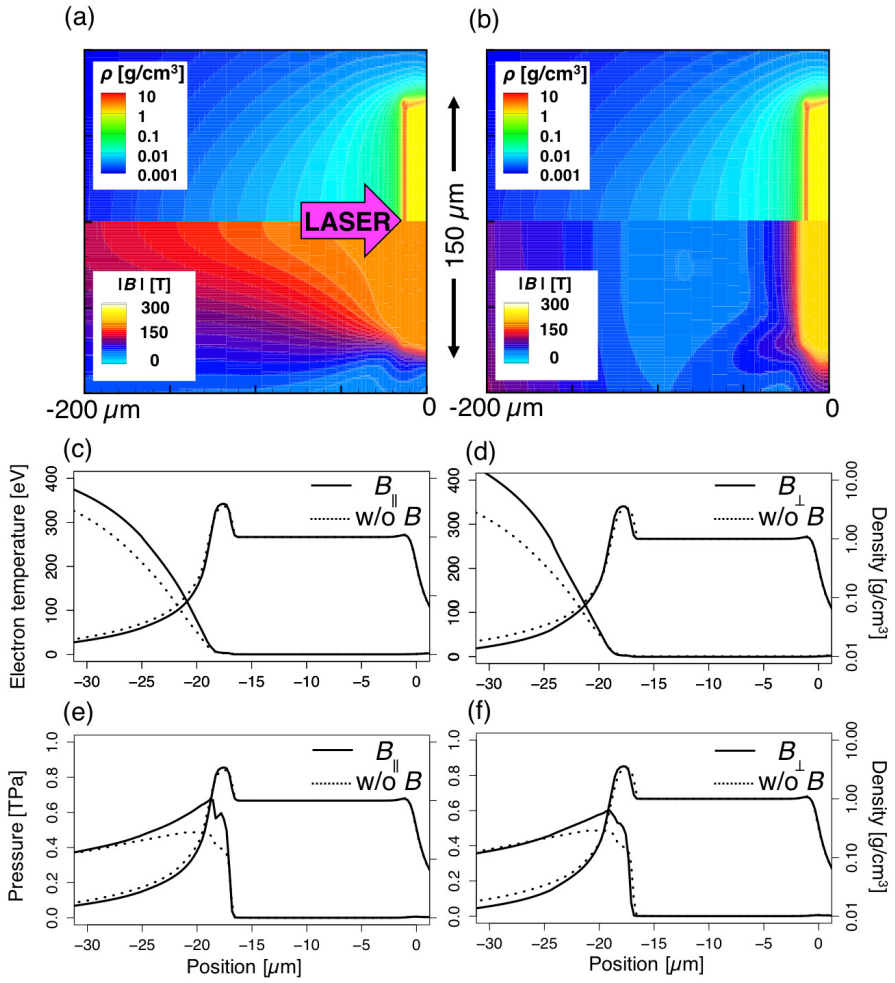

Figure 3.4: Two-dimensional mass density and magnetic flux density distributions at the laser peak timing for (a) $B_{\parallel}$ and (b) $B_{\perp}$ cases. The origin of the position is defined as the initial position of the target rear surface. Electron temperature and pressure profiles along the target center axis are shown in (c),(d),(e), and (f). Electron temperature (solid lines) of the ablated plasmas increases notably in the external magnetic field due to anisotropic thermal conduction as shown in (c) $B_{\parallel}$ and (d) $B_{\perp}$ compared to that without magnetic field (dotted lines). Pressure (solid lines) of the ablated plasmas also increases in the external magnetic field,as shown in (e) $B_{\parallel}$ and (f) $B_{\perp}$ compared to that without magnetic field (dotted lines).

on this target, it is enough to consider the difference between buoyancy and gravity:

$$m\ddot{a} = (\rho_1 - \rho_2)ag \tag{3.15}$$

And the momentum of this interface can be described:

$$P = \int_{-\infty}^{\infty} \rho v(z) dz \tag{3.16}$$

Here, z is defined as the direction in which the target is accelerated. From $\nabla \times v(z) = 0$ for a vortexless flow, $v(z)$ can be written as $v = \nabla\phi$ using the velocity potential ϕ. If it is an incompressible fluid, from $\nabla \cdot v(z) = 0$:

$$\begin{aligned} \nabla^2\phi &= 0 \\ &= \frac{\partial^2\phi}{\partial^2 y} + \frac{\partial^2\phi}{\partial^2 z} \\ &= -k^2 f(z)\cos(ky) + f''(z)\cos(ky) \end{aligned} \tag{3.17}$$

Where $v(z)$ that satisfies the expression 3.17 is:

$$\dot{a}\exp(-k|z|)\cos(ky) \tag{3.18}$$

Substituting the expression 3.18 into the expression 3.16 and executing integration:

$$\begin{aligned} P &= \int_0^{\infty} \rho_1 \dot{a}\exp(-k|z|)dz + \int_{-\infty}^{0} \rho_2 \dot{a}\exp(-k|z|)dz \\ &= (\rho_1 + \rho_2)\frac{\dot{a}}{k} \end{aligned} \tag{3.19}$$

Since this time change $\dot{P}$ is equal to the expression 3.15:

$$\frac{d^2a}{dt^2} = kgA_Ta \tag{3.20}$$

is obtained. Where $A_T = (\rho_2 - \rho_1)/(\rho_2 + \rho_1)$ is called the Atwood number. k is the wave number of the disturbance, g is the acceleration. The time evolution of the disturbance amplitude is as follows:

$$a(t) = a_0 \exp(\sqrt{kgA_T}t) \tag{3.21}$$

In the acceleration phase, the disturbance grows exponentially due to RT instability.

To simplify the situation, we used the planar polystyrene foils which have a 50 μm wavelength sinusoidal perturbation with initial amplitude a_0 = 1.6 or 3.2 μm whose initial thickness l_0 = 16 or 25-μm in the experiment. Two capacitor-coil targets were arranged in the $B_{\parallel}$ geometry, and the corrugated polystyrene foil was located at the midpoint between the two coils. Face-on X-ray backlighting coupled with an X-ray streak camera was used to measure the temporal evolution of the areal density modulations ($\Delta\rho a$) amplified by the hydrodynamic instability from X-ray intensity ratio between the peak (I_{peak}) and valley (I_{valley}) of an image as $\Delta\rho a = \ln(I_{\text{peak}}/I_{\text{valley}})/2\mu$, here μ = 607 g/cm^2 is the mass absorption rate of a polystyrene for the X rays. Laser-produced Zn plasmas were used as the X-ray backlighting sources, which emit relatively broad L-shell X rays centered at 1.5 keV. A 5.5 μm-thick Al (K absorption edge at 1.56 keV) and 25 μm-thick Be foils were put in the front of the X-ray streak camera for X-ray filtering.

The magnetic field lines move together with the ablated plasma due to its large Re_m. The direction of the ablated plasma flow is normal to the target surface, and ablated plasma accumulates at the valley of the sinusoidal perturbation. Therefore, the external magnetic field is compressed (decompressed) at the valley (peak) of the sinusoidal perturbation (Figs. 3.5 (c)). The thermal conductivity across the magnetic field lines is reduced at the valley compared to that at the peak. The temperature increases at the valley due to the anisotropic thermal conduction in the perturbed magnetic field structure as shown in Figs. 3.5 (a) and (b). The pressure distribution becomes spatially non-uniform, and lead to enhancement of the perturbation growth.

The PINOCO-MHD code was used to reproduce the temporal evolution of the experimentally observed perturbation growth. In our previous studies[14], growth of a 50-μm perturbation was found to be significantly slow compared to the simulation and theoretical predictions. Similar results were obtained also in the other facilities' experiment[15]. We artificially reduced the laser intensity by $\times$ 0.25 to fit the computed growth to the experimental ones for the case of no external magnetic field, and the same reduction factor was used to compute the perturbation growth for the $B_{\parallel}$ geometry. The spatial and temporal resolutions of the imaging system were 13 μm and 150 ps, respectively. The modulation transfer function (MTF) of the imaging system was measured in separate shots, and the MTF was used to obtain the actual amplitude of the areal density modulations from the

[14] Sakaiya et al. 2002; Azechi et al. 2007.
[15] Glendinning et al. 1997; Smalyuk et al. 2008.

measured one as shown in Fig. 3.6 (a). The PINOCO-MHD code reproduces the experimental trend with the reduced laser intensity, as shown in Fig. 3.6 (b).

Hydrodynamic instability growth is reduced by restitution force of the magnetic field bent by non-uniform plasma flow in a low-β plasma and external magnetic field having the critical strength[16]. In our high-β plasma, restitution force of the magnetic field is negligibly small to hydrodynamics instability growth. And also, an ablated plasma flow across the fluid boundary plays essential roles in the ablative hydrodynamic instability. The previous analysis, in which the ablation effects are neglected, can not be directly applied to our result.

Instability growth in the $B_\perp$ geometry is also simulated for a reference. An ablated plasma flow carries away the external magnetic field from the laser absorption region, therefore, the hydrodynamics growth is not affected by the $B_\perp$ magnetic field in this simulation.

We have demonstrated experimentally that a 200-300 T external magnetic field noticeably affects the hydrodynamics and instability growth of a HEDP, even for high-β plasmas. This experimental result suggests that the magnetic field seeds non-spherical symmetrical structures in a HEDP by anisotropic thermal conduction. These effects must be considered in the design of magnetically-assisted inertial confinement fusion, which may be an alternative to fusion ignition schemes. Srinivasan *et al.,* have pointed out that strengths of the self-generated magnetic field and the Hall parameter are estimated to be in the order of 10^2 - 10^3 Tesla and in the range between 0.1 and 1, respectively, in National Ignition

[16] Stone and Gardiner 2007; Sano, Inoue, and Nishihara 2013.

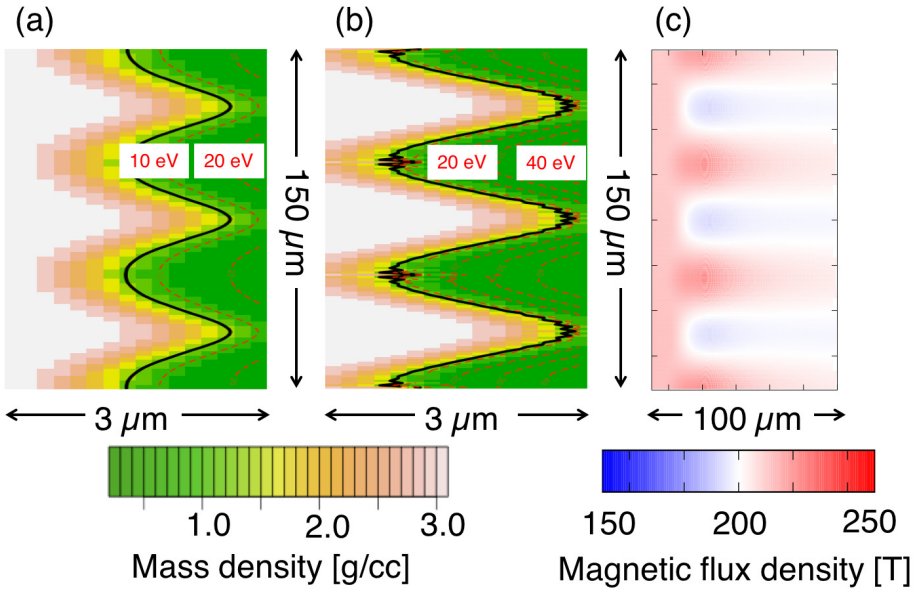

Figure 3.5: Snapshot of 50-μm wavelength perturbations on a laser-accelerated polystyrene foil simulated using the PINOCO-MHD code for (a) no external magnetic field and the (b) $B_{||}$ geometry. The solid black lines are lines of equal density for the target solid density of 1 g/cm^3, and the dashed red lines are isotherms of the electron temperature plotted in 10-eV increments. The anisotropic thermal conduction in the perturbed magnetic field structure (c) leads to enhancement of the perturbation growth.

Facility implosion[17]. In such strong self-generated magnetic field, anisotropic thermal conduction may affect hydrodynamic instability growth and thermal energy transports during hot spot generation. The reported experimental platform is a unique testbed for studying MHD phenomena in laboratory astrophysics and the laser fusion research. The anisotropic thermal transport is still a hypothesis to explain a part of our experimental results based on the simulation. In the future

[17] Srinivasan and Tang 2012.

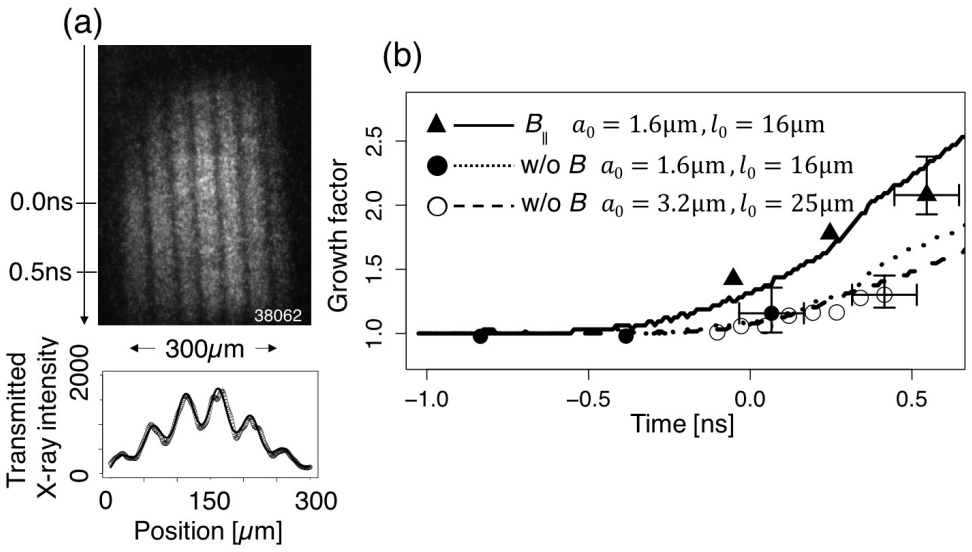

Figure 3.6: (a) A face-on X-ray backlight image and its line-out at the laser peak timing. The origin of the axis is defined as the laser peak timing. (b) Comparison of temporal evolution of areal density modulations measured in the experiment and calculated by the PINOCO-MHD code.

work, it is necessary to measure directly temperature and density of ablating plasmas in the external magnetic field to verify more details of the simulation code.

3.5 Measurements of temporal evolution of implosion core in a strong magnetic field

As explained in Chapter1, a shell target has been used to generate an implosion core from the beginning of the FI experiment. The role of the shell target is adapted to generate hot spots at moderate laser intensity.

Fig.3.7 shows asymmetric implosion of a shell implosion under an external magnetic field[18]. This simulation was calculated by the PINOCO-MHD code, in which magnetic field effects are considered. A 250-μm diameter solid spherical deuterated polystyrene (CD) target is imploded uniformly by 0.53 μm-wavelength and Gaussian laser pulse (1.3 ns of full width at half maximum and 1.8 kJ with 9 beams). A 7-μm thick gold cone is attached to the CD target for the fast-ignition laser fusion. A capacitor coil target with 1000 μm diameter is located 1000 μm from the centre of the shell. The shell is initially exposed to a 20–60 T magnetic field. This simulation was performed to optimize magnetic field structure for guiding of a diverged relativistic electron beam to a fuel core by the external magnetic field for increasing heating efficiency of the fast-ignition scheme. Although initial fluxes of the magnetic field is perpendicular in this figure, the magnetic fluxes are bent associated with ablation and implosion of the plasma due to diamagnesim feature of the imploding plasma. Under the external magnetic field, the core is compressed strongly in the direction of across the magnetic lines of flux. Electron thermal conduction across the magnetic field lines is reduced because

[18] Nagatomo, T. Johzaki, T. Asahina, et al. 2015.

Lamor radius of thermal electrons is much smaller than temperature scale length of the plasma. Plasma temperature and pressure increases owing to reduction of the thermal conductivity. This simulation indicates that a shell implosion under an external magnetic field leads to asymmetric implosion by the anisotropic thermal conduction.

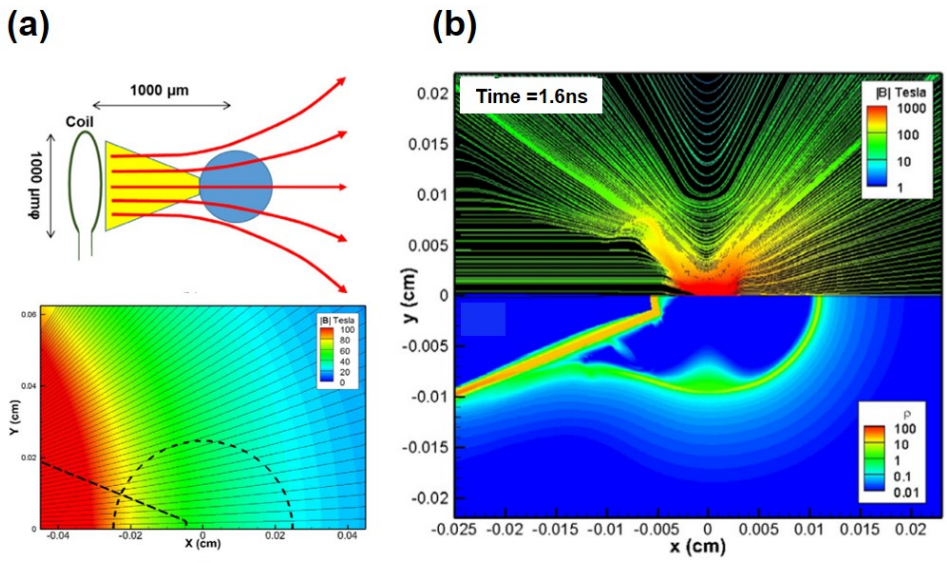

Figure 3.7: (a) Initial conditions of simulation.(b) A snapshots of magnetic field lines and mass density at acceleration phase. The figure is taken from Nagatomo, T. Johzaki, T. Asahina, et al. 2015.

In FI scheme, the hot spot does not generate during the compression process but generated by the heating. This means that using a shell target is not necessary. Here a solid target is suggested for a new target for FI. The shell target is directly accelerated by the ablation pressure. While the solid target is not accelerated but shock waves are driven inside the target. The solid target is only compressed by the shock waves. A shock wave is a well-known self-stabilizing hydrodynamic

phenomenon. Even it has an initial perturbation on the shock surface, those are smoothed by the ion-acoustic waves at the post-shocked region[19]. Solid targets can be expected to be more resistant to hydrodynamic instability than shell targets.

We measured the time evolution of an directly driven CD solid ball target to investigate the strength against hydrodynamic instability in a magnetic field. Fig.3.8 shows the experimental setup. Nine of GEKKO-XII laser beams were used for compression of a solid ball target. Wavelength, pulse shape, pulse duration, and energy of the GEKKO-XII beams used for implosion were 0.526 μm, Gaussian, 1.3 ns (FWHM), and 240 $\pm$ 15 J per beam. The target was made of a 200 μm-diameter CD solid ball. Three of GEKKO-XII laser beams were used for generating magnetic field. Wavelength, pulse shape, pulse duration, and energy of the GEKKO-XII beams used for magnetic field generation were 1.053 μm, Gaussian, 1.3 ns full-width at half-maximum (FWHM), and 600 $\pm$ 20 J per beam. From previous study[20], the strength of magnetic field can be estimated 100 T at the center of the CD solid ball target by the current GEKKO-XII laser beams configuration.

X-ray backlight images of the compressed core were recorded with a combination of 4.51 keV Ti$-K_\alpha$ produced by the 1.6 ps, 1 kJ LFEX laser, and a spherically bent crystal x-ray imager[21] . The magnification, spatial resolution, and spectral bandwidth were 10, 15 μm (FWHM), and 5 eV (FWHM), respectively. The time evolution of the core images was obtained by changing the delay between the GEKKO-XII and LFEX laser. The x-rays generated by the LFEX laser were

[19] CHESTER 1954.
[20] Law et al. 2016; Fujioka, Z. Zhang, et al. 2013.
[21] Fujioka, Fujiwara, et al. 2010; Sawada, Lee, et al. 2016.

attenuated by the compressed plasma and x-ray shadow of the compressed plasma was imaged by using a spherical bent crystal on an imaging plates(IP). Fig.3.9(a) shows x-ray shadow of the compressed core in previous experiment. Noise from direct X-ray radiation from the target is detected on the right side of the image, and the noise of electrons is detected throughout the image. Noise of the x-ray was removed by placing a shield of lead (Pb), and noise of the electrons was removed by placing a magnet in front of the IP, as shown in Fig.3.9(b). An x-ray shadowgraph is converted to an x-ray transmittance profile by interpolating the two-dimensional backlight x-ray intensity profile from the outside peripheral of the dense plasma shadow.

Fig.3.10 shows comparison of transmittance profile in nodriven case. The spatial resolution and noise of the measurement system were added to the simulation result and compared with the experimental result. The transmittance at the center position of a solid ball target without laser irradiation was reproduced by simulation. Fig.3.11 shows a comparison of the transmittance with and without the magnetic field. The transmittance of with magnetic field 70 ps after laser peak time is lower than without magnetic field 140 ps after laser peak time in the simulation. This trend is same in the experiment. Fig.3.12 shows the time evolution of the core in the magnetic field. The implosion core reaches maximum compression about 200 ps after the peak of the implosion laser and then expands. The experimental maximum compression time agrees with the simulation. When using a solid ball target, asymmetric implosion does not occur in experiments and simulations. Solid ball targets are suitable for compression in the magnetic field.

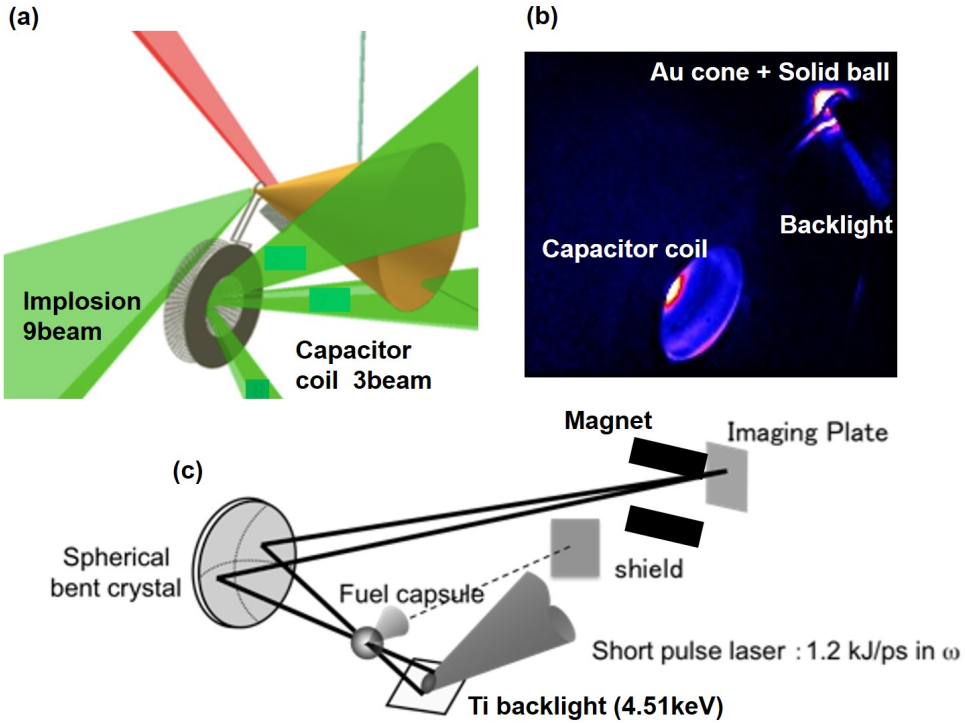

Figure 3.8: (a) Geometry of $\mathrm{Ti}-K_\alpha$ radiography experiment. (b) Self-emission x-rays from implosion core and capacitor coil target were recorded by x-ray pinhole camera. (c) X-ray backlight images of the compressed core were recorded with a combination of 4.51 keV Ti K-alpha produced by LFEX laser and a spherically bent crystal imager.

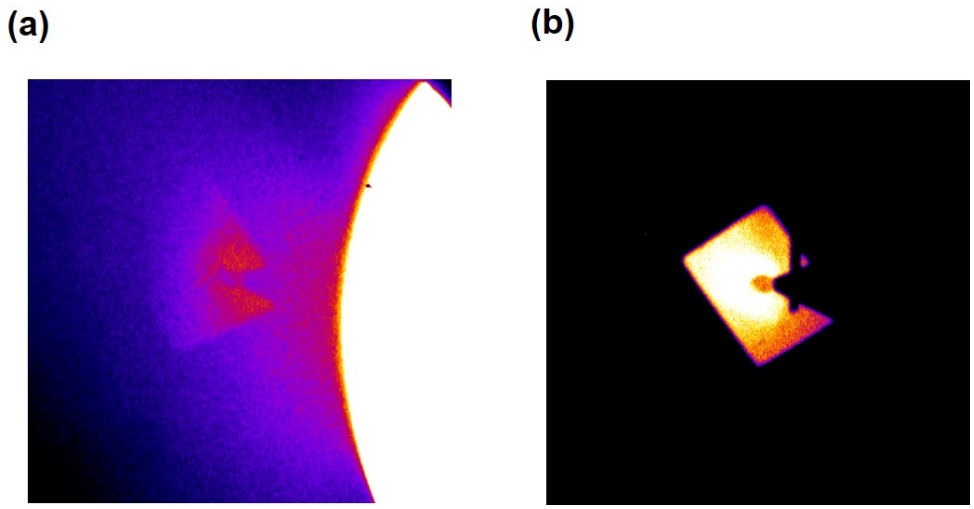

Figure 3.9: (a) Previous image of $\mathrm{Ti}-K_\alpha$ radiography. (b) Current image of $\mathrm{Ti}-K_\alpha$ radiography.

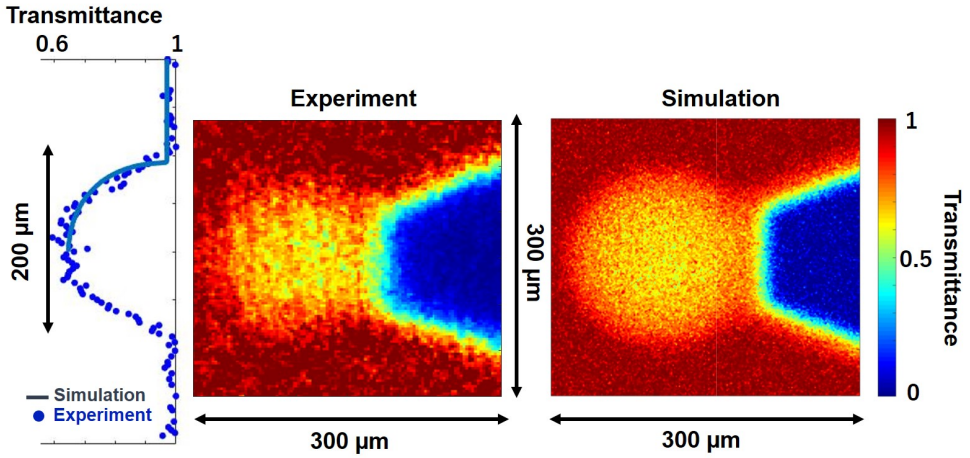

Figure 3.10: Comparison of transmittance (nodriven). The spatial resolution(=15μm) and noise of the measurement system were added to the simulation result and compared with the experimental result. The transmittance at the center position of a solid ball target without laser irradiation was reproduced by simulation.

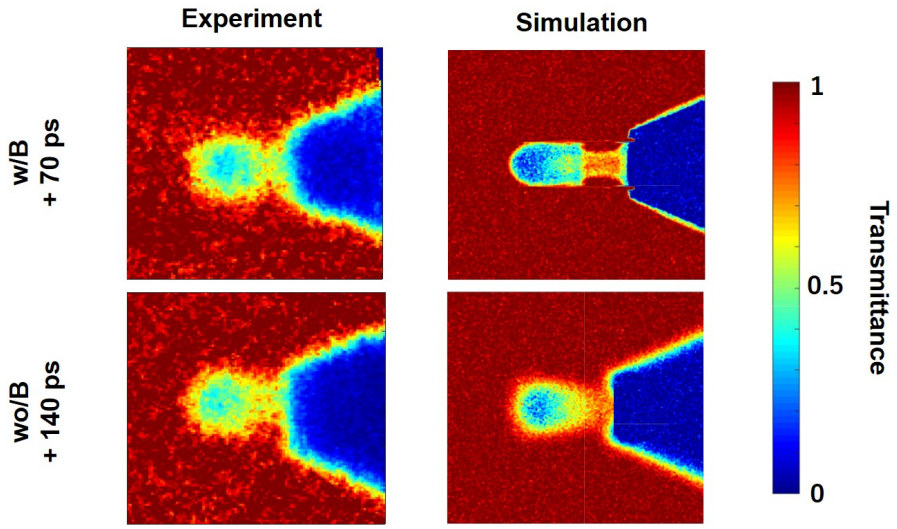

Figure 3.11: The transmittance of with magnetic field 70 ps after laser peak time is lower than without magnetic field 140 ps after laser peak time in the simulation. This trend is same in the experiment.

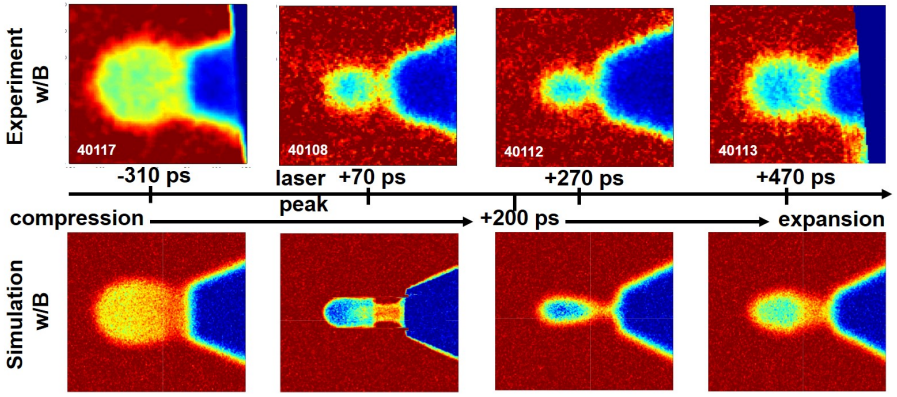

Figure 3.12: Measurements of temporal evolution of implosion core in the strong magnetic field. In this experiment, the time of + 270 ps is estimated to be around the maximum compression time. And the time of + 200 ps is the maximum compression time in the simulation. Experimental trend is similar to the simulation. But size of the implosion core is about larger than the value predicted by simulation.

4. Efficient heating by thermal transport from the laser heated hot region to the cold dense region

4.1 Introduction

Power laser apparatus can inject a plenty of energy to a matter in a small volume within a short time duration. The matter becomes a high-energy-density state that is applicable to various scientific researches such as laboratory astrophysics[1] and several kind of radiation sources: X-rays, charged particles, and neutrons[2]. Fast isochoric heating of a solid target have been studied to create high-energy-density states by using short pulse laser[3] and X-ray free electron laser[4]. The fast isochoric laser heating of a compressed dense plasma core is one of the scheme to create

[1] Remington, Drake, and Ryutov 2006.
[2] Fujioka, Takabe, et al. 2009; Casey et al. 2017.
[3] Sawada, Sentoku, et al. 2019.
[4] Vinko et al. 2015; Royle et al. 2017.

ultra-high-energy-density (UHED) state, which is equivalent to the state at the center of the sun, for the inertial confinement fusion (ICF) science.

In conventional implosion, kinetic energy of an imploded shell is converted to the internal energy of the compressed matter at the maximum compression timing. A UHED state with 36 Peta-Pascal (PPa) was achieved on the National Ignition Facility with 1.8 MJ of laser energy by the indirect X-ray driven implosion[5]. The OMEGA laser facility with 30 kJ of laser energy produced 5.6 PPa of UHED by the direct laser-driven implosion[6]. The significant growth of hydrodynamic instabilities during the compression causes the hot spark mixing with the cold dense fuel and prevents efficient creation of UHED state. The current central ignition scheme requires enormous laser energy to create a UHED state.

In the context of ICF, the fast isochoric heating also known as the fast ignition had been proposed as an alternative approach to the ICF ignition[7]. This approach separates compression and heating processes to avoid the mixing, using a more stable compression followed by an external energy injection, whose time scale is much shorter than the implosion time scale. Significant progresses have been made on the fast isochoric heating to increase the laser-to-core energy coupling[8]. Those improvements mainly focus on increasing laser-to-core energy coupling by drag heating which is the energy exchange through binary collisions between relativistic electrons (REs) and bulk electrons of the plasma.

[5] Le Pape et al. 2018.
[6] Regan et al. 2016.
[7] Tabak et al. 1994.
[8] R.Kodama 2001; Theobald et al. 2014; Jarrott et al. 2016.

There are three major mechanisms of the fast isochoric heating. The following equation describes temporal increment of electron temperature T_e of a dense bulk plasma, whose electron number density is n_e, heated by relativistic electrons (REs)[9].

$$\frac{3}{2}n_e\frac{\partial T_e}{\partial t} = \frac{3}{2}\frac{n_h T_h}{\tau_e(T_h)} + \frac{{j_h}^2}{\sigma(T_e)} + \frac{\partial}{\partial x}(\kappa(T_e)\frac{\partial T_e}{\partial x}). \tag{4.1}$$

Here $\tau_e(T_h)$ is the collision time between bulk electrons and REs having T_h of temperature in a fully ionized plasma. In the calculation of $\tau_e(T_h)$ the bulk electrons' temperature T_e ($\ll T_h$) is neglected. RE current is given as $j_h \simeq en_h c$ with hot electron number density n_h, elementally charge e and speed of light c. Electric conductivity σ of a plasma is $\sigma = n_c e^2\tau/m_e$, where n_c, τ, and m_e are the critical density, collision time scale of cold bulk electrons, and the electron mass, respectively. $\kappa(T_e)$ is bulk electrons' thermal conductivity.

The first mechanism is the heating by REs, which is often called drag heating. This mechanism contributes significantly to heating the over-solid density plasma when the energy of REs is optimized for them to be stopped in the plasma. The REs' large divergence is a critical issue in the drag heating. We had reported enhancement of the laser-to-matter energy coupling with the magnetized fast isochoric heating scheme[10]. The maximum coupling efficiency via the drag heating reached 7.7 $\pm$ 1.2% because of reduction of RE's divergence by the application of the external magnetic field.

The second term represents the resistive heating. The RE current drives a return

[9] Kemp et al. 2006.
[10] Sakata et al. 2018.

current j_e, whose flow direction is opposite to that of the RE current, to maintain current neutrality in the plasma, i.e. $j_e \simeq j_h$. Since the return current is more collisional than the RE current, the return current heats the plasma ohmically. The resistive heating is the dominant heating mechanism when the current density is high since $\propto j_h^2$. However, it becomes less effective when REs propagate with large divergence. The resistive heating is the dominant heating mechanism in the laser-plasma interaction region.

The third mechanism is the diffusive heating, in which thermal electrons transport their energy diffusively from the laser heated hot region to the cold dense region. The diffusive heating has been identified as one of the dominant mechanisms for laser isochoric heating for the first time in Ref. [11]. A high ionization state in a solid was produced by thermal diffusion in a few picoseconds even after the pulse terminates. By extending the pulse duration, the laser supplies its energy continuously to the hot plasma while the thermal diffusion takes place. The diffusive heating becomes more important to heat the dense core (> 10 g/cm^3) beyond keV by multi-picosecond heating laser pulse duration.

In this study, we have created 2.2 PPa of UHED efficiently using a mulit-picosecond petawatt laser, LFEX, with the total 4.6 kJ energy (1.5kJ is for compression, 1.7kJ is for generating a magnetic field, and 1.4kJ is for heating laser) in the magnetized fast isochoric heating scheme. The achievement of the UHED with the fast isochoric heating can not be explained only with the enhanced drag heating. Two-dimensional particle-in-cell (2D-PIC) simulation reveals that the diffusive

[11] Sawada, Sentoku, et al. 2019.

heating mechanism contributed significantly to the keV heating of an imploded plasma in a time scale of a few picoseconds.

This achievement was realized with the following improvements, as shown in Fig.4.1. The first improvement is the heating laser contrast. A short pulse laser system emits inevitably weak pulses preceding the main pulse. The intensity ratio of the main pulse to the preceding pulses is called the pulse contrast. A low contrast laser system produces a long-scale-length plasma in the laser-plasma interaction zone before the main pulse arrival time. The preformed plasma affects negatively on the dense plasma heating because of separation of the interaction zone away from the dense plasma. The high contrast laser enables easy access to high density plasma.

The second is implementation of a solid ball target. The solid ball compression does not generate shocks and rarefactions traveling ahead of the shock-compressed matter, therefore a cone tip is not required for preventing a hot plasma flowing into the cone. The direct interaction of a dense matter with heating laser pulse is then realized with the open-tip cone, resulting enhancement of the diffusive heating from the interaction zone to the imploded dense plasma.

The third is a laser-driven capacitor coil target used for generating strong magnetic field. By applying external magnetic fields to the path of the REs and the thermalized electrons, which carry the heat, the divergence issue can be resolved so that the resistive heating near the interaction zone works efficiently to make a large temperature gradient for the diffusive heating.

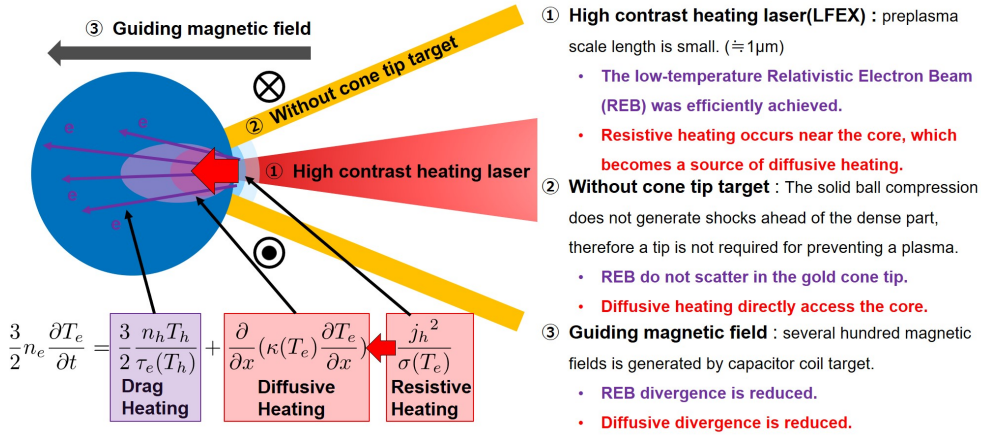

Figure 4.1: Improvements for efficient creation of UHED state

4.2 Experimantally estimation of hot-spot pressure

Figure 4.2 shows an experimental layout. Three of GEKKO-XII laser beams were used for generating magnetic field to guide REs and enhance drag heating efficiency. Wavelength, pulse shape, pulse duration, and energy of the GEKKO-XII beams used for magnetic field generation were 1.053 μm, Gaussian, 1.3 ns full-width at half-maximum (FWHM), and 600 $\pm$ 20 J per beam. The strength of magnetic field generated with the capacitor-coil target had been measured on GEKKO-XII, LULI2000, Shengguang-II, and OMEGA-EP laser facilities[12]. 600 - 700 Tesla of magnetic fields were obtained by the current GEKKO-XII laser beams configuration. By applying external magnetic fields to the path of the REs and the

[12] Law et al. 2016; Fujioka, Z. Zhang, et al. 2013; Zhu et al. 2015; Santos et al. 2015; Gao et al. 2016.

thermalized electrons, which carry the heat, the divergence issue can be resolved[13] so that the resistive heating near the interaction zone works efficiently to make a large temperature gradient for the diffusive heating.

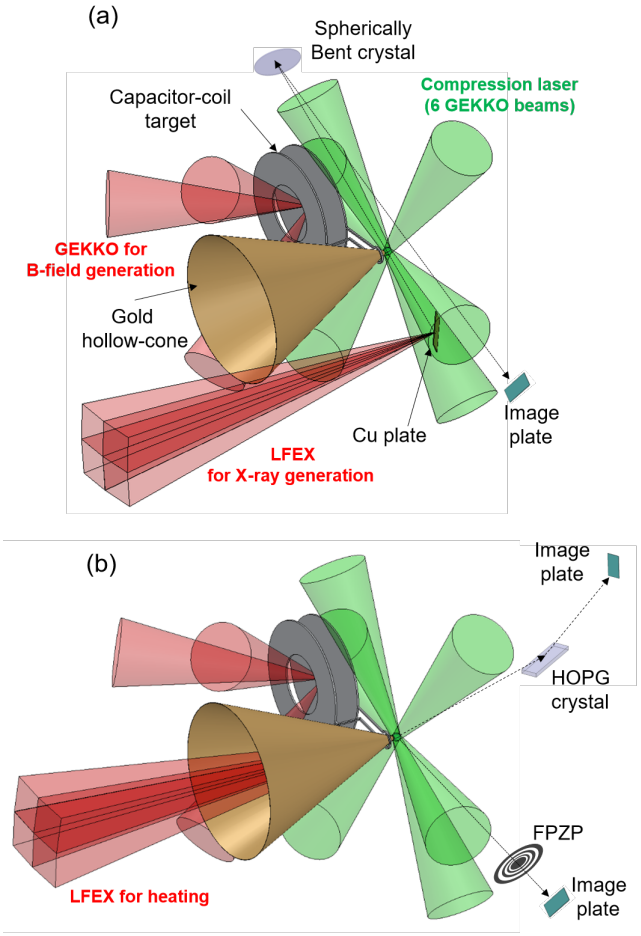

Figure 4.2: (a) Two-dimensional density profiles of compressed Cu(II) oleate solid balls were measured with flash X-ray backlight technique coupled with a spherically bent crystal X-ray imager. (b) The X-ray spectrometer was installed at 40 deg from the LFEX incident axis to estimate the electron temperature and the Fresnel Phase Zone Plate(FPZP) was installed at 90 deg from the LFEX incident axis to identify the heating region.

[13] Bailly-Grandvaux et al. 2018.

Table 4.1 summarizes the results in the experiment. The experiment had been conducted on GEKKO-LFEX laser facility at Institute of Laser Engineering, Osaka University. The experimental time origin (t_{exp} = 0 ns) is defined hereafter as the peak of the compression laser pulse.

Case	Heating Energy [J]	Heating Timing [ns]	Electron Temperature [keV]	Mass Density [g/cm^3]	Pressure [PPa]
A	1516	0.40	2.1 $\pm$ 0.2	1.1 (+6.1 / -0.0)	0.2 (+1.4 / -0.0)
B	1016	0.61	2.0 $\pm$ 0.1	11.3 (+5.9 / -2.2)	2.2 (+1.3 / -0.5)
C	1100	0.38	1.9 $\pm$ 0.2	1.1 (+6.1 / -0.0)	0.2 (+1.4 / -0.0)
D	668	0.37	1.5 $\pm$ 0.1	1.1 (+6.1 / -0.0)	0.2 (+1.4 / -0.0)
E	625	0.72	N/A	11.3 (+5.9 / -2.2)	N/A

Table 4.1: Summary of the results in Fast Isochoric Heating experiment.

Six of GEKKO-XII laser beams were used for compression of a solid ball target. Wavelength, pulse shape, pulse duration, and energy of the GEKKO-XII beams used for implosion were 0.526 μm, Gaussian, 1.3 ns (FWHM), and 240 $\pm$ 15 J per beam. The target was made of a 200 μm-diameter Cu(II) oleate solid ball [$Cu(C_{17}H_{33}COO)_2$][14] coated with a 25 μm-thick polyvinyl alcohol (PVA) layer to prevent the Cu atoms from directly laser irradiation. The Cu(II) oleate solid ball contains 9.7% Cu atoms in weight. X-ray emissions from Cu atoms were used for characterizing the coupling efficiency and the electron temperature. A open-tip gold cone was attached to the Cu(II) oleate solid ball. The solid ball compression does not generate shocks and rarefactions traveling ahead of the shock-compressed matter, therefore a cone tip is not required for preventing a hot plasma flowing into the cone[15]. The direct interaction of a dense matter with heating laser pulse is then

[14] Iwasa et al. 2017.
[15] Fujioka, Tomoyuki Johzaki, et al. 2015.

realized with the open-tip cone, resulting enhancement of the diffusive heating from the interaction zone to the imploded dense plasma.

Two-dimensional density profiles of compressed Cu(II) oleate solid balls were measured with flash X-ray backlight technique coupled with a spherically bent crystal X-ray imager[16] as shown in Fig. 4.3. The magnification, spatial resolution, and spectral bandwidth were 20, 13 μm (FWHM), and 5 eV (FWHM), respectively. The X-rays generated by the LFEX laser were attenuated by the compressed plasma and x-ray shadow of the compressed plasma was imaged by using a spherical bent crystal on an imaging plates. An X-ray shadowgraph is converted to an X-ray transmittance profile by interpolating the two-dimensional backlight X-ray intensity profile from the outside peripheral of the dense plasma shadow. Areal density of the compressed plasma was calculated from the X-ray transmittance profile with an opacity of 100 eV Cu(II) oleate for 8.05-keV photon. A two-dimensional density profile of the compressed plasma was then obtained after applying an inverse Abel transformation to the areal density profile, assuming rotational symmetry of the core along the cone axis. The converging shock waves were still traveling to the center of the solid ball at t_{exp} = 0.38 ns, therefore the area close to the cone maintained the initial density 1.1 g/cm^3. Maximum compression was reached at around t_{exp} = 0.72 ns. The average mass density of the core along the laser axis is 11.3 g/cm^3.

Since the plasma compression progresses with time, we can experimentally test how isochoric heating efficiently changes with density, simply by altering

[16] Fujioka, Fujiwara, et al. 2010; Sawada, Lee, et al. 2016.

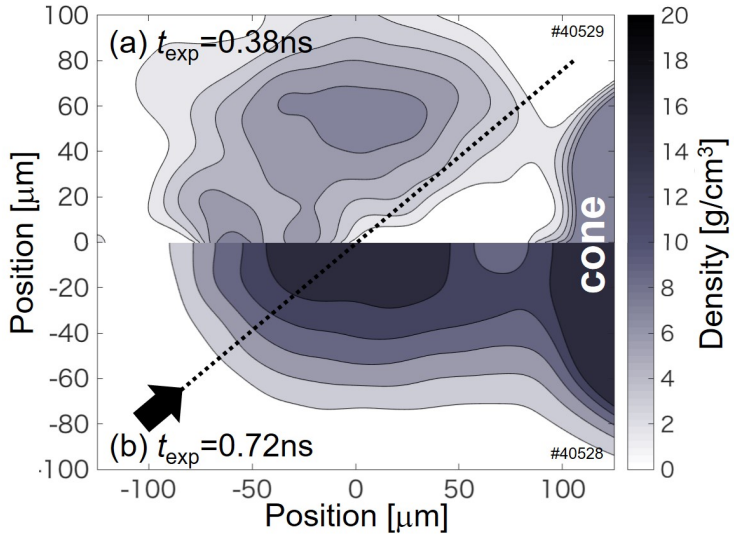

Figure 4.3: Two-dimensional density profiles of compressed Cu (II) oleate solid balls. (a) At t_{exp} = 0.38 ns, the converging shock waves were still traveling to the center. (b) The core reached maximum compression timing at t_{exp} = 0.72 ns. Dotted lines show lighn of sight of the X-ray spectrometer.

the heating laser timing(e.g., t_{exp} = 0.37 or 0.72 ns). Four LFEX beams were injected from the gold cone to heat the compressed plasma isochorically to 1-2 keV. Wavelength, pulse shape, pulse duration, and energy of the LFEX beams were 1.053 μm, Gaussian, 1.8 $\pm$ 0.3 ps (FWHM), and varied from 620 to 1520 J. The focal spot diameter was 50 μm (FWHM) containing 30% of the total energy, yielding an intensity of 1.3×10^{19} W/cm^2 at the maximum energy shot. A short pulse laser system emits inevitably weak pulses preceding the main pulse. The intensity ratio of the main pulse to the preceding pulses is called the pulse contrast. A low contrast laser system produces a long-scale-length plasma in the laser-plasma interaction zone before the main pulse arrival time. The preformed plasma affects

negatively on the dense plasma heating because of separation of the interaction zone away from the dense plasma. The high contrast LFEX laser enables easy access to high density plasma.

The X-ray spectrometer was installed at 40 deg from the LFEX incident axis (dotted lines of Fig. 4.3). The spectrometer utilizes a planar highly oriented pyrolytic graphite (HOPG) as a dispersive element. The spectral resolution of the spectrometer was 17.9 eV (FWHM). Figure 4.4 (a,b,c,d,e) shows X-ray spectra in the range of 8.0 to 8.6 keV. The peaks at 8.05, 8.35, and 8.39 keV are Cu$-K_\alpha$, Li-like Cu satellite lines , and Cu$-He_\alpha$, respectively. The peak at 8.26 keV is Ni-K_β that was emitted from a Ni-made capacitor-coil target. The peak around 8.5 keV are Au-L lines emitted from the Au cone. The ratio of Cu$-He_\alpha$ to Li-like satellite line reflects information on the electon temperature T_e, plasma density ρ and thickness along the line of sight of the spectrometer d.

X-ray spectra from Cu were computed by using FLYCHK code[17]. The Ni-K_β and Au-L lines were measured in separate shots, and these emissions were subtracted from the measured spectra after adjusting their peak intensity to fit the measured one. The thickness was determined so that the spectrum could be reproduced within the density range obtained with the X-ray backlight. The spectra were calculated with varying ρ within the experimentally obtained density and T_e to minimize the differences between the experimental spectral shape and calculated ones.

In Cases A, C and D, where the LFEX is injected before the maximum com-

[17] Chung et al. 2005.

pression timing, the minimum difference was found around 1.0 g/cm^3. The spectra calculated with T_e = 2.1, 1.9, and 1.5 keV, ρ = 1.0 g/cm^3, d = 100 μm well reproduce the shape of the spectrum, as shown in Fig. 4.4 (a), (c), and (d), respectively.

The plasma was compressed further at the later timing (Case B), the spectra calculated with T_e = 2.0 keV, ρ = 12 g/cm^3, d = 30 μm well reproduce the shape of the spectrum, see Fig. 4.4 (b). In Case B, our measurements show that the mass density of the plasma along the laser axis was 11.3 g/cm^3 and a part of the core was heated to 2.0 keV, which correspond to 2.2 PPa of electron pressure. The amount of Li-like Cu satellite lines and Cu-He$_\alpha$ X-ray signal decreases as LFEX laser energy decreases. In case E, where the LFEX energy was minimum among the listed shots, the signal was too weak, therefore, it was impossible to evaluate the temperature by fitting as shown in Fig. 4.4 (e).

The mean square values of differences between measurements and calculations of x-ray spectra, which is normalized with its minimum value, are shown in the assumed density and temperature spaces as Fig. 4.5 (a,b,c,d,e). Figure 4.5 (a), (c), and (d) show those before the maximum compression time which correspond to Case A, C, and D in Table I. In those cases, we can find the minimum least square value around 1.0 g/cm^3. Assuming a smaller thickness and over the initial solid density, the temperature is found to be around 2 keV for Case B in Table I, as shown in Fig. 4.5(b). The amount of Li-like Cu satellite lines and Cu$-He_\alpha$ X-ray signal decreases as LFEX laser energy decreases. In case E, whose energy is minimum in the listed shots, the signal was too weak for our measurement, therefore, it was impossible to evaluate the temperature with sufficient accuracy by fitting, as shown

in Fig. 4.5(e).

To identify the heated region, the heated core was imaged by Fresnel Phase Zone Plate(FPZP). He_α emissions indicating the heated region were observed along the laser axis, so that the experimental result confirms that the heating region exists in the above-solid-density region. Details of the FPZP observations are described in appendixB.

In our previous work, maximum laser-to-core coupling efficiency by the drag heating was 7.7 $\pm$ 1.2 % which corresponds to Case E in Table **??**. It means that 48 $\pm$ 7 J energy can be deposited in the core by the drag heating. Even at the maximum compression timing, the areal mass densities (ρL) of the core along the RE beam path length (L) were $\rho L = 0.16 \mathrm{g/cm^2}$, which is shorter than the RE's mean free areal density (typically ρL = 0.6 g/cm^2 for 1 MeV of REs's slope temperature). Therefore, the entire core was heated uniformly up to $T_e = 80 \pm 10$ eV by the drag heating. Then, the 7.7 $\pm$ 1.2% of coupling efficiency via the enhanced REs heating[18], which is so called drag heating, can not explain the achievement of the UHED. This suggests that the other heating mechanism contributes predominantly to explain the observations.

[18] Sakata et al. 2018.

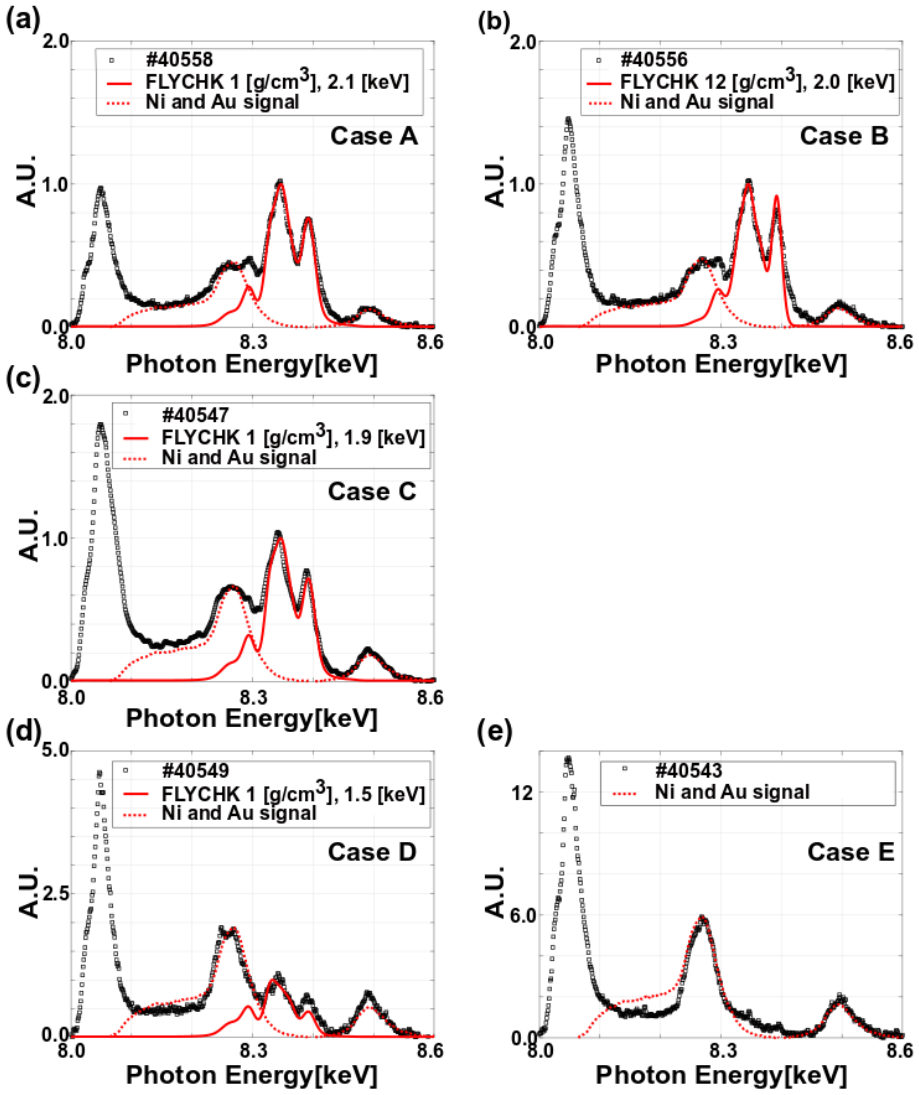

Figure 4.4: X-ray spectra in the range from 8.0 to 8.6 keV. (a), (b), (c), (d), (e) Black square, red line, and red dotted line show the experimental spectra data, the computed spectra data by using FLYCHK code, and the Ni-K_β and Au-L lines subtracted from the measured spectra. The experimental data of Case A, C, and D were well reproduced with the density 1.0 $\mathrm{g/cm^3}$, and the temperature as 2.1 $\pm$ 0.2, 1.9 $\pm$ 0.2, 1.5 $\pm$ 0.1 keV, respectively. The experimental data of Case B were well reproduced with the density 12 $\mathrm{g/cm^3}$ and the temperature 2.0 $\pm$ 0.1 keV.

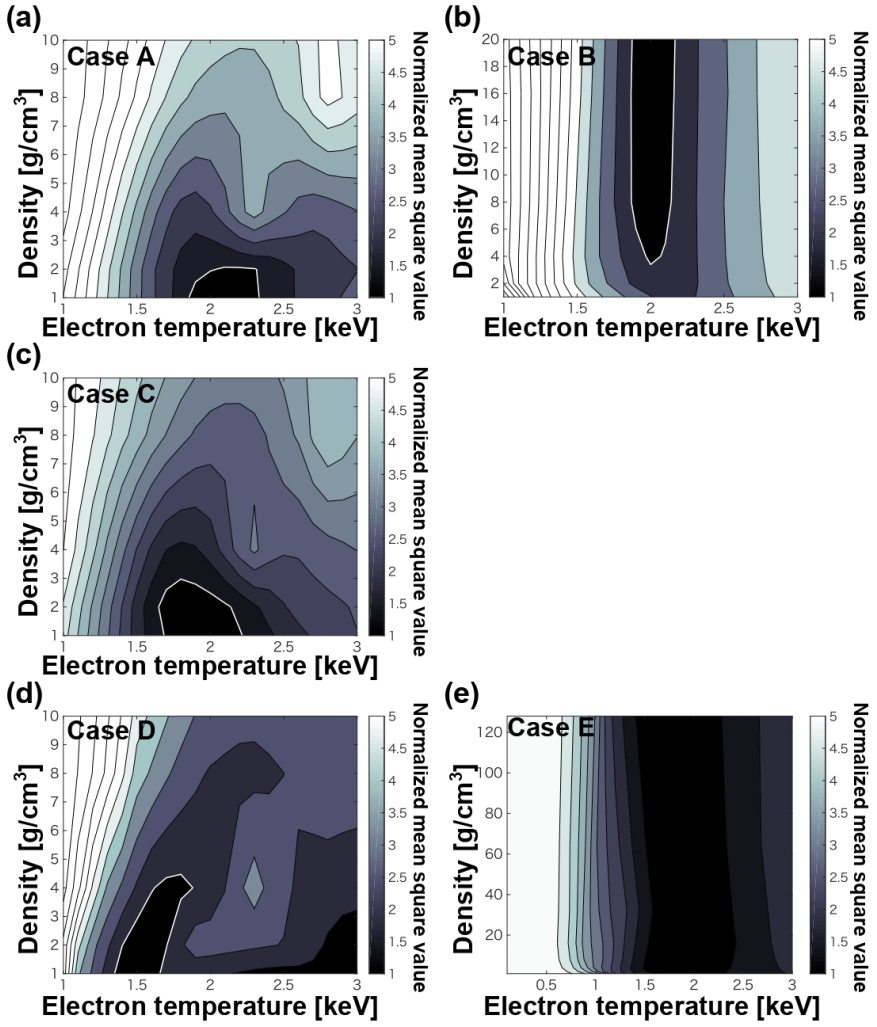

Figure 4.5: (a), (b), (c), (d), (e) The least square value is normalized by using the minimum least square value of each data. We can find the minimum least square value in the region surrounded by white line. The experimental data of Case A, C, and D were well reproduced with the density 1.0 $\mathrm{g/cm^3}$, and the temperature as 2.1 $\pm$ 0.2, 1.9 $\pm$ 0.2, 1.5 $\pm$ 0.1 keV, respectively. The experimental data of Case B were well reproduced with the density 12 $\mathrm{g/cm^3}$ and the temperature 2.0 $\pm$ 0.1 keV.

4.3 Particle-in-cell simulations with experimental conditions

To study the LFEX heating of imploded plasmas, we performed 2 dimensional Particle-in-cell(PIC) simulations under an external magnetic field using the density distribution obtained in the experiment. Simulation results in 2D geometry are obtained using a fully relativistic PIC code PICLS, which features binary collisions among charged particles and dynamic ionization[19]. The size of simulation box is 150 μm in the laser propagation direction and 228 μm in the transverse direction with the mesh size of $1/35\,\mu$m. The origin of X is set to the center of the core as same as experimental data Fig. 4.3. To avoid the numerical heating, the fourth-order interpolation scheme is applied. Absorbing boundary conditions are used for particles in the transverse direction (i.e., no electron reflux is imposed to represent the actual large transverse size of the target). The laser pulse profile and the wavelength are similar as those of the LFEX laser, which has wavelength, pulse shape, pulse duration, and peak intensity of the heating beams of 1.053 μm, Gaussian, 1.2 ps (FWHM), and 1.6×10^{19} W/cm^2. The plasma density profiles are set by the measured plasma density shown in Fig. 4.3 (a) for a case before the maximum compression (shown below as Fig. 4.6) and (b) for the maximum density compression (shown in Fig. 4.7). The target consists a neutral plasma of electrons and C^{3+}, containing 5% Cu^{3+} ions in weight. The number of particles per cell is 32 (29 for electrons and 3 for ions) and the total number of particles

[19] Sentoku and Kemp 2008.

used in the simulation is about 1.4 billion. A uniform external magnetic field with 1 kT along X-axis is applied as in the experiment. The energy density is converted to the pressure in unit [PPa].

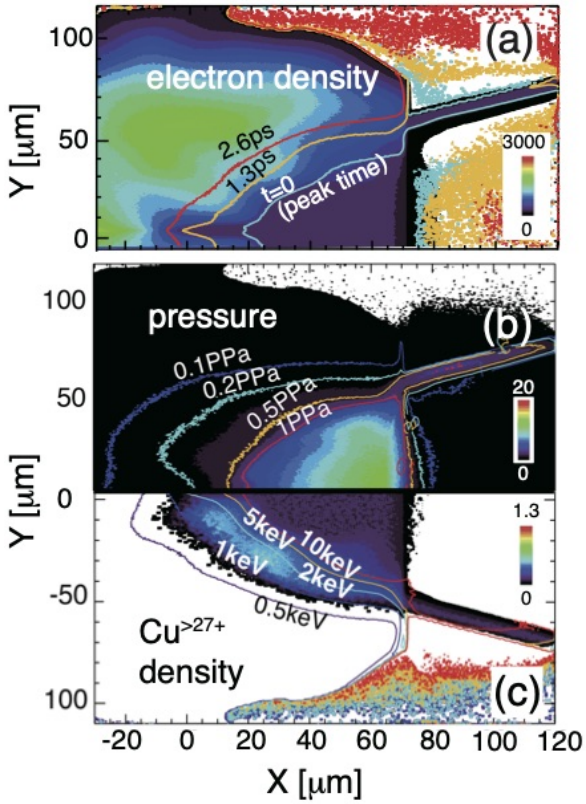

Figure 4.6: PIC simulation before the maximum compression ($t_{exp} = 0.38$ ns): (a) The propagation of heat wave indicated by 1 keV contour lines on the density profile. (b) Pressure distributions with the contour lines (PPa). (c) Electron temperature distribution on the density distribution of the doped copper with charge state $Z \geq 27$, which indicates where the He_α emissions come from. (b) and (c) are plotted at $t = 2.6$ ps after the heating laser peak time.

Figure 4.7 (a) shows time evolution of heated region indicated with contour lines of 1 keV from the heating laser peak time ($t = 0$) for the cases with the density

profile at the maximum compression timing ($t_{\rm exp}$ =0.72 ns) in Fig. 4.3. The heating laser is irradiated from the right side through the cone and it heats directly the front edge of the dense plasma core owing to the high contrast laser light. The electron temperature evolves temporally via the thermal heat transport to the core by the diffusive heating. The heat wave propagates with velocity $> 10\,\mu$m/ps even after the heating laser irradiation terminated, and then the core region ($X < 40\mu$m) was heated over 1 keV electron temperature at $t = 4.8$ ps, see Fig. 4.7 (a) and (c).

Fig. 4.7 (b) shows the two dimensional pressure distribution at t=4.8 ps. The pressure of the core region ($X < 40\mu$m) starts from 2 PPa at the front edge to 0.5 PPa at the other side ($X \simeq -10\,\mu$m). Fig. 4.7 (c) show the bulk electron temperature on the density distribution of the doped copper having the charge states $Z \geq 27$. The doped copper densities with $Z \geq 27$ indicate that where Cu$-He_\alpha$ photons are coming from. We see that the doped copper ions inside the core region get $Z \geq 27$, namely, the large amount of He_α emissions are expected from the core. The core region at the maximum compression is heated to 1-2 keV, which is consistent with the experimental observation. The electron phase plots of the longitudinal momentum are shown in Fig. 4.7(d) and (e). The diffusive feature is seen from the heating surface ($X \sim 70\,\mu$m). Note here that the phase plot is symmetric vertically in p_x space and also the phase plot of transverse momentum (p_y) has the identical distribution, namely, the electrons are thermalized in the momentum space in this energy range, < 10 keV. These PIC simulation reveals that the diffusive heating is the heating process which can locally heat up the front region to the core region over peta-pascal pressure.

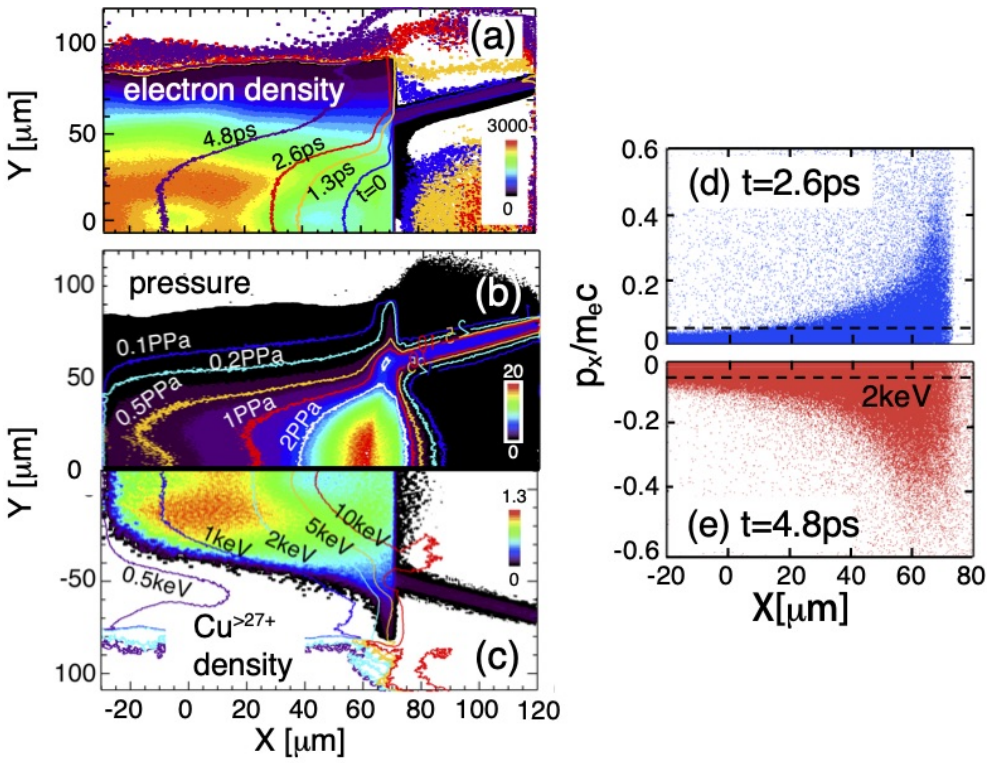

Figure 4.7: PIC simulation at the maximum compression($t_{\exp}$ =0.72 ns): (a) The propagation of heat wave indicated by 1 keV contour lines on the electron density [n_c]. (b) Pressure distributions with the contour lines [PPa]. (c) Electron temperature distribution on the doped copper density [n_c] with charge state $Z \geq 27$, which indicates where the He_α emissions come from. The contours are plotted at $t = 4.8$ ps after the heating laser peak time. The electron phase $X - p_x/m_e c$ at 2.6 ps (d) and 4.8 ps (e), lower-half. The phase plot is vertically symmetric, so that only the upper and lower half are shown due to the space limitation.

4.4 Model of diffusive heating for ignition design

Since the current core density is still low $\sim 10\,\mathrm{g/cm^3}$, still two orders of magnitude less than from the ignition core, the RE drag heating does not play a significant role. While we find that the diffusive heating driven by the direct heating at the interaction surface by the heating laser is a key for creation of keV UHED plasma in the time scale of picoseconds. Here, we revisit a simple one-dimensional model of diffusive heating. In the diffusive process, a heat flux is proportional to the temperature gradient as

$$q = -\kappa \nabla T_e \approx \kappa \frac{T_b}{L}, \tag{4.2}$$

where T_b is the bulk electron temperature near the solid surface, L is the scale length of the temperature gradient. The heat conductivity coefficient κ is assumed as $\kappa = n_\mathrm{e} v_\mathrm{th} l_\mathrm{mfp} = \kappa_\mathrm{SH} \times 3\pi/128$[20], where n_e is the bulk electron density, v_th is the thermal velocity of T_b, l_mfp is the mean free path for T_b and n_e. κ_SH is the thermal conductivity in Spitzer-Härm regime. We here assume that a part of laser energy flux is converted to the heat flux by the surface direct heating;

$$\eta I = n_\mathrm{e} T_b v_\mathrm{heat}, \tag{4.3}$$

where v_heat is the propagation speed of the thermal conduction, and η is the convergence ratio from the laser energy flux (intensity) I to the electron heat

[20] Takashi Asahina et al. 2019.

flux. Hereafter we normalize each variable and express the normalized one with bar, i.e., velocity, density, time, temperature are normalized by the light speed c, critical density of laser light $n_{\rm c}$, laser period $\tau_{\rm L}$, electron rest mass energy $m_{\rm e}c^2$, respectively. Using Eqs.4.2 and 4.3 and assuming that the scale length of diffusion increases as $\bar{L} \approx \bar{v}_{\rm heat}\bar{t}$, the bulk electron temperature near solid surface and the propagation speed of heat wave are derived as

$$\bar{T}_b = \left(\bar{\Gamma} \ln\Lambda \left(\frac{\eta\, a_0^2}{2} \right)^2 \frac{\bar{t}}{\bar{n_{\rm e}}} \right)^{\frac{2}{9}}, \tag{4.4}$$

$$\bar{v}_{\rm heat} = \left(\frac{1}{\bar{\Gamma} \ln\Lambda} \left(\frac{\eta\, a_0^2}{2} \right)^{\frac{5}{2}} \frac{1}{\bar{t}\, \bar{n_{\rm e}}^{\frac{7}{2}}} \right)^{\frac{2}{9}}, \tag{4.5}$$

where $\ln\Lambda$ is the Coulomb's logarithm, $\bar{\Gamma} = \Gamma n_{\rm c} \tau_{\rm L} \left(m_{\rm e}c^2\right)^{-3/2} = 2.65 \times 10^{-8}$. Here, $\Gamma = (4/3)(2\pi)^{1/2} e^4 / m_e^{1/2}$ is a constant of the Coulomb's collision frequency. Both $v_{\rm heat}$ and T_b depend on the plasma density n_e, conversion rate η, and heating time $\bar{t}$, $v_{\rm heat} = 13\,\mu$m/ps and $T_b = 18\,$keV in $5\,$g/cm^3 CH plasma with $\eta = 0.3$, $\ln\Lambda = 5$ at $t = 2\,$ps. Note here that the time dependence is weak as $\bar{T}_b \propto t^{2/9}$ and $\bar{v}_{\rm heat} \propto t^{-2/9}$. Those values are consistent with the simulations, as seen in Fig. 3 (b,d,f). From Eq.4.5, the scale length of heated region is $\bar{L} \approx \bar{v}_{\rm heat}\bar{t}$ proportional to $(t/n_e)^{7/9}$. This suggests that heating lasers with longer duration can heat denser core as a self-similar way.

Fig.4.8 shows the performance of ICF and magnetic confinement fusion (MCF) devices which include our achievement and typical ignition condition. In MCF,

the confinement time τ_E can be easily determined by measuring the decaying time of the plasma energy. Therefore it is common to express ignition conditions as a function of $n\tau_E$ and T. On the other hand, the only measurable parameters of the fuel assembly in ICF are the areal density ρR, ion temperature T, and neutron yield. Therefore it is natural to express ignition conditions as a function of ρR and T, as descrived equation(1.13) in Chapter1. The parameter $P\tau_E$ allow a direct comparison of MCF and ICF for ignition conditions. In ICF the parameter $P\tau_E$ is roughly estimated by using ρR and T[21]:

$$P\tau_E \approx 3.0[(\rho R)T]^{0.8} \tag{4.6}$$

In this study $\rho R = 0.06\,\mathrm{g/cm^3}$ and $T = 2.0\,\mathrm{keV}$, that is, $P\tau_E = 0.55\,\mathrm{atm\,s}$. The typical ignition condition require $P\tau_E \approx 10\,\mathrm{atm\,s}$. According to our model, heating lasers with 10 times longer duration can heat 10 times denser core as a self-similar way which means achivement of $P\tau_E \approx 5.5\,\mathrm{atm\,s}$. The applicability of this model should be discussed in more detail in the future, but this definitely contributes to achivement of the ignition condition.

In the ignition scale experiment, the REB drag heating is also expected to play a significant role. As an example, we here assume that the core is about 10 times denser than the current experiment, i.e., $100\,\mathrm{g/cm^3}$, with the similar diameter $50\,\mu\mathrm{m}$, the heating laser has the same intensity and 10 times longer duration, thus 10 times higher energy than the current experiment, and the coupling efficiency

[21] Betti et al. 2010.

from laser to the core electrons could be much larger than the current experiment 7.7% for $\sim 10\,\mathrm{g/cm^3}$ core. The core temperature is then estimated as $\sim 5\,\mathrm{keV}$ via the REB drag heating. While, the diffusive heating, which is proportional to the ratio of the heating time and the core density, will keep contributing to the heating.

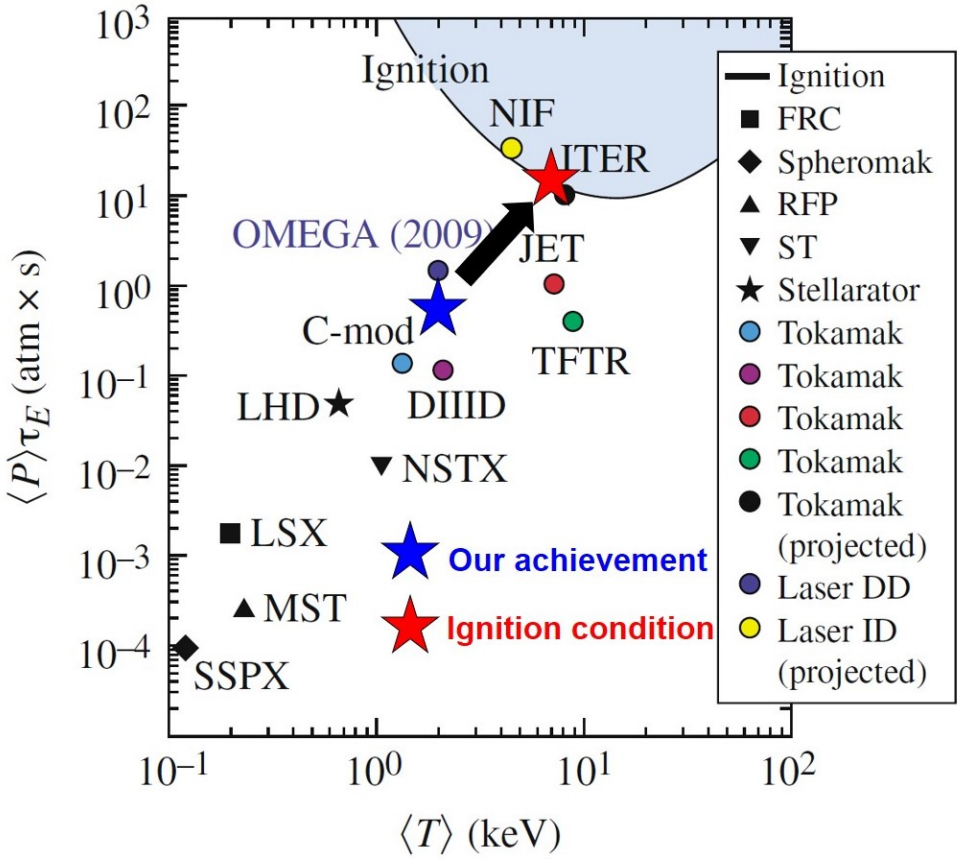

Figure 4.8: Performance of ICF and MCF devices in the $P\tau_E$-T plane. The blue star is our achivement and the red star is typical ignition condition which is our goal. Heating a denser core with a longer duration heating laser can approach ignition conditions.

In summary, we have achieved experimentally 2.2 PPa of UHED state with 4.6 kJ of the total laser energy that is one order of magnitude lower than the energy

used in the conventional implosion scheme. The generation of such the UHED state cannot be explained with the drag heating mechanism only. Particle-in-cell simulations with the experimental conditions confirm that the diffusive heating mechanism plays an essential role[22] to heat the core plasma over keV range on top of the drag heating and resistive heating. Our experimental results clarified that the magnetized fast isochoric heating is an efficient way to create the Peta-Pascal UHED state that is an interesting and unique testbed for various scientific researches, e.g., inertial confinement fusion, intense X-ray, charged particles, and neutron sources, and laboratory astrophysics. We must note that the ultra-high pressure is realized in electron pressure, not in ion pressure. The temperature relaxation time between electron and ion can be estimated as a function of density and temperature after achieving equilibrium temperature[23]. For example, the relaxation time is 13 ps for a CH plasma having $T_e = T_i = 2.0$ keV and $\rho = 10$ g/cm^3. This time is longer than the LFEX laser pulse duration (1.8 ps), therefore ion temperature is lower than the electron one in the current experiment. The relaxation time becomes shorter than heating laser pulse duration in more dense plasma ($\rho > 100$ g/cm^3), then electron energy can be efficiently transferred to ions. For fusion applications, we need ultra-high ion pressure, and thus, further investigations are needed to shorten T_e - T_i equilibration time to deliver ultra-high ion pressure.

[22] Sawada, Sentoku, et al. 2019.
[23] Huba 2013.

5. General conclusion

In this dissertation, experimental demonstration of thermal transport effect in a strong magnetic field for magnetized fast ignition inertial confinement fusion were perfomed. The research is underway on Magnetized Fast Ignition (MFI), which combines a conventional fast ignition method with a strong magnetic field of the order of kilo-tesla to realize fusion ignition. It is predicted that by applying a magnetic field of about 100 T before compression of fusion fuel, heat transfer from the high-temperature ignition part to the low-temperature fuel part can be reduced, and the temperature of the ignition part is increased. In recent years, a method has been established to realize a kilo-tesla-class strong magnetic field with good reproducibility by driving a capacitor coil target with a laser.

In this study, we first experimentally revealed the effect of a strong magnetic field on plasma motion using this method. By applying a magnetic field of about 100T, the Hall parameter easily becomes more than unity at the ablation region. When Hall parameter has nonzero value, the thermal conductivity reduce in the external magnetic field. Because anisotropic thermal diffusion reduces the thermal energy loss from the ablated plasma to its cold peripheral region that is transverse

to the magnetic field lines, the temperature and pressure of the ablated plasma increase significantly, resulting in acceleration of the polystyrene foil by the larger pressure gradient. The enhancement of hydrodynamic perturbation growth has been also clarified experimentally. The magnetic field lines move together with the ablated plasma due to its large magnetic Reynold's number. The external magnetic field is compressed (decompressed) at the valley (peak) of the sinusoidal perturbation due to the accumulation of the ablated plasma. The temperature increases at the valley due to the anisotropic thermal conduction in the perturbed magnetic field structure. The pressure distribution becomes spatially non-uniform, and lead to enhancement of the perturbation growth. We experimentally revealed that an external magnetic field notably affects hydrodynamics due to anisotropic thermal transport, even when the magnetic field pressure is much lower than the plasma pressure.

In addition, we experimentally verified a heating method that heats fusion fuel efficiently by heat transport. A steep temperature gradient is generated by resistive heating at the ablation region in a strong magnetic field. The diffusive heating mechanism in which thermal electrons transport their energy diffusively from the laser heated hot region to the cold dense region plays an essential role to heat the core plasma over keV range. We have achieved experimentally 2.2 petapascal pressure of ultra-high-energy-density (UHED) state with 4.6 kJ of the total laser energy that is one order of magnitude lower than the energy used in the conventional implosion scheme. These findings clarified that MFI is an efficient way to create the petapascal UHED state that is a unique testbed for ICF.

Acknowledgments

First, I want to express my deepest gratitude to my academic advisor, Professor Shinsuke Fujioka. He encouraged my research and gave me the opportunity to grow as an experimentalist since I was an undergraduate student.

I would like to express my appreciation to Lecturer Yasunobu Arikawa, Professor Hiroshi Azechi, Associate Professor Hiroshi Sawada, Professor Yasuhiko Sentoku, Assistant Professor Takayoshi Sano, Associate Professor Hideo Nagatomo, and Professor Beg Farhat that allowed me to follow my interests and helped me in any way they could to allow me to have the most fruitful possible experience.

I would like to acknowledge Prof.Mitsuo Nakai, Prof.Hiroaki Nishimura, Prof.Hiroyuki Shiraga, Prof.Takayoshi Norimatsu, Prof.Keisuke Shigemori, Associate Prof.Akifumi Yogo, Associate Prof.Youichi Sakawa, Lecturer Alessio Morace, Lecturer Natsumi Iwata, Assistant Prof.Kohei Yamanoi, Dr.Atsushi Sunahara (Institute for Laser Technology), Associate Prof.Tomoyuki Johzaki (Hiroshima

University), Associate Prof.Tetso Ozaki (National Institute for Fusion Science), and Prof.Hitoshi Sakagami (National Institute for Fusion Science) for providing me a wonderful research environment. I would like to acknowledge the dedicated technical support of the staff at Institute of Laser Engineering, Osaka University.

And thank yous all around to a multitude of people. I had the privilege of learning from: Shohei Sakata, Sadaoki Kojima, Yuki Abe, Lee Seungho, Utsugi Masaru, King Fai Farly Law, Hiroki Morita, Masayasu Hata, Takashi Shiroto, Hiroki Kato, Yuki Iwasa, Daiki Kawahito, Takashi Asahina, Naoki Higashi.

I would especially thank Associate Prof.Joao Jorge Santos, Dr.Hui Chen, Prof.Zhe Zhang, Dr.Xavier Vaisseau, Dr.Mathieu Bailly-Grandvaux, Dr.Min Sang Cho and all the international groups. I had the fortune to work with: at University of Bordeaux, LULI, LLNL, CLPU, CELIA, Chinese Academy of Sciences, GIST.

This work was supported by Grant-in-Aid for JSPS Research Fellow (No. 18J11354) from the Japan Society for the Promotion of Science. This work was supported by Overseas Challenge Program for Young Researchers (1039961) from the Japan Society for the Promotion of Science.

At last, I thank my parents for supporting me.

Bibliography

Asahina, Takashi et al. (2019). "High Energy Density Physics Enhanced heat transport in ablation plasma under transverse magnetic field by upper hybrid resonance heating". In: *High Energy Density Physics* 30.September 2018, pp. 8–12. ISSN: 1574-1818. DOI: 10.1016/j.hedp.2018.12.003. URL: https://doi.org/10.1016/j.hedp.2018.12.003.

Azechi, H. et al. (2007). "Comprehensive diagnosis of growth rates of the ablative Rayleigh-taylor instability". In: *Physical Review Letters* 98.4.

Bailly-Grandvaux, M. et al. (2018). "Guiding of relativistic electron beams in dense matter by laser-driven magnetostatic fields". In: *Nature Communications* 9.1, pp. 1–8. ISSN: 20411723. DOI: 10.1038/s41467-017-02641-7. arXiv: 1608.08101. URL: http://dx.doi.org/10.1038/s41467-017-02641-7.

Betti, R. et al. (2010). "Thermonuclear ignition in inertial confinement fusion and comparison with magnetic confinement". In: *Physics of Plasmas* 17.5. ISSN: 1070664X. DOI: 10.1063/1.3380857.

Braginskii, S. I. (1965). "Transport processes in a plasma". In: *Reviews of Plasma Physics* 1.205.

Casey, D. T. et al. (2017). "Thermonuclear reactions probed at stellar-core conditions with laser-based inertial-confinement fusion". In: *Nature Physics* 13.12, pp. 1227–1231. ISSN: 17452481. DOI: 10.1038/nphys4220.

Chang, P. Y. et al. (2011). "Fusion yield enhancement in magnetized laser-driven implosions". In: *Physical Review Letters* 107.3, pp. 2–5. ISSN: 00319007. DOI: 10.1103/PhysRevLett.107.035006.

CHESTER, W. (Jan. 1954). "THE DIFFRACTION AND REFLECTION OF SHOCK WAVES". In: *The Quarterly Journal of Mechanics and Applied Mathematics* 7.1, pp. 57–82. ISSN: 0033-5614. DOI: 10.1093/qjmam/7.1.57. eprint: https://academic.oup.com/qjmam/article-pdf/7/1/57/5300149/7-1-57.pdf. URL: https://doi.org/10.1093/qjmam/7.1.57.

Chung, H. K. et al. (2005). "FLYCHK: Generalized population kinetics and spectral model for rapid spectroscopic analysis for all elements". In: *High Energy Density Physics* 1.1, pp. 3–12. ISSN: 15741818. DOI: 10.1016/j.hedp.2005.07.001.

Cobblea, J. A. (2004). "High resolution laser-driven proton radiography". In: 1775.May 2002. DOI: 10.1063/1.1494128.

Constantin, Carmen G et al. (2009). "Design , construction , and calibration of a three-axis , high-frequency magnetic probe (B-dot probe) as a diagnostic for exploding plasmas Design , construction , and calibration of a three-axis , high-frequency magnetic probe „ B -dot probe . . . as a diagnostic for exploding plasmas". In: November. DOI: 10.1063/1.3246785.

Daido, H. et al. (1986). "Generation of a strong magnetic field by an intense CO2 laser pulse". In: *Physical Review Letters* 56.8, pp. 846–849. ISSN: 00319007. DOI: 10.1103/PhysRevLett.56.846.

Denisiuk, Yu. N. (1963). "On the reflection of the optical properties of object in optical field scattered on it". In: *Opt. Spectrosc.* 15, pp. 522–530.

Do, A et al. (2017). "High-resolution quasi-monochromatic X-ray imaging using a Fresnel phase zone plate and a multilayer mirror". In: *Citation: Review of Scientific Instruments* 88. DOI: 10.1063/1.4973296. URL: https://doi.org/10.1063/1.4973296%20http://aip.scitation.org/toc/rsi/88/1.

Everson, E. T. et al. (2009). "Design, construction, and calibration of a three-axis, high-frequency magnetic probe (B-dot probe) as a diagnostic for exploding plasmas". In: *Review of Scientific Instruments* 80.11. ISSN: 00346748. DOI: 10.1063/1.3246785.

Fujioka, Shinsuke, Takashi Fujiwara, et al. (2010). "Monochromatic x-ray radiography for areal-density measurement of inertial fusion energy fuel in fast ignition experiment". In: *Review of Scientific Instruments* 81.10, pp. 2008–2011. ISSN: 00346748. DOI: 10.1063/1.3494383.

Fujioka, Shinsuke, Tomoyuki Johzaki, et al. (2015). "Heating efficiency evaluation with mimicking plasma conditions of integrated fast-ignition experiment". In: *Physical Review E - Statistical, Nonlinear, and Soft Matter Physics* 91.6, pp. 1–8. ISSN: 15502376. DOI: 10.1103/PhysRevE.91.063102.

Fujioka, Shinsuke, Hideaki Takabe, et al. (2009). "X-ray astronomy in the laboratory with a miniature compact object produced by laser-driven implosion". In: *Nature Physics* 5.11, pp. 821–825. ISSN: 1745-2473. DOI: 10.1038/nphys1402. arXiv: 0909.0315v1. URL: http://www.nature.com/nphys/journal/v5/n11/abs/nphys1402.html.

Fujioka, Shinsuke, Zhe Zhang, et al. (2013). "Kilotesla magnetic field due to a capacitor-coil target driven by high power laser." In: *Scientific reports* 3, p. 1170. ISSN: 2045-2322. DOI: 10.1038/srep01170. URL: http://www.nature.com/srep/2013/130130/srep01170/full/srep01170.html.

G.Brown, Thomas (2004). "The Optics Encyclopedia". In: *WILEY-VCH* 5.

Gao, Lan et al. (2016). "Ultrafast proton radiography of the magnetic fields generated by a laser-driven coil current". In: *Physics of Plasmas* 23.4. ISSN: 10897674. DOI: 10.1063/1.4945643. URL: http://dx.doi.org/10.1063/1.4945643.

Glendinning, S. G. et al. (1997). "Measurement of a dispersion curve for linear-regime rayleigh-taylor growth rates in laser-driven planar targets". In: *Physical Review Letters* 78.17, pp. 3318–3321. ISSN: 10797114. DOI: 10.1103/PhysRevLett.78.3318.

Henke, Burton L. (1993). "X-Ray-Interactions–Photoabsorption–Scattering–Transmission–and-Reflection-at-E—50-30-000-eV–Z—1-92_1993_Atomic-Data-and-Nuclear-Data-Tables". In: ISSN: 0092-640X. DOI: 10.1006/ADND.1993.1013.

Huba, J. D. (2013). "NRL PLASMA FORMULARY". In: *NRL PLASMA FORMULARY*.

Iwasa, Yuki et al. (2017). "Cu-oleate microspheres fabricated by emulsion method as novel targets for fast ignition laser fusion experiments". In: *Fusion Engineering and Design* 125.November, pp. 89–92. ISSN: 09203796. DOI: 10.1016/j.fusengdes.2017.11.009. URL: https://doi.org/10.1016/j.fusengdes.2017.11.009.

Jarrott, L. C. et al. (2016). "Visualizing fast electron energy transport into laser-compressed high-density fast-ignition targets". In: *Nature Physics* advance on.January, pp. 1–7. ISSN: 1745-2473. DOI: 10.1038/nphys3614. URL: http://dx.doi.org/10.1038/nphys3614.

Kemp, A. J. et al. (2006). "Collisional relaxation of superthermal electrons generated by relativistic laser pulses in dense plasma". In: *Physical Review Letters* 97.23.

Keskinbora, Kahraman et al. (2013). "Rapid prototyping of fresnel zone plates via direct Ga+ ion beam lithography for high-resolution x-ray imaging". In: *ACS Nano* 7.11, pp. 9788–9797. ISSN: 19360851. DOI: 10.1021/nn403295k.

Krokhin, O. N. and V. B. Rozanov (1973). "ESCAPE OF alpha PARTICLES FROM A LASER-PULSE-INITIATED THERMONUCLEAR REACTION." In: *Sov J Quantum Electron* 2.4, pp. 393–394. ISSN: 0049-1748. DOI: 10.1070/qe1973v002n04abeh004476.

Law, K. F F et al. (2016). "Direct measurement of kilo-tesla level magnetic field generated with laser-driven capacitor-coil target by proton deflectometry". In: *Applied Physics Letters* 108.9, pp. 1–6. ISSN: 00036951. DOI: 10.1063/1.4943078. URL: http://dx.doi.org/10.1063/1.4943078.

Le Pape, S. et al. (2018). "Fusion Energy Output Greater than the Kinetic Energy of an Imploding Shell at the National Ignition Facility". In: *Physical Review Letters* 120.24, p. 245003. ISSN: 10797114. DOI: 10.1103/PhysRevLett.120.245003. URL: https://doi.org/10.1103/PhysRevLett.120.245003.

Manuel, M. J E et al. (2012). "First measurements of Rayleigh-Taylor-induced magnetic fields in laser-produced plasmas". In: *Physical Review Letters* 108.25, pp. 1–5. ISSN: 00319007. DOI: 10.1103/PhysRevLett.108.255006.

Nagatomo, H., T. Johzaki, T. Asahina, et al. (2015). "Computational study of magnetic field compression by laser-driven implosion". In: *Nuclear Fusion* 55.9, p. 093028. ISSN: 0029-5515. DOI: 10.1088/0029-5515/55/9/093028. URL: http://stacks.iop.org/0029-5515/55/i=9/a=093028?key=crossref.c084663919821fe5b1959a13fc38927a.

Nagatomo, H., T. Johzaki, A. Sunahara, et al. (2013). "Computational study of strong magnetic field generation in a nonspherical, cone-guided implosion". In: *Nuclear Fusion* 53.6, p. 063018. ISSN: 0029-5515. DOI: 10.1088/0029-5515/53/6/063018. URL: http://stacks.iop.org/0029-5515/53/i=6/a=063018?key=crossref.f290b53beeaddd4ca6971919a92ef5fd.

Nishiguchi, A. et al. (1984). "Convective amplification of magnetic fields in laser-produced plasmas by the Nernst effect". In: *Physical Review Letters* 53.3, pp. 262–265. ISSN: 00319007. DOI: 10.1103/PhysRevLett.53.262.

Passoni, Matteo (2010). "Target normal sheath acceleration: theory, comparison with experiments and future perspectives". In: *New Journal of PhysicsPhysics* 12.045012, p. 14. DOI: 10.1088/1367-2630/12/4/045012.

Peres, Asher (1979). "Fusion cross sections and thermonuclear reaction rates". In: *Journal of Applied Physics* 50.9, pp. 5569–5571. ISSN: 00218979. DOI: 10.1063/1.326748.

Perkins, L. J. et al. (2013). "Two-dimensional simulations of thermonuclear burn in ignition-scale inertial confinement fusion targets under compressed axial magnetic fields". In: *Physics of Plasmas* 20.7. ISSN: 1070664X. DOI: 10.1063/1.4816813.

R.Kodama (2001). "Fast heating of ultrahigh-density plasma as a step towards laser fusion ignition". In: *Nature* 412, pp. 798–802. ISSN: 13652966. DOI: 10.1093/mnras/stx1978. arXiv: arXiv:1706.03720v1.

RADIA (n.d.). In: (). URL: http://www.esrf.eu/Accelerators/Groups/InsertionDevices/Software/Radia/Documentation/Introduction.

Regan, S. P. et al. (2016). "Demonstration of Fuel Hot-Spot Pressure in Excess of 50 Gbar for Direct-Drive, Layered Deuterium-Tritium Implosions on OMEGA". In: *Physical Review Letters* 117.2, pp. 6–10. ISSN: 10797114. DOI: 10.1103/PhysRevLett.117.025001.

Reich, Ch et al. (2000). "Yield optimization and time structure of femtosecond laser plasma Kα sources". In: *Physical Review Letters* 84.21, pp. 4846–4849. ISSN: 10797114. DOI: 10.1103/PhysRevLett.84.4846.

Remington, Bruce A., R. Paul Drake, and Dmitri D. Ryutov (2006). "Experimental astrophysics with high power lasers and Z pinches". In: *Reviews of Modern Physics* 78.3, pp. 755–807. ISSN: 00346861. DOI: 10.1103/RevModPhys.78.755.

Royle, R. et al. (2017). "Kinetic modeling of X-ray laser-driven solid Al plasmas via particle-in-cell simulation". In: *Physical Review E* 95.6, pp. 1–11. ISSN: 24700053. DOI: 10.1103/PhysRevE.95.063203.

Sakaiya, T et al. (2002). "Ablative Rayleigh-Taylor Instability at Short Wavelengths Observed with Moiré Interferometry". In: 52. DOI: 10.1103/PhysRevLett.88.145003.

Sakata, Shohei et al. (2018). "Magnetized fast isochoric laser heating for efficient creation of ultra-high-energy-density states". In: *Nature Communications* 9.1, p. 3937. ISSN: 2041-1723. DOI: 10.1038/s41467-018-06173-6. URL: http://www.nature.com/articles/s41467-018-06173-6.

Sano, Takayoshi, Tsuyoshi Inoue, and Katsunobu Nishihara (2013). "Critical Magnetic Field Strength for Suppression of the Richtmyer-Meshkov Instability in Plasmas". In: *Physical Review Letters* 111, p. 205001. ISSN: 0031-9007. DOI: 10.1103/PhysRevLett.111.205001. arXiv: 1310.6136. URL: http://link.aps.org/doi/10.1103/PhysRevLett.111.205001.

Santos, J. J. et al. (2015). "Laser-driven platform for generation and characterization of strong quasi-static magnetic fields". In: *New Journal of Physics* 17.8. ISSN: 13672630. DOI: 10.1088/1367-2630/17/8/083051. arXiv: 1503.00247.

Sawada, H., S. Lee, et al. (2016). "Flash Kα radiography of laser-driven solid sphere compression for fast ignition". In: *Applied Physics Letters* 108.25, p. 254101. DOI: 10.1063/1.4954383. URL: http://dx.doi.org/10.1063/1.4954383.

Sawada, H., Y. Sentoku, et al. (2019). "Monochromatic 2D Kα Emission Images Revealing Short-Pulse Laser Isochoric Heating Mechanism". In: *Physical Review Letters* 122.15, p. 155002. ISSN: 10797114. DOI: 10.1103/PhysRevLett.

122.155002. URL: https://doi.org/10.1103/PhysRevLett.122.155002.

Sentoku, Y. and A. J. Kemp (2008). "Numerical methods for particle simulations at extreme densities and temperatures: Weighted particles, relativistic collisions and reduced currents". In: *Journal of Computational Physics* 227.14, pp. 6846–6861. ISSN: 00219991. DOI: 10.1016/j.jcp.2008.03.043.

Smalyuk, V. A. et al. (2008). "Rayleigh-taylor growth stabilization in direct-drive plastic targets at laser intensities of ???1??1015W/cm2". In: *Physical Review Letters* 101.2, pp. 1–4. ISSN: 00319007. DOI: 10.1103/PhysRevLett.101.025002.

Spitzer, Lyman and Richard Härm (Mar. 1953). "Transport Phenomena in a Completely Ionized Gas". In: *Phys. Rev.* 89 (5), pp. 977–981. DOI: 10.1103/PhysRev.89.977. URL: https://link.aps.org/doi/10.1103/PhysRev.89.977.

Srinivasan, Bhuvana and Xian Zhu Tang (2012). "Mechanism for magnetic field generation and growth in Rayleigh-Taylor unstable inertial confinement fusion plasmas". In: *Physics of Plasmas* 19.8, pp. 1–5. ISSN: 1070664X. DOI: 10.1063/1.4742176.

Stefano, Atzeni (2003). "The Physics of Inertial Fusion". In: *OXFORD UNIVERSITY PRESS*.

Stone, James M. and Thomas Gardiner (2007). "Nonlinear evolution of the magnetohydrodynamic Rayleigh-Taylor instability". In: *Physics of Fluids* 19.9. ISSN: 10706631. DOI: 10.1063/1.2767666. arXiv: 0707.1022.

Strozzi, D. J. et al. (2012). "Fast-ignition transport studies: Realistic electron source, integrated particle-in-cell and hydrodynamic modeling, imposed magnetic fields". In: *Physics of Plasmas* 19.7. ISSN: 1070664X. DOI: 10.1063/1.4739294. arXiv: arXiv:1205.1594v1.

Tabak, Max et al. (1994). "Ignition and high gain with ultrapowerful lasers". In: *Physics of Plasmas* 1.5, pp. 1626–1634. ISSN: 1070664X. DOI: 10.1063/1.870664.

Theobald, W. et al. (2014). "Time-resolved compression of a capsule with a cone to high density for fast-ignition laser fusion". In: *Nature Communications* 5, pp. 1–7. ISSN: 20411723. DOI: 10.1038/ncomms6785.

Tikhonchuk, V. T. et al. (2017). "Quasistationary magnetic field generation with a laser-driven capacitor-coil assembly". In: *Physical Review E* 96.2, p. 023202. ISSN: 2470-0045. DOI: 10.1103/PhysRevE.96.023202. URL: https://link.aps.org/doi/10.1103/PhysRevE.96.023202.

Troussel, Ph et al. (2005). "Wolter-like high resolution x-ray imaging microscope for Rayleigh Taylor instabilities studies". In: *Review of Scientific Instruments* 76.6. ISSN: 00346748. DOI: 10.1063/1.1902803.

Vinko, S. M. et al. (2015). "Investigation of femtosecond collisional ionization rates in a solid-density aluminium plasma". In: *Nature Communications* 6, pp. 1–7. ISSN: 20411723. DOI: 10.1038/ncomms7397.

Zhou, Ye (2017). "Rayleigh–Taylor and Richtmyer–Meshkov instability induced flow, turbulence, and mixing. I". In: *Physics Reports* 720-722, pp. 1–136. ISSN: 03701573. DOI: 10.1016/j.physrep.2017.07.005. URL: http://dx.doi.org/10.1016/j.physrep.2017.07.005.

Zhu, B. J. et al. (2015). "Strong magnetic fields generated with a simple open-ended coil irradiated by high power laser pulses". In: *Applied Physics Letters* 107.26. ISSN: 00036951. DOI: 10.1063/1.4939119.

A. Sinusoidally corrugated target

A.1 Hot press method for the initially corrugated target

For simplicity, the initially corrugated target is widely used in hydrodynamic instability experiments such as mentioned in chapter3. In general, a 30 - 150 μm wavelength sinusoidal perturbation with initial amplitude a_0 = 1 - 10 μm was usually imposed on planar polystyrene(C_8H_8) foils, whose initial thickness l_0 = 10 or 100-μm. Polystyrene has a low atomic number, therefore, it emits few self-emission of x-rays, making it suitable for x-ray backlight measurement. The accuracy of a the initially corrugated target directly affects the error of the experiment, therefore it is necessary to make the target with high accuracy and small individual differences.

Previously, we have made such a target by the hot press, as shown in Fig.A.1. In this method, a polystyrene foil is placed on a tightly wound rod of tungsten wire with a diameter equal to the wavelength of the initial sinusoidal perturbation. Then apply pressure with a clip using a glass slide. The amplitude of the target is adjusted by adding parylene between the polystyrene foil and the tungsten wire. Finally, it is heated in an oven at a temperature(= 120 - 130°C) between the glass transition point and the melting point of polystyrene. Example fabrication parameters of the hot press method are listed in TableA.1. With this method, only one target can be manufactured at a time. The drawback was that the accuracy of the pinch and the placement of the foil at that time caused variations in individual targets.

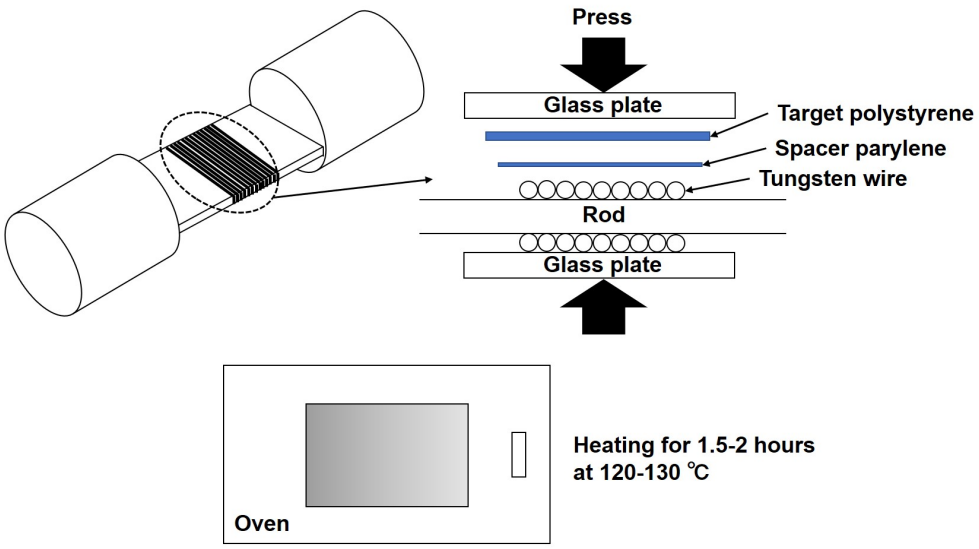

Figure A.1: Manufacturing method of disturbance target by hot press.

Diameter of tungsten wire	Thickness of parylene film	Amplitude of the target
μm	μm	μm
50	20	1.6 ± 0.1
50	15	3.2 ± 0.1
100	20	5.6 ± 0.3
150	20	7.9 ± 0.5

Table A.1: Fabrication parameters of hot press method. The wavelength of the initial sinusoidal perturbation equal to diameter of tungsten wire. Amplitude of the target is adjusted by adding parylene film

A.2 Photoresist method for the initially corrugated target

We need to develop another method for the target with high accuracy and small individual differences. The method is described below.

- The silicon substrate is coated with the photoresist(PMER P-LA900PM).
- A sinusoidal pattern is drawn using a high-speed maskless UV exposure system on the photoresist.
- The silicon substrate is etched using a magnetic neutral discharge dry etching system.
- A plastic foil is formed on the substrate on which the sinusoidal pattern to transfer the sinusoidal pattern to the plastic foil, as shown in Fig.A.2.

It is confirmed that the same pattern as the substrate was transferred to the plastic plate. Once the silicon substrate is made, the sinusoidal corrugated polystyrene foil can be transferred many times with good reproducibility. We were able to establish a method to produce sinusoidally corrugated targets with high accuracy and small individual differences. The method contributes to improving the accuracy of experiments.

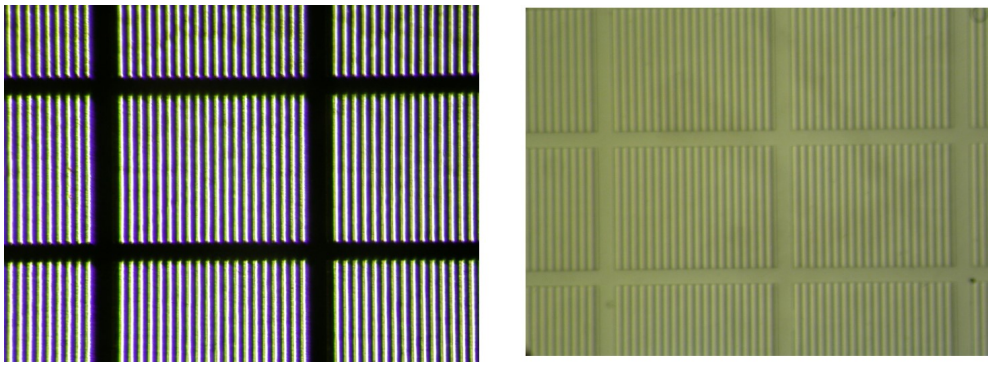

Figure A.2: Photo of the frame (left) and transferred plastic foil (right)

B. Fresnal Phase Zone Plate

B.1 Flash X-ray backlight technique using a Fresnel phase zone plate for measuring interfacial instability

Understanding the physics of interfacial instabilities is of great interest in many fields such as astrophysical fluid dynamics[1] as well to the achievement of inertial confinement fusion (ICF)[2]. X-ray measurements are powerful diagnostics for high energy density plasma. Especially, X-ray imager with high resolution and high sensitivity is indispensable to measure the instability growth. A lot of X-ray imager has been developed over the decades.

Currently, the pinhole diagnostics are commonly used as X-ray imagers in laser plasma experiments. They are easy to set up and less expensive to manufacture. However, their resolution is directly linked to their pinhole diameter thus better resolution leads to low efficiency. And they don't have wavelength selectivity therefor they need filtering. It is not possible to select a limited spectral bandwidth without the signal loss by filtering.

The idea to use a diffraction for recording hard X-ray images has been published in 1963[3]. The application of this idea known as Fresnel Phase Zone Plate(FPZP) designed for focusing and imaging hard X-ray. FPZPs work as less geometrical restriction and consideration X-ray imager like the pinhole diagnostics. FPZPs are not commonly used in laser-plasma experiments mainly due to expensive to manufacture. Although they can provide high spatial resolution X-ray images without sacrificing the efficiency, thanks to their larger diameter with precision manufacturing of thin rings.

[1] Remington, Drake, and Ryutov 2006.
[2] Troussel et al. 2005.
[3] Denisiuk 1963.

The demonstration of FPZP as high resolution imager in laser-plasma expriments has been done for the first time in Ref. [4]. An experiment has been performed at the LULI2000 laser facility to image the Al$-He_\beta$ from plasma's self-emission zone. It was demonstrated that Fresnel-lens-based X-ray imager can provide a reusable and versatile high-resolution X-ray microscope for laser-plasma-interaction diagnostic and can be potential imaging diagnostics for high power laser facility.

In this study, we have tested the FPZP coupled with flash X-ray backlight technique[5] at the GEKKO-LFEX laser facility at the Institute of Laser Engineering. A sinusoidally corrugated polystyrene foil was irradiated by GEKKO beams. Flash Ti$-K_\alpha$ X-ray was produced by LFEX beam irradiating on a Ti foil. The flash X-rays were passing through the sinusoidally corrugated polystyrene foil and imaged by the FPZP on an imaging plates. It was demonstrated that the growth of the sinusoidal perturbation was clearly observed with the flash X-ray backlight technique using a FPZP.

The FPZP has been used in many fields for a high spatially resolving imaging[6]. In our case, it was used to image Ti$-K_\alpha$ emissions produced by LFEX laser. The FPZP we used for imaging is consists of multiple rings made of tantalum. A phase difference occurs between the X-ray that passed through the ring part and that passed through the cavity part. The X-rays with phase differences interfere with each other in the same phase on the focal plane and imaging becomes possible. When the light of the wavelength λ is incident on the FPZP with the innermost ring radius a, the light is focused at the point of the focal length $f = a^2/\lambda$. In principle imaged by FPZP can be calculated according to the following expression,

$$\frac{1}{f} = \frac{1}{r} + \frac{1}{R} \tag{B.1}$$

where r is the distance between the light source and the FPZP, and R is the distance between the FPZP and the light receiving surface. The focal length is a function of the wavelength, therefore the wavelength differs from the predetermined value, the focal position is shifted and the image is not formed. FPZP itself has wavelength selectivity. The fabrication parameters of the FPZP are listed on Table B.1. The Innermost ring radius a of the FPZP is 6μm, therefore the focal distance for Ti$-K_\alpha$ X-ray is 131mm.

[4] Do et al. 2017.

[5] Fujioka, Fujiwara, et al. 2010; Sawada, Lee, et al. 2016.

[6] Keskinbora et al. 2013.

Material	Tantalum
Innermost ring radius (a)	6μm
Outermost ring radius (d)	52μm
Thickness	1μm
Last zone width	0.15μm

Table B.1: FPZP fabrication parameters. The FPZP was manufactured by NTT AT, Inc.

Fig.B.1(a) shows the schematics of FPZP imaging. When the monochromatic parallel X-ray beam incident to FPZP, the 1st order light is focused at the point of the focal length. 0th, 3rd and more higher order of unfocused light are also detected on the detector. The efficiency on the detector of the kth order can be calculated with the following equations[7].

$$\eta_0 = \frac{1}{4}\left(1+2e^{\frac{-2\pi\beta e}{\lambda}}\cos(\frac{-2\pi\delta e}{\lambda})+e^{\frac{-4\pi\beta e}{\lambda}}\right) \tag{B.2}$$

$$\eta_k = \frac{1}{\pi^2 k^2}\left(1-2e^{\frac{-2\pi\beta e}{\lambda}}\cos(\frac{-2\pi\delta e}{\lambda})+e^{\frac{-4\pi\beta e}{\lambda}}\right) \tag{B.3}$$

Here δ and β are the real and imaginary part of the refraction index $n = 1-\delta-i\beta$. Henke's table[8] is used for calculating δ and β. Using these formulas, the thickness is selected to maximize the ratio of 1st order and the other orders. Fig.B.1(b) shows a comparison of the efficiencies of the 0th, 1st, and 3rd orders for a thickness of 1μm tantalum. The efficiency of the 0th and 3rd orders around Ti$-K_\alpha$(= 4510 eV) X-ray are small compare to that of the 1st order.

It is difficult to produce a monochromatic X-ray by laser. Fig.B.2(a) shows typical X-ray spectra from laser irradiated titanium foil in the range of 4300 to 4900 eV. The peaks at 4510 and 4750 are Ti$-K_\alpha$ and Ti$-He_\alpha$ respectively. Even this situation the FPZP can provide high spatial resolution X-ray images, thanks to their wavelength selectivity. The intensity of detected X-ray on the detector $I(\sigma)$ can be calculated by the following equation[9].

$$\frac{4\pi^2}{(rR\lambda)^2}\left|\int_0^d \rho\exp\left(\frac{i\pi(R+r)\rho^2}{rR\lambda}\right)J_o\left(\frac{2\pi\sigma\rho}{R\lambda}\right)d\rho\right|^2 \tag{B.4}$$

[7] G.Brown 2004.
[8] Henke 1993.
[9] G.Brown 2004.

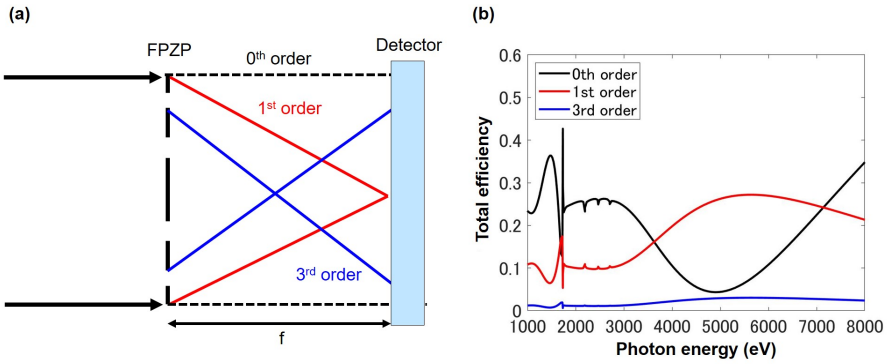

Figure B.1: (a) The schematics of FPZP imaging, showing the various diffraction orders. (b) The Efficiency of 0th, 1st, and 3rd orders imaged by the 1.0 μm thick tantalum FPZP

where σ is a distance from center of the IP, d(=52μm) is an outermost ring radius of the FPZP, ρ is a distance from center of the FPZP. The normalized intensity is calculated from (B.4) with varios X-ray energy, as shown in Fig.B.2(b). The object to FPZP distance r is 144 mm and the FPZP to IP distance R is 1440 mm corresponding to our backlight experiment. Ti$-K_\alpha$ X-ray is well focused on the detector. Other X-rays near Ti$-K_\alpha$ line is also focused on the detector. However, there are no strong characteristic X-ray emissions around Ti$-K_\alpha$ X-ray. It is important to reduce chromatic aberration.

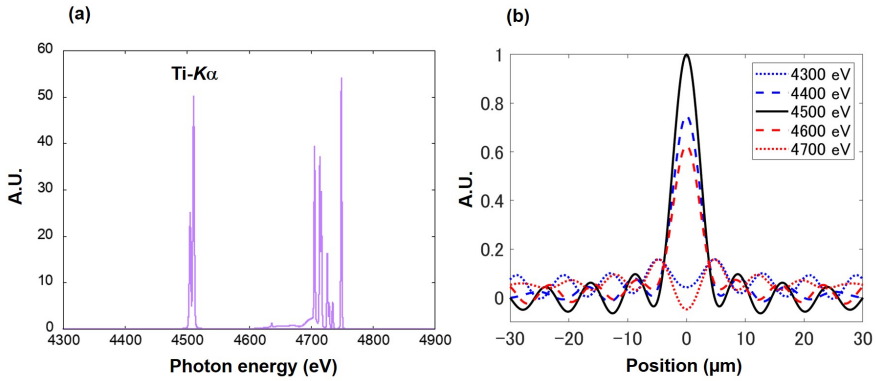

Figure B.2: (a) Typical emission from laser irradiated titanium foil. (b) The imaging function with varios X-ray energy.

The backlight imaging experiment was carried out to determine the spatial

resolution. The diagnostic setup is presented in Fig.B.3(a). The 1.6ps, 1kJ LFEX beam were focused on Ti foil for producing the flash Ti$-K_\alpha$ X-ray. The Ti$-K_\alpha$ X-ray is passing through a gold mesh and imaged on the imaging plate(IP). A 50-μm-thick beryllium foil was placed in front of the FPZP for protecting from debris. The gold mesh to FPZP distance r is 144 mm and the FPZP to IP distance R is 1440 mm corresponding to a magnification around 10. The backlight image of the gold mesh target was measured, as shown in Fig.B.3(b). The dot and solid lines of Fig.B.3(c) are a line profile of the gold mesh image and a calculated profile obtained by convoluting an ideal gold mesh image(dotted line) and a Gaussian point spread function. This comparison indicates the spatial resolution at FWHM is $\delta = 5.0 \pm 1.0 \mu$m.

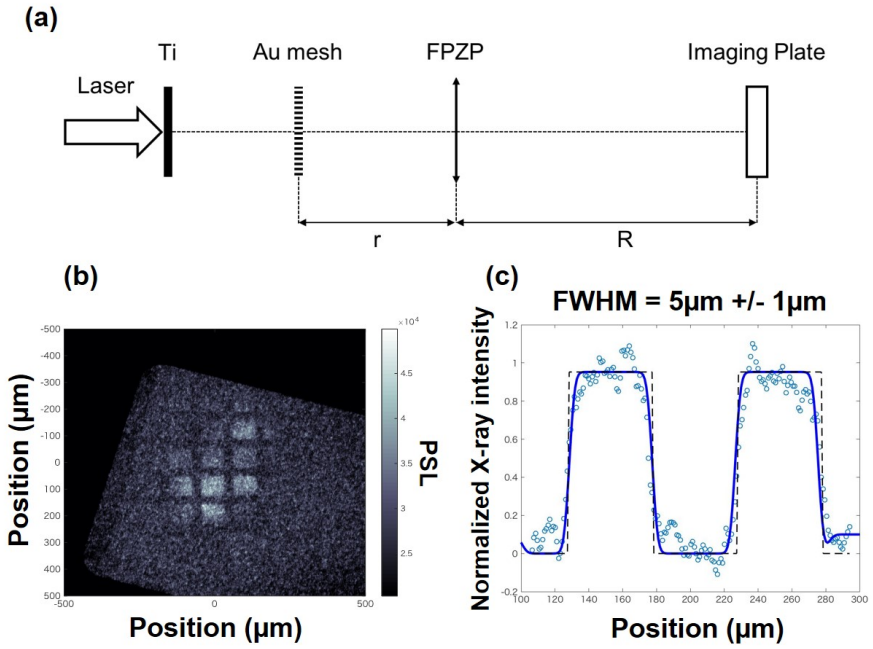

Figure B.3: (a) Experimental setup of the backlight imaging experiment. The gold mesh to FPZP distance r is 144 mm and the FPZP to IP distance R is 1440 mm corresponding to a magnification around 10. (b) X-ray radiograph of the gold mesh backlight by TiK_α X-ray. (c) Line profiles of the measured backlight image (dot) and a calculated profile (solid line) obtained by convoluting an ideal profile (dotted line) and a Gaussian point spread function 5 μm of FWHM.

The Richtmyer-Meshkov Instability(RMI)[10] which is one of the major interfacial instabilitie was also measured. A 150 μm wavelength sinusoidal perturbation with initial amplitude 7.9 $\pm$ 0.5 μm was imposed on rear surface of planar polystyrene foils, whose thickness 50 μm, as shown in Fig.B.4(a). Two 532 nm beams of the GEKKO-XII laser were used to drive the foil at an intensity of 4.0 $\pm$ 0.1 $\times$ $10^{13}\,\mathrm{W/cm^2}$ from front surface. The RMI occurs when an incident shock strikes a corrugated density gap. A strong shock waves grow through the inhomogeneitie. The shadow was measured by flash X-ray backlight technique using FPZP after 10ns laser irradiation, as shown in Fig.B.4(b). Time duration of Ti$-K_\alpha$ pulse measurement was'nt performed in this experiment, but according to previous theoretical study[11], it is reasonable to assume that the duration of the X-ray pulse is of the order of LFEX laser of 1.6 ps. It enables to record an instantaneous image of the sinusoidal perturbation. The width of the polystyrene foil along the line of sight of the diagnostics was $l = 400$ μm. When the Ti$-K_\alpha$ X-ray pass through the target with the initial intensity I_0, the intensity after passing through the target I is calculated by $I = I_0 e^{-\mu\rho l}$ where $\mu = 24\,\mathrm{cm^2/g}$ and $\rho = 1.1\,\mathrm{g/cm^3}$ are mass absorption rate of a polystyrene for the Ti$-K_\alpha$ X-ray and mass density. The target reduces the initial X-ray intensity by a factor of 0.35. The target boundary is defined by its intensity point. Fig.B.4(c) show the trace of rear surface of the target. The evaluated amplitude is 11.6 +2.2/-2.3 μm after 10ns laser irradiation. We suceed to measure the instability growth clearly even under the influence of self-emission from plastic foil.

In this study, we have tested FPZP at the GEKKO-LFEX laser facility at the Institute of Laser Engineering. Nanosecond GEKKO-XII laser beams were used for driving a sinusoidally modulated polystyrene foil and picosecond LFEX laser was used for producing flash X-ray to measure the instability growth. The resolution of our FPZP at FWHM is $\delta_{\mathrm{tot}} = 5.0 \pm 1.0 \mu$m which was evaluated from the sharp edge of the mesh target. The Richtmyer-Meshkov instability was also measured. It was demonstrated that the growth of the sinusoidal perturbation was clearly observed with the flash X-ray backlight technique using a FPZP even under the influence of self-emission.

[10] Sano, Inoue, and Nishihara 2013.
[11] Reich et al. 2000.

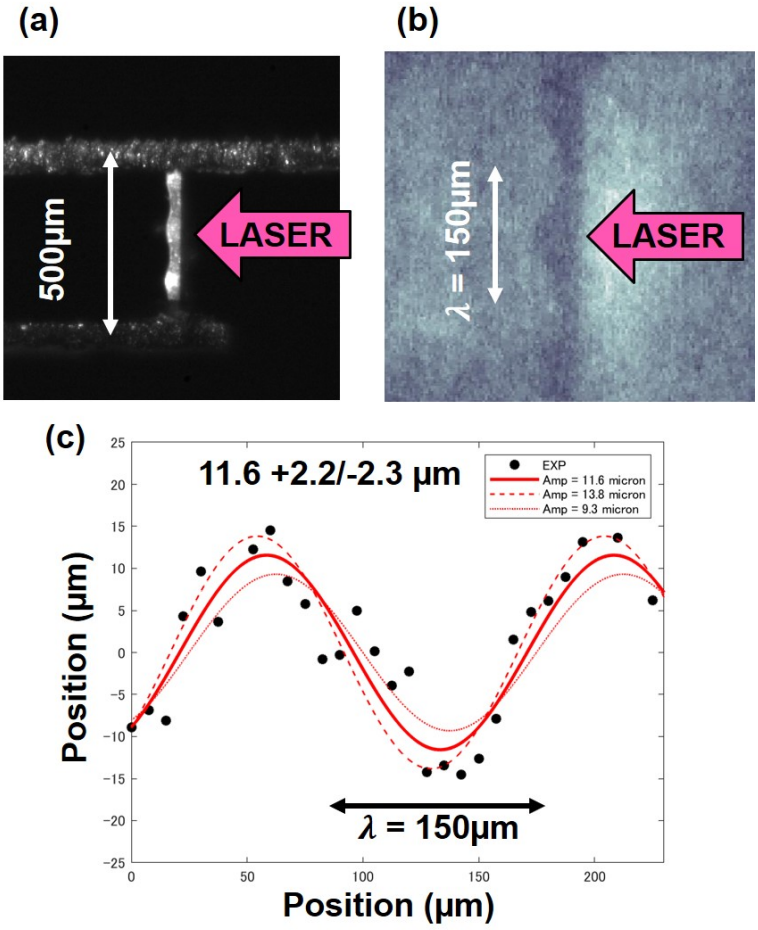

Figure B.4: (a) A picture of sinusoidally corrugated polystyrene foil. (b) The shadow measured by flash X-ray backlight technique using FPZP after 10ns laser irradiation. (c) Profile of rear surface of measured shadow.

B.2 Quasi monochromatic imaging of diffusively heated region

We measured the two-dimensional heating distribution of the fast heated high energy density plasma. A heavy water target containing titanium as a tracer is used for measuring the two-dimensional heating distribution. The 250 μm diameter, 10 μm thickness plastic shell is filled with D_2O liquid contained 2.3% Ti atoms in weight through filltube. A open-tip gold cone is attached to this heavy water target. The heavy water target was compressed by GEKKO beams and heated by LFEX beams.

The Ti$-K_\alpha$ and the Ti$-He_\alpha$ emitted from the core were respectively imaged by FPZP to identify the heating region, as shown in Fig. B.5. When the REB passing through the cold plasma, Ti$-K_\alpha$ is emitted. The Ti$-K_\alpha$ emission is observed edge of the target and inside of filltube, as shown in Fig. B.5 (a). Titanium is rapidly ionized after heated up, and can emit He-like X-ray such as Ti$-He_\alpha$.The Ti$-He_\alpha$ emission where is the heating region was strongly observed along the laser axis, as shown in Fig. B.5 (b). The difference of emission region shows that the core is locally heated along the laser axis.

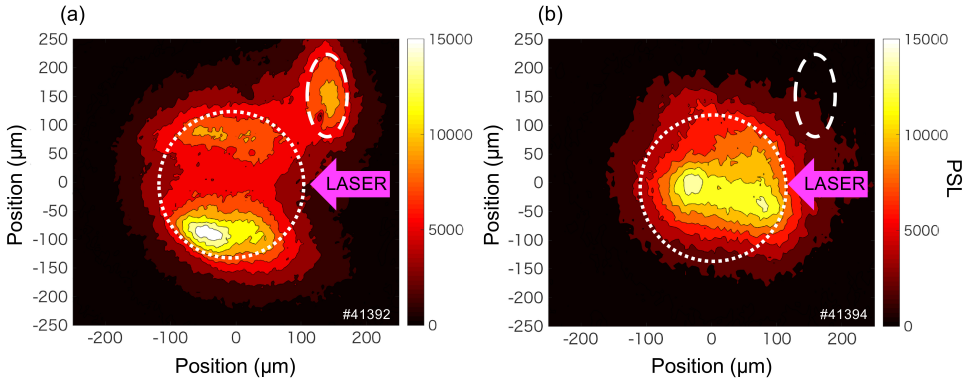

Figure B.5: (a)The Ti$-K_\alpha$ emission and (b)Ti$-He_\alpha$ emission from the core. A dotted line show the initial diameter of the target and a dashed line shows the position of the filltube. The Ti$-K_\alpha$ emission is observed edge of the target and inside of filltube. The Ti$-He_\alpha$ emission where is the heating region was strongly observed along the laser axis.